UNIVERSITY OF CALIFORNIA,

IRVINE

A Measurement of the Two Track Charged Current Quasi-Elastic Cross Section with the MINERνA Detector

DISSERTATION

submitted in partial satisfaction of the requirements

for the degree of

DOCTORAL OF SCIENCE

in Physics

by

Benjamin P. Ziemer

Disseration Committee:

Dr. Henry Sobel, Chair

Dr. Jonas Schultz

Dr. Steven Barwick

2012

Contents

List of Figures

List of Tables

ACKNOWLEDGMENTS

I owe gratitude to my family for their unwaivering support in many difficult times that were faced during my time at UCI. I certainly would not have reached the end of my PhD without this support.

Nemo vir est qui mundum non reddat meliorem

This research was funded by a grant for the Department of Energy.

CURRICULUM VITAE

Benjamin P. Ziemer

2003	B.S. in Chemistry, University of Wisconsin, Madison
2003	B.S. in Mathematics, University of Wisconsin, Madison
2003	B.S. in Physics, University of Wisconsin, Madison
2006	M.S. in Physics, University of California, Irvine
2006-12	Research Assistant Particle Physics, University of California, Irvine
2012	PhD. in Physics, University of California, Irvine

FIELD OF STUDY

High Energy Neutrino Particle Physics

PUBLICATIONS

D. D. Stancil et. al. Demonstration of Communication Using Neutrinos Modern Physics Letters A 27 (2012)

N. Tagg et. al. Arachne - A Web-based event viewer for MINERνA Nuclear Instruments and Methods in Physics 676 (2012) 44-49

G. N. Perdue et. al. The data acquisition system and infrastructure Nuclear Instruments and Methods in Physics Research Section A: Accelerators, Spectrometers, Detectors and Associated Equipment 694 (2012) 179-192

ABSTRACT OF THE DISSERTATION

A Measurement of the Two Track Charged Current Quasi-Elastic Cross Section with the MINERνA Detector

by

Benjamin P. Ziemer

Doctoral in Physics

University of California, Irvine 2012

Professor Hank Sobel, Chair

The MINERνA detector collected 1.2×10^{20} POT of ν_μ data with the NuMI beam at Fermi National Laboratory from 03/2010 to 07/2010. I will describe an analysis to identify two track charged current muon neutrino quasi-elastic interactions using this data set. The final state muon was identified by curvature using the MINOS detector. The final state contained proton was identified by the energy deposited per unit length at the end of the track. Two additional cuts were applied to separate signal from background: a cut on the extra energy in the event and a cut on a proton energy dependent variable. The $d\sigma/dQ^2$ using this selection is presented. An initial list of systematic errors is introduced and calculated. In addition to this analysis work, I also developed both pattern recognition schemes used by the experiment, wrote MINOS muon track matching algorithms, implemented a Kalman Filter track fitting algorithm and contributed to various other tasks to the MINERνA experiment; I will provide an explanation of these. I will also give a brief overview of neutrino physics, the NuMI beam, and the MINERνA detector.

1 Introduction

The MINERνA experiment is located at Fermi National Accelerator Laboratory and uses the 'Intensity Frontier' NuMI neutrino beam. The experiment will measure neutrino and anti-neutrino cross sections to a high precision. The tracking region of the detector is constructed with hexagonal planes of scintillator approximately 2.1cm thick. These planes have lead absorbers attached in the electromagetic calorimeter portion of the detector and steel absorbers in the hadronic calorimeter region. In addition, the detector has helium, water, lead, iron and carbon targets installed in upstream of the tracking region. These will be used to study and extract neutrino nuclear effects. This will be an unprecedented study as these five nuclear targets can be studied in the ***same*** beam; many previous studies relied on taking unfolded data distributions from different experiments, detectors and beams and then extracting nuclear effects. Numerous other topics will also be studied: the presence/absence of coherent π events, the strangeness contribution to the nucleon, confirmation/rejection of new N particle/N hole theories and meson exchange currents, in addition to many other topics.

A two-track neutrino charged current quasi-elastic analysis will be presented. This analysis includes two-track vertices with a muon track that is identified by the MINOS detector and an inner detector contained track identified as a proton by the energy deposited per length. Other cuts are also applied to the data/monte carlo in order to enhance the signal over background. A final cross section is reported for the two-track quasi-elastic process. An initial list of systematic errors is provided and calculated for this process. Additional systematic errors and the progress towards their evaluation are presented.

A description of the MINERνA detector and the NuMI beam will be provided. Brief overviews of the relevant neutrino physics and the GENIE event generator are also

presented. There is a review of the event reconstruction in MINERνA. The author of this document played a large role in this development of the event reconstruction and the particular contributions are highlighted.

2 Few GeV Neutrino Physics

As modern day HEP experiments probe new and more precise physics topics, the costs have risen. Fiscal limitations dictate that these experiments obtain maximal physics reach on a variety of issues. The MINERνA project aims to provide a wealth of information to both aid current oscillation physics and provide error containment for future oscillation searches. It also can provide insight on stand-alone neutrino physics topics for which the bulk of current day knowledge comes from bubble chamber experiments and extrapolations that may or may not contain miscalculations (*e.g.* neutrino nuclear effects). The MINERνA collaboration contains participants from, and will work with, the MINOS collaboration, Jefferson National Laboratory and the theoretical HEP and nuclear community to extract the most from the modest (in size and cost) MINERνA project.

Pion absorption by the nucleus can bias reconstructed neutrino energy to lower values than the actual value. Current resonance-mediated pion production cross sections are beset by errors and the data itself are sparse. MINERνA's finely segmented scintillating inner tracking region will take measurements of these exclusive final state processes to give precision cross-section measurements that will further aid oscillation searches. There have been recent experiments that have found a 30% higher charged current quasi-elastic (CCQE) M_A. This could be due to nuclear effects, mis-identified pion production events (where the pion was absorbed), new meson exchange currents or some other still unknown process. MINERνA will shed light on this situation.

2.1 Neutrino Interactions

The neutrino has a non-composite nature and flavor-discrimination that make it an ideal probe in scattering experiments. The relatively low cross-section hindered detec-

tion rates at previous detectors. With the intensity reach by the NuMI beam, rates are sufficient now to study neutrino interactions with unprecedented accuracy. Anti-neutrino running, accessible by NuMI, would allow for further physics reach with the MINERνA detector.

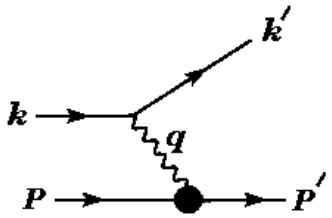

Figure 1: Incoming neutrino, k, radiates a $W^{\pm}$ or Z, transforming it to the corresponding lepton (while changing the target in the case of $W^{\pm}$ emission). The outgoing particle, P', could be a proton, neutron, pion, etc., depending on the channel of interaction.

The primary interaction has the neutrino, k, changing to a lepton, k', after it interacts with the target, P (see figure 1). The neutrino and the target can interact via a $W^{\pm}$ or Z^0 exchange. The target of interest depends on the incoming neutrino energy. At lower energy, the target is the neutron and the channel is simple (quasi-) elastic scattering. The next dominant interaction is resonant pion production. These channels include:

$$\nu_\mu p \to \mu^- p \pi^+, \quad \nu_\mu n \to \mu^- n \pi^+, \quad \nu_\mu n \to \mu^- p \pi^0$$

The dominant production proceeds through the $\Delta(1232)$ resonance, but other resonances are known to contribute as well. Multi-π production does enter in, but single-π is a channel that can obfuscate neutrino oscillation analysis and needs to be studied more in depth. As the energy increases further, the neutrino probes the quark, rather

than hadron, nature of the target and the final state, P', becomes a shower of hadrons and one considers inclusive rather than the above exclusive processes. MINERνA measurements in this energy region will probe the nucleon quark composition. The MINERνA experiment will be able to give a detailed study of the $V-A$ structure of the weak current. Field Theory lets us write this hadronic current in terms on four-momenta (P,P' and $q = P' - P$) of the participating particles:

$$< p(P`)|J_\lambda|p(P) >= \mathbf{M_\lambda^V} - \mathbf{M_\lambda^A}$$

$$\mathbf{M_\lambda^V} = \begin{pmatrix} \cos\theta_c \\ \sin\theta_c \end{pmatrix} \overline{u}(P`) \left[\gamma_\lambda f_1(Q^2) + \frac{i\sigma_{\lambda\nu}q^\nu f_2(Q^2)}{2M} + q_\lambda f_3\right] u(P)$$

$$\mathbf{M_\lambda^A} = \begin{pmatrix} \cos\theta_c \\ \sin\theta_c \end{pmatrix} \overline{u}(P`) \left[\gamma_\lambda\gamma_5 g_1(Q^2) + \frac{i\sigma_{\lambda\nu}\gamma_5 q_\lambda g_2(Q^2)}{2M} + \gamma_5 q_\lambda g_3\right] u(P)$$

Vector form factors are f_1, f_2 and f_3 (dubbed vector, weak magnetism, and induced scalar, respectively). Axial form factors are g_1, g_2 and g_3 (dubbed axial vector, pseudo-tensor and induced pseudo-scalar, respectively). The conservation of the electromagnetic current leads one to believe that this weak current is also conserved. Using the Conserved Vector Current hypothesis or CVC, relations between the weak and corresponding well-known electromagnetic form factorscan be found.

$$f_1(Q^2) = F_1^p(Q^2) - F_1^n(Q^2) \qquad f_2(Q^2) = F_2^p(Q^2) - F_2^n(Q^2)$$

where,

$$F_1^{p,n} = \frac{G_E^{p,n} + \frac{Q^2}{4M^2}G_M^{p,n}}{1 + \frac{Q^2}{4M^2}}, \qquad F_2^{p,n} = \frac{G_M^{p,n} - G_E^{p,n}}{1 + \frac{Q^2}{4M^2}}$$

and CVC tells us,

$$f_1(Q^2) \overset{Q^2\to 0}{\longrightarrow} 1, \qquad f_2(Q^2) \overset{Q^2\to 0}{\longrightarrow} \mu_p - \mu_n \qquad f_3(Q^2) = 0$$

with μ_α representing the particular particle's magnetic moment. Looking at the transformation properties in the current, f_1 and f_2 share the same transformation sign while f_3 has the opposite sign; similarly, g_1 and g_3 transform differently than g_2. Looking again at the $Q^2 \to 0$ limit, $\mathbf{M_\lambda^V} - \mathbf{M_\lambda^A}$ becomes pure vector and axial vector, $\overline{u}(P`)\gamma_\lambda(1 - g_a\gamma_5)u(P)$. Based on their transformation properties, this leads one to classify f_1, f_2, g_1 and g_3 as first-class currents and f_3 and g_2 as second-class currents. Experiments suggest the absence of these second class currents (the conserved vector current hypothesis dictates that $f_3 = 0$) or that the effects from them are very small. However, nuclear effects might change the contribution of these to non-negligible values. The above-described form factors describe the cross-section for the quasi-elastic and resonance channels (with various multiplicative factors). The form factors can be thought of as an effective interaction radius of the particle by taking the Fourier transform. This interpretation works well with the nucleon picture, but as energy increases, the neutrinos probe the quark nature of the nucleus and the picture breaks down. Neutrinos have quark specific interactions and therefore are a clean probe of quark compositions. Comparing formulas for nucleon- and quark-model cross-sections, one can obtain quark content of the form factors.

$$\begin{aligned}
\nu N: \quad & f_2 = x[u + d + \overline{u} + \overline{d} + 2s + 2\overline{c}] \qquad xf_3 = x[u_v + d_v + 2s - 2\overline{c}] \\
\overline{\nu} N: \quad & f_2 = x[u + d + \overline{u} + \overline{d} + 2c + 2\overline{s}] \qquad xf_3 = x[u_v + d_v - 2c - 2\overline{s}]
\end{aligned}$$

Here, $x_{bj} = \frac{Q^2}{2M\nu}$ is the fraction of momentum carried by the quark, and $q_v = q - \overline{q}$ is

the valence quark content. The previous assumption of $f_3 = 0$ is valid because at lower energies charm and strange production is suppressed.

Neutral current interactions are suppressed by a factor of roughly one-third to the charged current interactions. In general, they are harder to detect at lower energies and only become visible in a scintillating detector when the neutron has enough energy to re-interact in the detector. This is also the case for low energy proton stubs. These neutral current signals can be confused with various backgrounds in the detector. The neutral current Lagrangian, for neutrinos, has factors of $\sin^2\theta_W$ absent in the charged current version. By taking the ratios of these two, one can extract this parameter. The NuTeV experiment [1] found a value of $\sin^2\theta_W$ that was approximately 3σ away from the accepted Standard Model value. Extensive error analysis was unable to remedy this disagreement. MINERνA will be able to confirm or deny this and possibly determine the nature of the discrepancy (*e.g.* neutrino-induced nuclear effects, etc.).

Other physics areas of interest accessible with the MINERνA detector are exclusive strange production channels, charm production, kaon physics, neutrino-induced nuclear effects, and generalized parton distributions.

2.2 Quasi-elastic Scattering

The simplest reaction that a neutrino can undergo is the quasi-elastic channel. The muon neutrinos from the NuMI beam will interact, via a charged current, only with neutrons in the carbon, lead, scintillator, etc. In this reaction, the incoming neutrino approaches the nucleon, radiates a W^+ and changes into the neutrino's corresponding lepton, simultaneously changing a down (neutron) quark into an up quark (proton). With anti-neutrinos, the targets are the protons and neutrons are emitted from the interaction vertex. This reaction channel is the main component of the cross-section at

neutrino energies below 2 GeV. MINERνA will be able to extract the Q^2 dependence of the weak current. This current is described by vector, axial-vector and pseudo-scalar form factors only; in the differential cross-section, $g_3(Q^2)$ is multiplied by $(m_l/M)^2$, consequently its contribution to muon neutrino interactions is very small except below energies of 0.2 GeV.

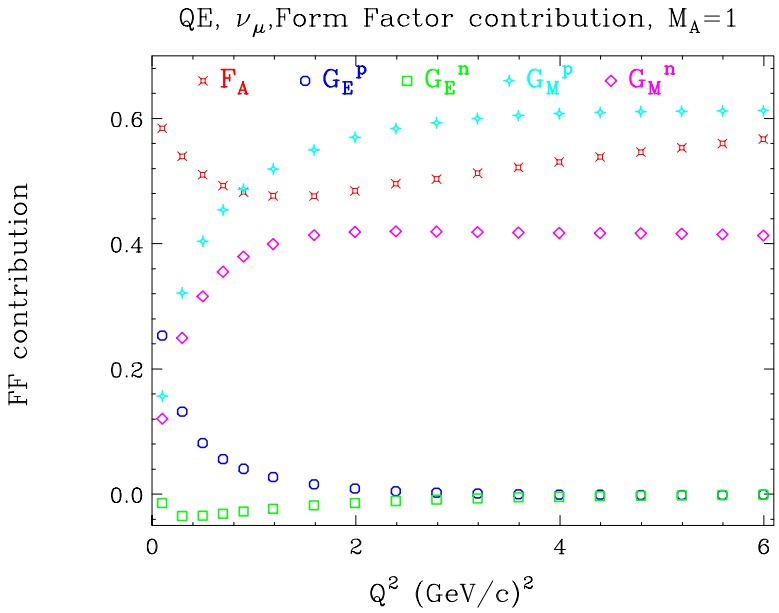

Figure 2: Fractional contributions of G_M^p,G_M^n,G_E^p, G_E^n and F_A to the Q^2 distributions for quasi-elastic neutrino samples with the NuMI beam. Because of interference terms, the sum of the fractions does not necessarily add up to 100%.

The form of the axial and pseudo-scalar form factors are generally taken to be that of a dipole [2, 3], although modifications to the dipole are presented in various theories. The dipole form of the factors is given here:

$$g_1(Q^2) = \frac{g_A}{(1+\frac{Q^2}{M_A^2})^2}$$

$$g_3 = \frac{2M^2}{m_\pi^2 - Q^2} g_1(Q^2)$$

The factor $g_A(= -1.2695 \pm 0.0029)$ is determined from the value of the form factor at $Q^2 = 0$ and M_A is an experimentally extracted parameter. Table 1 lists the various M_A values that have been extracted by other recent experiments.

Experiment	Target	Q^2 Cut	M_A (GeV)
K2K	oxygen	$Q^2 \geq 0.2$	1.2±0.12
K2K	oxygen	$Q^2 \geq 0.2$	1.14±0.11
MINOS	iron	no cut	1.19±0.17
MINOS	iron	$Q^2 \geq 0.2$	1.26±0.17
MiniBooNE	carbon	no cut	1.35±0.17
MiniBooNE	carbon	$Q^2 \geq 0.25$	1.27±0.14
NOMAD	carbon	no cut	1.07±0.07

Table 1: This table lists various extracted values of the parameter M_A obtained from other neutrino experiments. A range of targets, cut and M_A values exist.

The NOMAD experiment has a more extensive listing of various M_A values from experiments from prior to 2000 and from a larger variety of nuclear targets. This M_A survey has a spread of values from 0.7-1.3 GeV. The averaging of the world values yields M_A = 1.026±0.021GeV; the world average of the axial mass parameter from ν_μ-deuterium and pion electroproduction is M_A = 1.014±0.014GeV[4]. The current dipole form of the axial form factor agrees well with (averaged) world data, but is known to fail at higher energy transfers (Q^2) to the nucleus. There are two different methods for extracting the value of the axial mass: from the total CCQE cross section (the axial form factor makes up about 55% of the total CCQE cross section, see figure 2) and from an area normalized fit of the Q^2 spectrum from the specific event selection; care has to be taken with the latter method.

The MINERνA collaboration will test for deviations from the dipole form. In general, the axial form-factor $g_1(Q^2)$ can only be extracted from quasi-elastic neutrino scattering; at low Q^2, however, its behavior can also be inferred from pion electro-production data [2]. In addition, most extractions were done on lighter targets and using free form factors. Using bound form factors and the extrapolation to heavy targets could lead to significant changes to the form factors. Nuclear effects have been studied quite a bit with charged lepton experiments, but they have not been examined as extensively with neutrinos due to the lack of data, see section 2.4. There are also errors because results from different experiments cannot be compared directly. This is due to the existence of different targets, beam spectra, detector effects and efficiencies (and it is difficult to completely remove the dependency on these). The axial form factor (the axial mass, M_A) is input into oscillation analysis and high statistics MINERνA running will reduce this parameter's current errors. Since the axial form factor is a bulk contributor (see figure 2) to the cross-section in the energy ranges of today's oscillation experiments, fractional changes of M_A could lead to very different results.

Preliminary analysis of the quasi-elastic channel with a partial MINERνA data set is underway. There are one-track neutrino/anti-neutrino and two-track neutrino quasi-elastic analyses. The analyses are not quite advanced enough to release any fit for the axial mass parameter. The quasi-elastic channel is unique in the muon's dominant role in the kinematics. Using only muon information:

$$E_\nu = \frac{(m_n + E_b)E_\mu - \frac{1}{2}(2m_nE_b + E_b^2 + m_\mu^2)}{m_n + E_b + p_\mu \cos\theta_\mu}$$

$$Q^2 = 2E_\nu(E_\mu - p_\mu \cos\theta_\mu) - m_\mu^2$$

In the formula, E_b represents a binding energy factor (set at 30MeV), but the formula neglects all Fermi motion. MINERνA's fine segmentation ensures good θ_μ resolution and p_μ will be known to 5-10% depending on if the muon stops in MINERνA or enters the MINOS magnetic field region. The pattern recognition enables the tracking of short protons which can further add information in the quasi-elastic channel. Using only proton information:

$$Q^2 = 2m_p T_p$$

Here T_p refers to the kinetic energy of the proton. This formula allows the Q^2 to be matched using the muon and proton information separately. This last formula can also help to assist in identifying background and/or mis-reconstructed events when the extracted Q^2 is below the detection threshold for the detector (this is mentioned later in section 7).

2.3 Pion Production

As mentioned in the introduction, current data on π-production is sparse. The post-MINERνA situation will greatly increase knowledge of this neutrino interaction channel. There are different channels for π-production that MINERνA will address: coherent and resonant production of both charged and neutral π's; exclusive single- and multi-π reactions and inclusive production channels. The latter will be used to measure structure functions through the resonance to the deep inelastic regime.

Coherent production involves low energy transfer (t-channel) to the nucleus resulting in emergence of a muon and charged pion for charged current interactions, $\nu_\mu A \to \mu^- \pi^+ A$,

or a neutrino and neutral pion in neutral current interactions, $\nu_\mu A \rightarrow \nu_\mu \pi^0 A$. Many models rely on the Rein-Seghal model that uses the partially conserved axial-vector (PCAC) hypothesis. The PCAC hypothesis works well for higher energy neutrino interactions, but fails to explain data at lower energies. Some experiments have reported the complete absence of this channel in their data set and find a suppression of 0.60×10^2 compared to the charged current interaction [5] (the absence could be due to the unexplored neutrino nuclear effects). MINERνA's good reconstruction and calorimetric capabilities along with various nuclear targets make it possible to extract the A-dependence of this process, in addition to confirming or denying findings of previous experiments. Neutral current π theory agrees to a better degree than its charged current partner. This channel's signature is the presence of π^0 in the final state which appears as two electromagnetic showers from the subsequent decay photons. The kinematics of the neutral current coherent production allow it to be distinguished from other π^0 production channels. Resonant produced π's are typically lower in energy and do not necessarily follow the incident neutrino direction as the coherent-π's. As mentioned earlier, this channel can mimic the signal of neutrino oscillations in water Cherenkhov detectors when the two decay photons are not sufficiently separated and then are reconstructed as a single electron ring-like event. Reconstruction of neutral-π production in MINERνA has a high purity with only a $\sim 1\%$ contamination from charged current interactions [6] after cuts are made on the reconstructed energy of the two photon showers.

The lack of data in resonant mediated production of $\pi^{\pm,0}$ makes taking measurements of these channels worthwhile on their own. Previous data on this channel comes from bubble chambers, *i.e.* light nuclei targets. As mentioned previously, the neutrino cross-section necessitates heavy-A targets to achieve desirable rates. This introduces unknown corrections for the different nuclear environments that need to be studied. It has been shown in reference [7] that the cross-section can be described by only two of

the form factors, F_3^V and F_5^A. Using the common dipole form factor, the resonance production cross-section ($d\sigma/dQ^2$) shows disagreement with data at lower Q^2. Current dipole-based form factors are inflated at this lower energy transfer, but do agree at higher values. This has motivated the introduction of a modified form,

$$F^V_{old}(Q^2) = \frac{F_i(0)}{(1+\frac{Q^2}{M_V^2})^2}, \qquad F^V_{new}(Q^2) = \frac{F_i(0)}{(1+\frac{Q^2}{M_V^2})^2}\frac{1}{1+\frac{Q^2}{4M_V^2}}$$

$$F^A_{old}(Q^2) = \frac{F_i(0)}{(1+\frac{Q^2}{M_A^2})^2}, \qquad F^A_{new}(Q^2) = \frac{F_i(0)}{(1+\frac{Q^2}{M_A^2})^2}\frac{1}{1+\frac{Q^2}{3M_A^2}}$$

with

$$F^V(0) = 1.95, \qquad M_V = 0.84GeV$$

$$F^A(0) = 1.2, \qquad M_A = 1.05GeV$$

These parameters are a fit to the data in the region above $0.2GeV$. Including this region, in which nuclear effects become non-negligible, worsens the fit. The problem is not remedied with the inclusion of simple Pauli suppression. The modified dipole form fits the data better than the older Schreiner and von Hippel [8] at all values of Q^2, but still are inflated near $Q^2 = 0$. The authors of reference [7] also investigate the ratio of single-π production to quasi-elastic events to minimize the common unknown nuclear effects at low Q^2. Analysis discussed here focused on the Δ resonance ($W \leq 1.4GeV$); MINERνA analysis of the resonance channel will be primarily with this cut as well. Fermi motion serves to smear out higher W resonances. MINERνA will work with corresponding JLab experiments and collaborators in the extraction of the resonance

vector form factor. As with the quasi-elastic case, the axial factor is only able to be determined from $V-A$ weak structure of neutrino interactions. A preliminary analysis of this region with the MINERνA simulation clearly shows the Δ resonance in the reconstructed invariant mass (W) for the reaction. There are several pion analyses that are on-going in MINERνA experiment; these analyses include pions created from both neutrino and anti-neutrino resonant and coherent channels.

2.4 Nuclear Effects

Nuclear effects have been shown with electron and muon beam interactions with varying targets. The introduction of more nucleons (higher-A material) modifies the cross section in a variety of ways depending on the kinematic variables, of the particular reaction, in this case x_{bj}. The quantity that is studied is the ratio of σ^A/σ^D (or the ratio of varying form factors that make up the cross section, σ). Here, A refers to a heavy nucleus and D refers to deuteron. Deuteron is the simplest picture of an isoscalar nucleus; the concept is that $F_i^D = \frac{F_i^p+F_i^n}{2}$. At lower values of x_{bj}, $x_{bj} < 0.1$, the ratio σ^A/σ^D falls below one. The ratio rises above one, at a few percent, in the $0.1 < x_{bj} < 0.3$ region. At values of $0.3 < x_{bj} < 0.8$, the ratio drops substantially depending on the specific A of the material with the minimum at $x_{bj} \sim 0.6$. Above $x_{bj} = 0.8$, the ratio rises again and continues beyond $x_{bj} = 1$; based on the definition of x_{bj}, it should never rise above unity, but Fermi motion allows this to occur. These regions in x_{bj} space are named the shadowing, anti-shadowing, EMC effect, and Fermi motion regions, respectively. Throughout this kinematic range, the scattered particles can undergo final state interactions (FSI) which obscure the original interaction. The interactions that are seen in MINERνA are the combination of both of these effects. Each of the regions has some theoretical models and descriptions, but most come from the extensive data available from ***charged*** lepton scattering. Neutrino nuclear effects data is very sparse and any models of neutral lepton nuclear effects therefore suffer.

This review will focus on the former rather the latter and more extensive reviews of the subject can be found in references [9, 10].

Models of shadowing follow the vector meson dominance model (VMD). During an interaction (small x_{bj}), the longitudinal momentum transfer to the target and the lifetime of the particle of mass m is:

$$p_L = (m^2 + Q^2)/2\nu \qquad t = p_L^{-1} = 2\nu/(m^2 + Q^2)$$

For this kinematic region, the lifetime (or distance traveled) of this intermediate state is longer than inter-nucleon distance or greater than the nucleus itself. The state then interacts coherently with a number of the nucleons in the material resulting in a lower interaction rate per nucleon. In essence, the photon (here coming from the electron; but for neutrino interactions, this comes from the $W^{\pm}$), fluctuates into a hadronic particle, interacts with the nucleons, and effectively shadows the other constituents of the nucleus; this reduces the flux of incoming particles leading to a lower σ (or F_i). In the charged-lepton case, the fluctuations can be ρ, ω, and ϕ mesons. But for neutrinos, the introduction of the axial current introduces other states that this intermediate particle can change into before undergoing a reaction (a_1, etc.). The straight application from charged-lepton scattering is not as straight forward because the vector current disappears as $Q^2 \to 0$, while the axial current does not and is, in factor, the dominant contribution at low Q^2. This can describe the shadowing nuclear effect region but other models are proposed to explain shadowing and anti-shadowing simultaneously. This model is based in the Breit frame and uses the uncertainty principle. A quark that carries momentum xP_N of the nucleus can be confined to a region $\sim (xP_N)^{-1}$ in

the longitudinal direction. A nucleon in this frame has a spatial extent of $2R_N(M/P_N)$. We can then set two scales of this model:

$$x_N = 1/(R_N M), \qquad x_A = 1/(R_A M) \sim x_N A^{\frac{1}{3}}$$

Here, R_N and R_A refer to the nucleon and nuclear radius, respectively. Then, for $x_{bj} < x_N$ quarks from different nucleons can overlap and fuse; and, if $x_{bj} < x_A$ quarks throughout the nucleus have a chance to combine. On fusing, the number of partons at low-x_{bj} is reduced in favor of high-x_{bj} partons. It should be stressed that the momentum distribution of the partons is not altered by this, but simply re-arranged. As the cross-sections (distribution functions) are a measure of quark content (at a certain x_{bj}), at x_N this distribution is slightly enhanced, leading to anti-shadowing, and then falls off when approaching (smaller x_{bj} values) x_A [9]. This model has also been extended to include the possibility of gluon fusion, but, as this section is solely trying to give a broad view of the theoretical situation, is beyond its scope.

The next area of nuclear effects is named the EMC effect after the European Muon Collaboration that observed the effect in 1983. This region of x_{bj} ($0.3 < x_{bj} < 0.8$) is dominated by the valence distributions of the quarks and it appears the valence distribution in bound nuclei is suppressed relative to that of free nuclei. A first approach to explaining the EMC effect is one from nuclear physics. This approach hypothesizes an excess of virtual pions, associated with the strong force, in the nucleus. The quarks that belong to the nucleus then have a fraction of their momentum lost to the quarks and anti-quarks of the pion field. The structure functions then would be a combination of the 'regular' structure function weighted by the nucleus-quark distribution and a

pion function similarly weighted with a pion-quark function. Only a few extra pions are required for this type of an effect to reproduce the EMC data. A second approach has quarks inside the nucleus clustering and moving together independently in groups. The number of the quarks in the 'bag' vary from three to twelve. These quarks would then be described by adding a term to the structure function. Proposed models have distributions of $x^{1/2}(1-x/(i/3))^{2(i-1)-1}$ with i representing the number of quarks in the bag, xe^{-ax} with a=8-10, and $x^{1/2}e^{-Bx^2}$. These terms can be shown to reproduce the EMC effect in the appropriate x_{bj} range. The last methodology follows a similar approach in QCD and surmises that $F_2^A(x_{bj},Q^2) = F_2^D(x_{bj},\xi Q^2)$. The Q^2 that is felt by heavy nuclei is greater than that of a nucleon ($i.e\,\xi > 1$). Then, following the QCD formalism, start at $Q^2 = \mu^2$ where the the nucleon is described by the valence quarks only. The quark moments, in addition to the distributions, are equal $M_n^A(\mu_A^2) = M_n^N(\mu_N^2)$. As in QCD, the moments evolve according to:

$$\frac{M_n^A(Q^2)}{M_n^A(\mu_A^2)} = \left[\frac{\alpha_s(Q^2)}{\alpha_s(\mu_A^2)}\right]^{d_n} \qquad \longrightarrow \qquad \frac{M_n^A(Q^2)}{M_n^N(Q^2)} = \left[\frac{\alpha_s(\mu_N^2)}{\alpha_s(\mu_A^2)}\right]^{d_n}$$

where d_n in the QCD dimension and the above equality is used on the right. This leads to the solution of the parameter ξ of:

$$\xi(Q^2) = (\mu_N^2/\mu_A^2)^{\alpha_s(\mu_A^2)/\alpha_s(Q^2)}$$

Various nuclei have ξ values of 1-2. The solution to the theory disagreement in this x-region comes from a Drell-Yan production experiment. D.M.Alde et.al, found that the data from the production of muons fits this scheme with a $\xi \sim 2$. Structure function,

F_2^D, data from experiments at SLAC and JLab can be fit to the scaling hypothesis. The last region of nuclear effects ($x_{bj} > 0.8$) is attributed to Fermi-motion, nuclear binding and off-mass-shell effects of the nucleons. This large-x_{bj} region is generally treated by ignoring FSI and convolving the deuteron structure function with distribution functions of the nucleons in the heavier nucleus.

$$F_2^A(x) = \int_x dy D_{N/A}(y, p^2) F_2^N(x/y)$$

The distribution function is then formulated more specifically depending on what region of phase space and what effects are being investigated [9, 10, 11, 12]. For the region in question:

$$D_{N/A}(y, p^2) = \int \frac{d^4p'}{(2\pi)^4} \zeta(p') \left(1 + \frac{p'_3}{M}\right) \delta\left(y - \frac{p'}{M}\right) \delta(p^2 - p'^2)$$

and,

$$\zeta(p) = 2\pi \Sigma_n \delta(p_0 - M - \epsilon_n + T_R) |\Psi_n(\mathbf{p})|^2, \qquad p_0 = M + \epsilon_n - T_R$$

The factors p_0 and T_R are the energy and recoil of the interacting system,$|\Psi_n|^2$ is the probability function of the event (the nucleus starts in the state A and is changed to A-1, etc.), and ϵ_n is the energy removed from the struck nucleon. Forming the invariant

mass of the system,

$$p^2 = p_0^2 - \mathbf{p}^2 \simeq M^2 + 2M(\epsilon_n - T_R - \frac{\mathbf{p}^2}{2M}) \neq M^2$$

we see that off-shell effects are incorporated in this system. The probability function falls off with increasing $|\mathbf{p}|$, and central value have $y \sim 1$ and $p^2 \sim M^2$. Expanding the convolved function around these values:

$$F_2^A(x) \approx F_2^N(x) - \frac{\epsilon}{M} x F_2'^N(x) + \frac{T}{3M} x^2 F_2''^N(x) + 2\frac{\epsilon - T}{M}\left(p^2 \frac{\partial F_2^N(x,p^2)}{\partial p^2}\right)_{p^2=M^2}$$

with,

$$\epsilon = A^{-1}\int \frac{d^4p}{(2\pi)^4}\zeta(p)(p_0 - M), \qquad T = A^{-1}\int \frac{d^4p}{(2\pi)^4}\zeta(p)\frac{\mathbf{p}^2}{2M}$$

being the mean value of the single particle energy and kinetic energy. The average energy of the single particle state is correlated to nuclear binding (*i.e.* separation energy of the nucleons from the target). The next correction term accounts for the Fermi motion of the nucleons and is a large (positive) contribution to the structure function at higher x_{bj}. The last term accounts for the off-shell nature of the system.

All these formulations are, generally, treated separately and each in the region of applicability model data quite well. Some authors take a bolder approach and fit all x_{bj} values simultaneously as in reference [11]. These approaches have varying degrees of success. It should be stressed again that the above theoretical picture is the situation for ***charged*** lepton scattering. The models are widely thought to cross over to ***neutral*** lepton scattering, but corrections will have to be made for the axial current. A four year run (with the proposed beam scenario) of MINERνA would yield over 1000K events on both the Fe and Pb and 600K on the C nuclear target region (this does not include carbon events in the tracking scintillator volume). Post-MINERνA running, a non-statistics limited study of neutrino nuclear effects can be carried out and $V-A$ nuclear effect models can be formulated and tested. A preliminary study of a lower statistics sample of the MINERνA neutrino data was undertaken for two of the targets in the nuclear target region. The final result is a ratio of two of the targets to minimize errors. Furthermore, in depth studies will be done on the full MINERνA data sets as well as on the full range of nuclear targets that are available. The preliminary results from this smaller sized study are shown in figure 3.

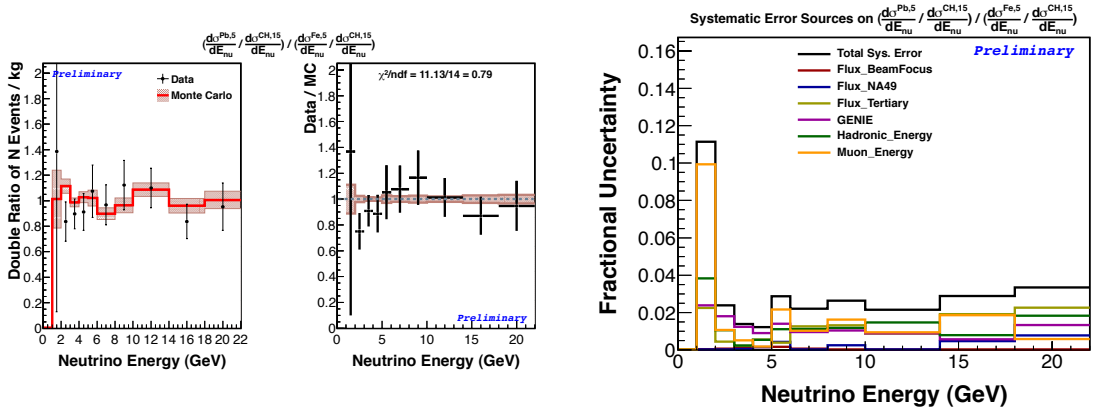

Figure 3: Left: Shown is the double ratio of target five events in lead over plastic background divided by events in iron over the plastic background as a function of neutrino energy. Right: Shown is the systematic error of the double ratio as a function of the neutrino energy.

The other difficulty that the high-A targets necessary for sufficient neutrino interactions

introduce are final state interactions (FSI). This is extremely important in the precision era of neutrino physics as the final state interactions can alter the neutrino-nucleon cross-section at the 10-30% level. The dominant concern is the interaction of pions produced directly or by the decay of various resonances. These pions have five channels through which they can re-interact: elastic scattering (nucleus left in ground state), inelastic scattering (nucleus left in excited state and/or parton(s) ejected), absorption, single-charge exchange, or double-charge exchange. Elastic, inelastic, and absorption interactions make up roughly 40, 20 and 35% (700, 360 and 600mb) of the total (pion) cross-section on iron and 35, 33, and 25% (220,210,160mb) for carbon. These high values make it likely that pions crossing MINERνA will likely undergo a few strong interactions before they range out or leave the detector. This translates to problems for experiments because the pion energy can be spread out over a number of nucleons or lost completely (in elastic or absorption reactions) after these final state interactions. This loss of hadron energy translates into a miscalculated incoming neutrino energy. Also, there is a more direct trouble with absorption-FSI, as the loss of a pion in the final state of a $\nu_l A \to l A' \pi$ mimics the quasi-elastic signal, $\nu_l n \to l p$, that is used as a signal in oscillation experiments. If these 'absorbed pion events' are used in a CCQE analysis, the reconstruction of the neutrino energy from the muon kinematics will be incorrect. Also, protons and neutrons can interact and produce more hadrons upon exiting the nucleus. This can lead to misclassification of higher multiplicity DIS events that can also produce incorrect results. With the above mentioned rates for Fe, Pb and C interactions, studies will be done to further understand the nature of FSI and, indirectly, reduce the backgrounds for neutrino oscillation analysis.

2.5 Strange Physics

Although not specifically designed to identify short recoil protons, MINERνA has the capability to measure the strange content of the nuclei, $G_A^s(0) = g_A^s$. This can be

achieved by making measurements of neutral current elastic scattering interaction. The axial form factor is generally parameterized by a dipole:

$$G_A(Q^2) = \frac{G_A(0)}{(1 + \frac{Q^2}{M_A^2})^2}$$

At Q^2=0, the value is given by:

$$G_A(0) = \begin{cases} \frac{-g_A\tau_3 + g_A^s}{2} & : \quad NC \\ g_A\tau_\pm & : \quad CC \end{cases}$$

where $g_A = 1.26$ determined by neutron decay. The operators τ_3 and $\tau_\pm$ are defined by:

$$\tau_3|p\rangle = +|p\rangle, \quad \tau_3|n\rangle = +|n\rangle$$

$$\tau_+|n\rangle = +|p\rangle, \quad \tau_+|p\rangle = 0$$

$$\tau_-|p\rangle = -|n\rangle, \quad \tau_-|n\rangle = 0$$

The strangeness contribution to the nucleon spin is related to the axial form factor by: $\Delta \mathrm{s} = G_A(Q^2 = 0) = g_A^s$. This can be extracted in the cross sections by taking the ratio:

$$R(Q^2) = \frac{(d\sigma/dQ^2)_\nu^{NC}}{(d\sigma/dQ^2)_\nu^{CC}}$$

or

$$R_\nu = \frac{\sigma(\nu_\mu p \to \nu_\mu p)}{\sigma(\nu_\mu n \to \mu^- p)}$$

This can also be done by incorporating anti-neutrino beam data and analyzing the

asymmetry $A(Q^2)$,

$$A(Q^2) = \frac{(d\sigma/dQ^2)_{\nu}^{NC} - (d\sigma/dQ^2)_{\overline{\nu}}^{NC}}{(d\sigma/dQ^2)_{\nu}^{CC} - (d\sigma/dQ^2)_{\overline{\nu}}^{CC}}$$

[13].

This analysis was done with the BNL734 data [14] and values from $-0.21 \leq g_A^s \leq 0$ were obtained with large error bars. The value of g_A^s was found to be heavily dependent on the value of M_A; any newer analysis of Δs or g_A^s will most likely yield differing results due to the higher values of M_A found by newer experiments. Negative values are favored from neutrino data and certain QCD models, but parity violating electron scattering data suggests positive values [15].

The timing capabilities of MINERνA allows the study of displaced vertices, a signature of strange particle production. Also with $\overline{\nu}$ beam time, a study of hyperon beta decay would yield new measurements of form factors and CKM matrix elements. With NuMI's high rate, strangeness changing neutral currents in the neutrino sector, if they exist, in rare K decays could indicate new physics.

2.6 Physics Conclusions

The MINERνA detector can give insight on numerous topics in high energy physics. A few of these topics are critical inputs for many future physics studies: precision cross sections, axial mass determination and weak current nuclear effects. In addition, the MINERνA detector has reach into other areas such as strangeness of the nucleon, $\sin^2\theta_W$ determination, and existence/absence of charged current coherent production. With sufficient $\overline{\nu}_\mu$ running, the window of physics insight would open even farther. The high intensity NuMI neutrino beam compels the extraction of the most physics while

it is in operation.

3 NuMI Beam

The NuMI beam is currently the most intense source of neutrinos that exists. The intensity of the source is coupled with versatility in that NuMI is able to produce neutrino beams with three different energy spectra. Many in the physics world are currently focused on the Large Hadron Collider and the recent experimental confirmation of the existence of a Higgs-like boson. This is an important advancement in the field; this should not eclipse the fact that the data MINERνA has recorded can reveal secrets in the neutrino sector.

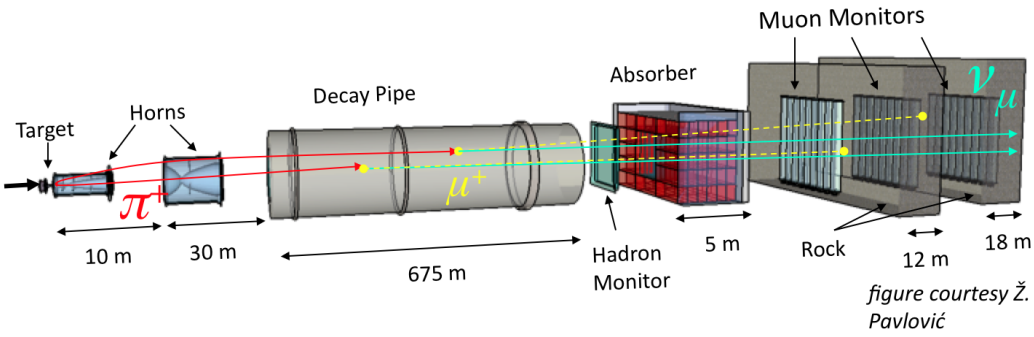

Figure 4: The variable energy NuMI $\nu/\overline{\nu}$ beam. The various components that comprise the beam are spread over a kilometer on the FNAL grounds. This is currently the most intense source of neutrinos that exists in the world.

A picture of the various stages of the NuMI beam is shown in figure 4. These stages will be described below.

3.1 Neutrino Generation

The first step in the generation of neutrinos is the extraction of the 120 GeV protons from the Fermilab Main Injection. Around 10^{12} protons in a 10μs time bunch are extracted every 2.2 seconds. The beam of protons, with an RMS width of 2.2mm, travel to a target hall where they strike a graphite target. The target is comprised of 6.4mm $\times$ 18mm $\times$ 20mm graphite sections. A total of 47 of these are placed end to end with

a 0.3mm spacing - the total length of the target is approximately 95cm corresponding to two proton interaction lengths. About 13% of the protons escape the target without interacting. The target structure also includes various support and cooling structures. The target also has been designed to minimize re-interactions of the protons in the target. A schematic of the target can be see in figure 5.

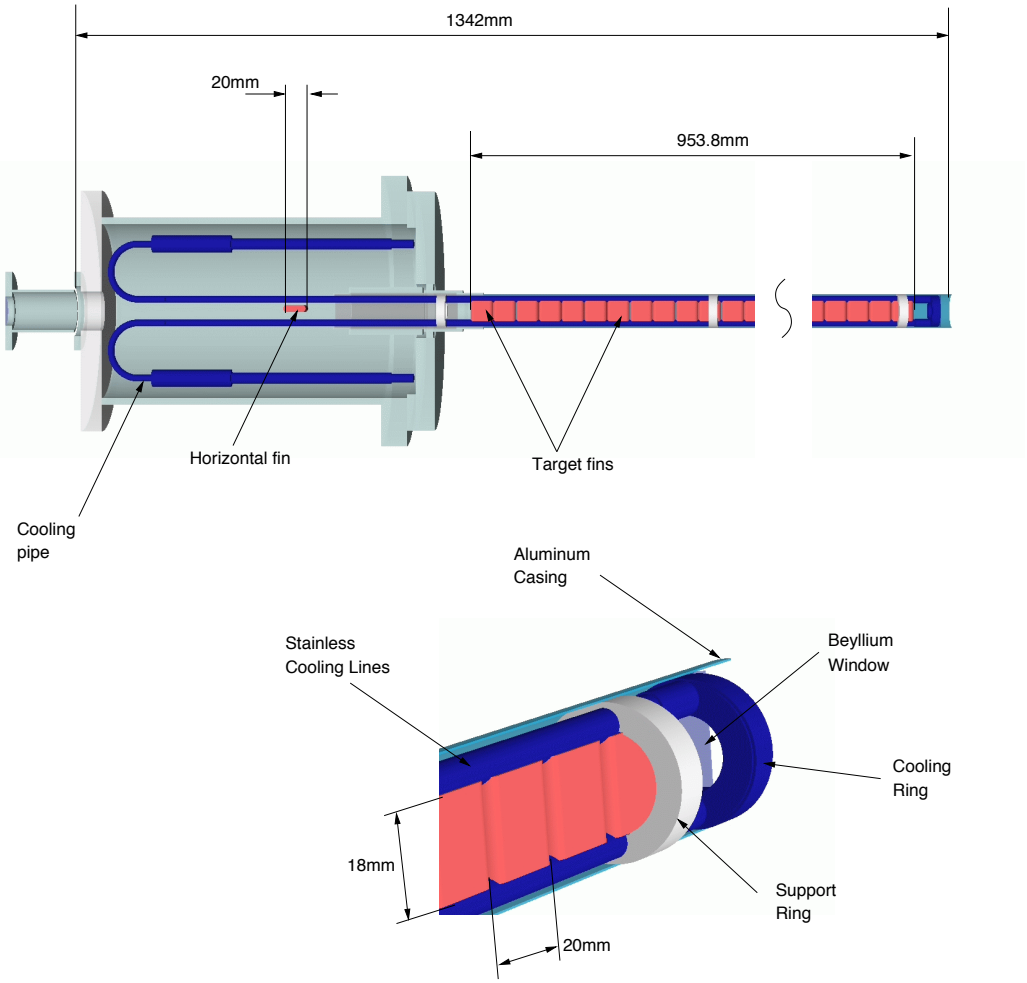

Figure 5: Shown in the target design for the NuMI target. The complicated design is both to ensure that a bulk of the protons from the main injector interact in the target, but also that the particles created from the interaction can escape the target without undergoing further interactions.

The protons interactions produce mainly charged pion and kaon secondaries. These charged particles leave the target at various angles and are not collimated. Two aluminum parabolic horns sit directly downstream of the target structure to refocus the

particles the stream of secondaries. The horns are about 10m apart from each other. A current is directed through these horns that creates a magnetic field. This magnetic field then in turn produces a force on the charged particles redirecting them back into a collimated beam, see figure 6. The focusing power is directly proportional to the particle momentum and inversely proportional to the current through the horn. With the horn focusing, the downstream flux of neutrinos seen at the detectors can increase by roughly a factor of 25 [16]. The polarity of the current in the horns can be switched to focus either positive or negative secondaries creating a neutrino or anti-neutrino beam (see below particle decays that produce the neutrino or anti-neutrino beam). Also, the specific current through the horns focuses only one particular momentum in the beam so that the focusing has varying effect on the spread of secondaries' momentum that are created by the interactions in the target.

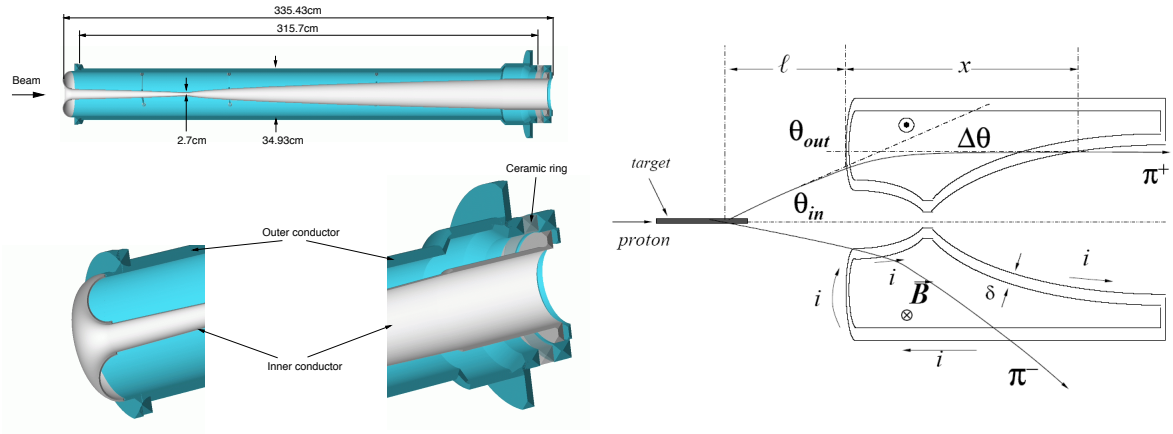

Figure 6: Left: Shown is the design of the first focusing horn the NuMI beam system. Right: The figure shows the details of the horn beam focusing.

Thirty meters downstream of the horns is the 675m long empty volume. This volume allows the focused particles to decay into the neutrinos that compose the NuMI beam. The relevant reactions are listed below and the contributions to the flux as a function of neutrino energy is shown in figure 7.

$\pi^{\pm} \rightarrow \mu + \nu_{\mu}$ $\tau \approx 26ns$ $branching\ ratio \approx 99.99\%$

$\mathrm{K}^{\pm} \rightarrow \mu + \nu_{\mu}$ $\tau \approx 12ns$ $branching\ ratio \approx 63.4\%$

$\mathrm{K}^{0}_{L} \rightarrow \mu + \nu_{\mu} + \pi$ $\tau \approx 52ns$ $branching\ ratio \approx 27.2\%$

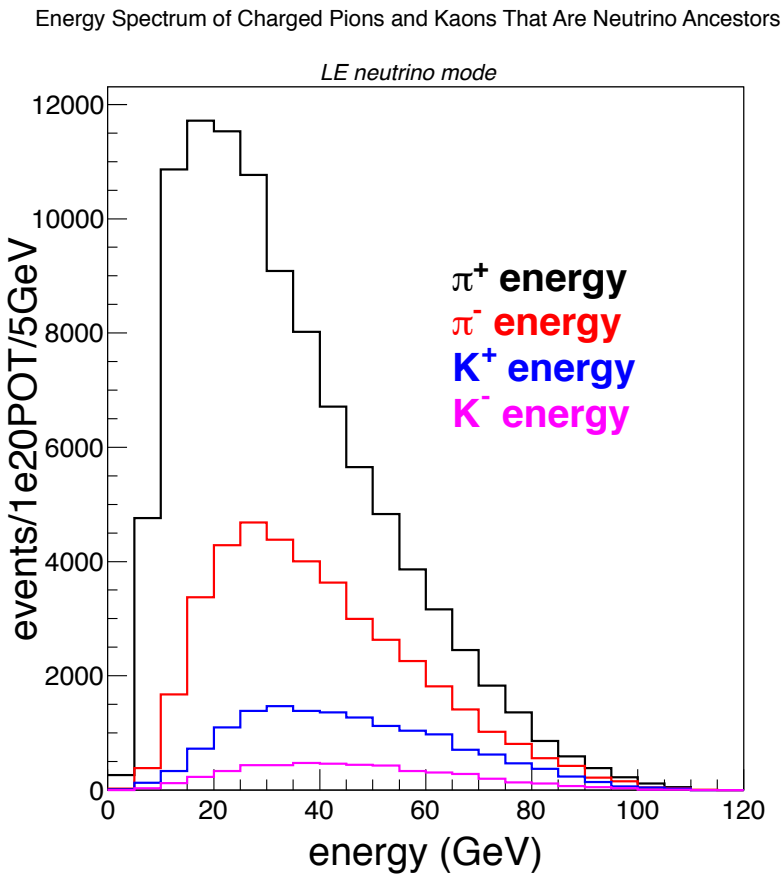

Figure 7: The various components of the LE flux as a function of the neutrino energy as predicted by gNuMI.

The particles created in the decay follow the direction of the parent particle. Some of the secondaries in the original proton interaction that are produced at high enough angles or that are outside of the focusing region will strike the walls of the decay pipe and interact. These interactions can also produce neutrinos that are directed downstream towards the detector hall. A hadron absorber sits directly downstream of the decay volume. The hadron absorber is made up of aluminum, steel and concrete. The aluminum and steel make hadrons further interact. The absorber also contains lower energy hadrons. The concrete serves to stop neutrons that are created in these reactions. A figure of the hadron and muon absorber/alcoves can be seen in 8.

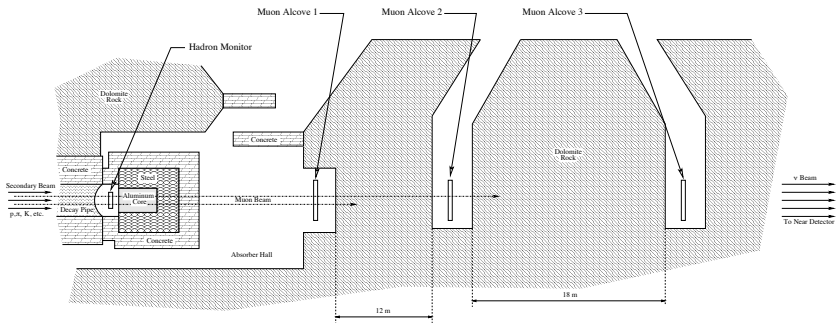

Figure 8: The secondary particle beam path is shown in the figure. First, the beam passes through the hadron absorbers. Then, it passes through earth where the muons are absorbed creating the ν beam.

At this point, the beam is comprised of μ's and ν's. Directly downstream of the hadron absorber is approximately 300m of earth. The highest energy muon that could be produced would be the same as the original proton energy (but, in reality the muon's energy is much lower than this). A 120 GeV muon would lose all of its energy via electromagnetic interactions in approximately 200m of earth. Therefore, muons that are produced in the secondaries' decay are completely absorbed after passing through this volume. This is the case with muons that pass along the beam line (i.e. go through all of the absorber); but, there are still muons that reach the experimental hall. These muons come from neutrino interactions that occur *before* reaching the MINERνA detector. These so-called rock muons are readily abundant and are used as a source of

calibration for the detector.

There are three stations set up along this last 300m distance of the beam line, with a fourth station being planned, that take measurements of the muons produced along with neutrinos. This muon monitor data can then be used as an alternate method of flux determination, see 3.2.1.

The final neutrino content of the beam, roughly a kilometer downstream from the initial location of the 120GeV proton extraction, is listed in table 2.

type	composition
ν_μ	92.9%
$\overline{\nu}_\mu$	5.8%
$\nu_e/\overline{\nu}_e$	1.3%

Table 2: The table lists the percent composition of the NuMI LE ν beam.

3.1.1 NuMI Energy Configurations

As already mentioned, the current through the horns varies the particular secondary particle momentum being focused. Altering this current changes the neutrino energy spectrum that gets delivered to the experimental hall. The spectrum for a few various currents is shown in figure 9.

In addition, the target apparatus and horns are able to move up and downstream relative to each other. This changes the spectrum of secondaries' momentum focused by the horns. This variability could theoretically allow neutrino beams with an infinite number of differing energy spectra. In the end, only three main different configurations are used: low energy (LE), medium energy (ME) and high energy (HE). The neutrino energy spectra are shown in figure 10 and for anti-neutrino mode in figure 11. The

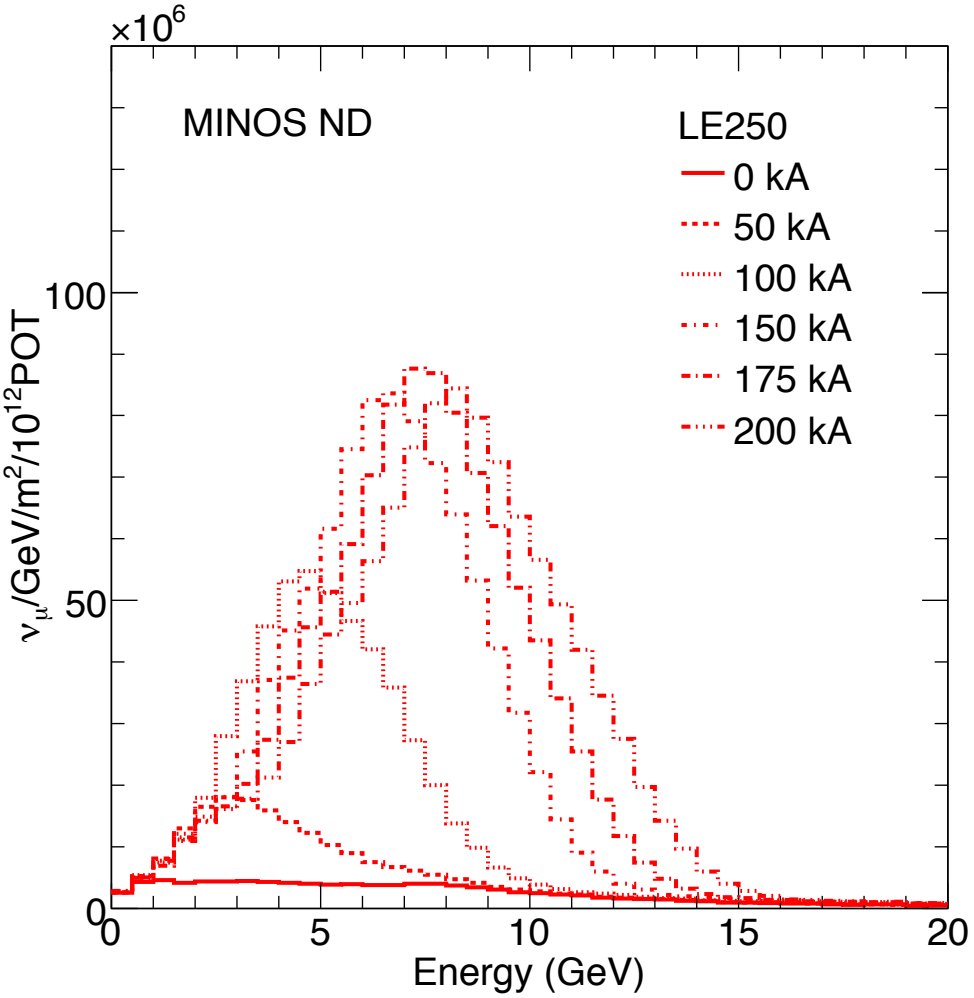

Figure 9: The ν_μ flux is shown as a function of energy or various currents through the focusing horn. As expected a higher current focuses higher energy particles that are ejected from the target at higher angles.

neutrino LE beam corresponds to a 185kA negative current, the focusing horns 10m apart and the target position of z=-10cm; the neutrino ME beam refers to a 200kA negative current, horns 23m apart and a z=-100cm position. The parameters for the anti-neutrino beam are the same except the horn current polarity is reversed. The HE mode of the beam is mainly only used in target scans.

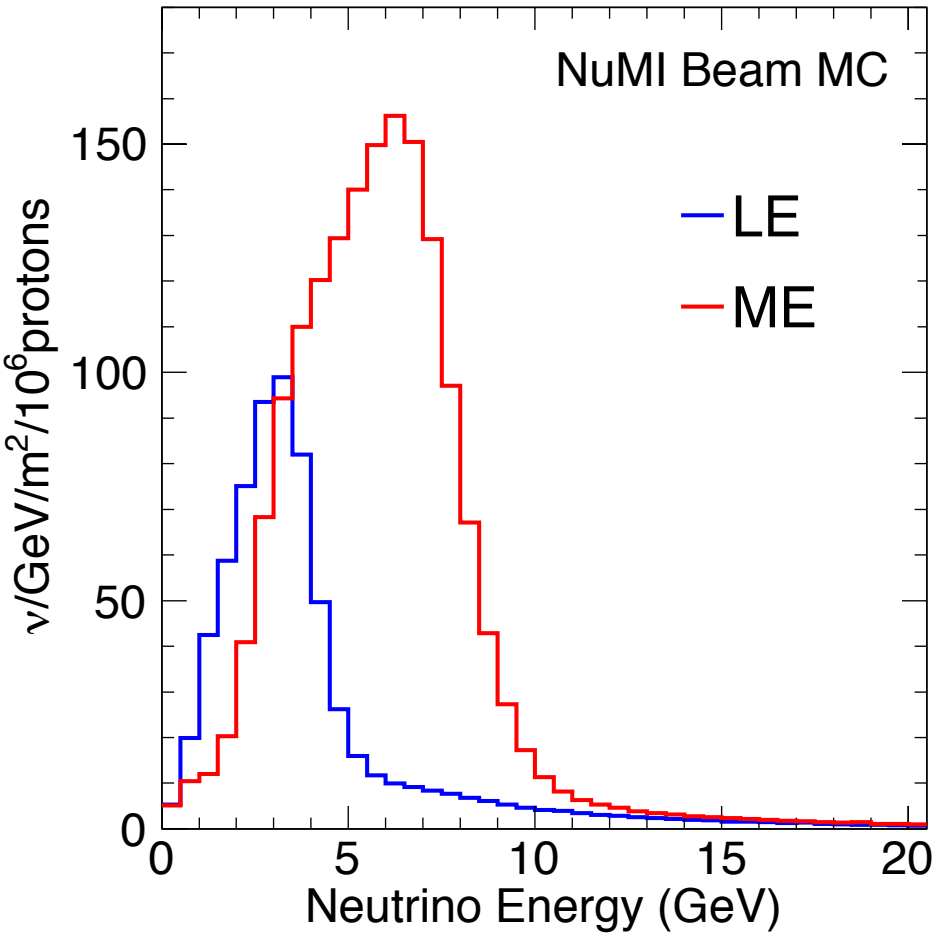

Figure 10: The flux as a function of the neutrino energy as predicted by gNuMI when the beam is in the LE and ME target/horn positions.

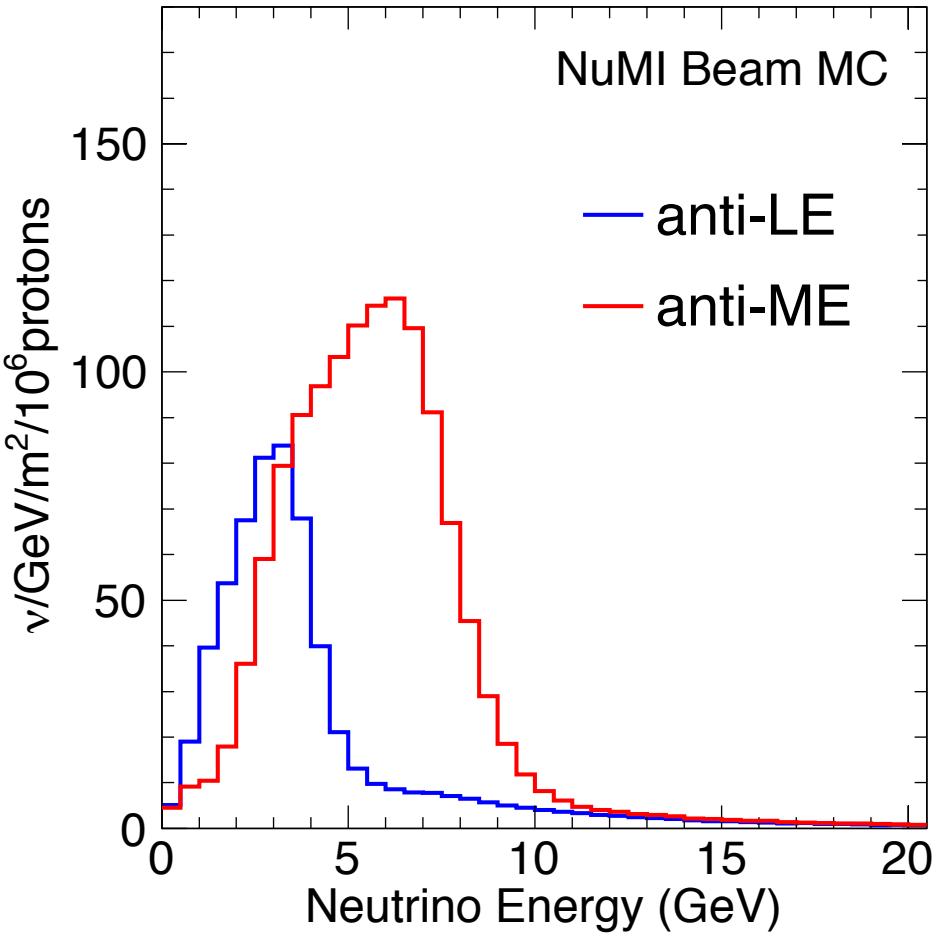

Figure 11: The flux as a function of the neutrino energy as predicted by gNuMI when the beam is in the LE and ME target/horn positions.

3.2 Flux and Flux Uncertainty

One of MINERνA's goals is to measure cross sections and therefore needs to know the flux of neutrinos produced. The flux is obtained via a monte carlo simulation of the entire above described system. The simulation is called g4numi, has been used by the MINOS experiment and will be used for the LBNE project. It is continually being updated with newer models and hadron production data. MINERνA is working with people at CERN to make hadron production measurements with an actual NuMI target and at actual NuMI proton energies to improve the beam simulation. The flux is a large source of uncertainty in any measurement that MINERνA will produce and there is much work done to understand it.

3.2.1 *In Situ* Flux Determination

MINERνA will be making flux measurements via other means as well. The various stations set up along the last 300m of earth take measurements as the muons are losing energy. The stations are composed of an array of ionization chambers. As the charged muons pass through the chambers they ionize helium gas and produce a current. This current can be converted to a muon flux which then can be turned into a neutrino flux. This is a newer method of flux determination for the NuMI beam, but it has been demonstrated in past experiments. This method was also the subject of a new MINERνA collaborator's dissertation but it will not be used in this manuscript, [16]. When the last ionization chamber is set up, more effort will be made to understand the neutrino flux with this method.

The MINERνA detector itself can be used to constrain the flux. The NuMI horn positions and currents are modified and then data is taken with the MINERνA detector. There are a number of different specific configurations of relative horn position and current used in these 'flux determining' data runs, see section 6.3.3 on page 88.

These data runs are analyzed and then compared to what is given in the beam simulation. The simulation can then tuned via these direct measurements. This method is also not currently being used, but is being developed now and will be used in the future.

Further analyses with the MINERνA detector will use these *in situ* methods in aiding the determination of the flux. As mentioned, these methods are simply too new and have very large errors. There is effort currently to better understand these methods, to reduce the errors and to use them for constraining the flux.

3.2.2 Hadron Production

The main source of uncertainty in the flux determination is the uncertainty in the number and energy spectra of the charged secondaries produced in the interaction of the 120 GeV proton with the graphite target. The hadron production data that goes into the monte carlo beam simulation comes from different initial particle energies and differing target structures. A comparison between the gNuMI monte carlo and NA49 data is shown in figure 12; data in the figure was taken at 49 GeV initial proton energy. As stated above, there is an effort to take 120 GeV proton thin target data and use the actual NuMI target in the NA61 experiment (61 GeV initial proton energy). Currently, differing existing hadron production data sets are compared to existing monte carlo predictions to set error bars (see section 7.8.2).

3.2.3 Other Sources of Error

The magnetic horns that focus the proton beam are one source of error. As stated above, the horns are set up to focus a very narrow momentum range of particles coming off of the target. The lack of hadron production knowledge directly feeds into the focusing error. The momentum spectrum of the particles produced in the original tar-

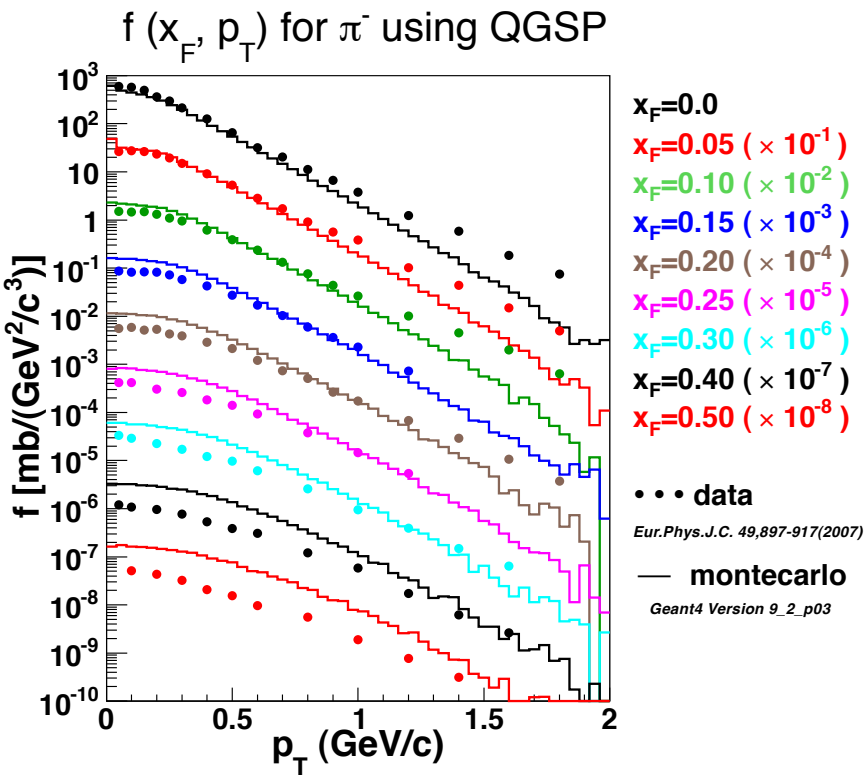

Figure 12: This plot shows the cross sections as a function of p_T for specific x_f slices for data and the gNuMI monte carlo.

get is unknown; so, the exact spectrum of particle momentum being focused by the horns is also unknown. This error peaks at the falling edge of the neutrino spectrum, see figure 13.

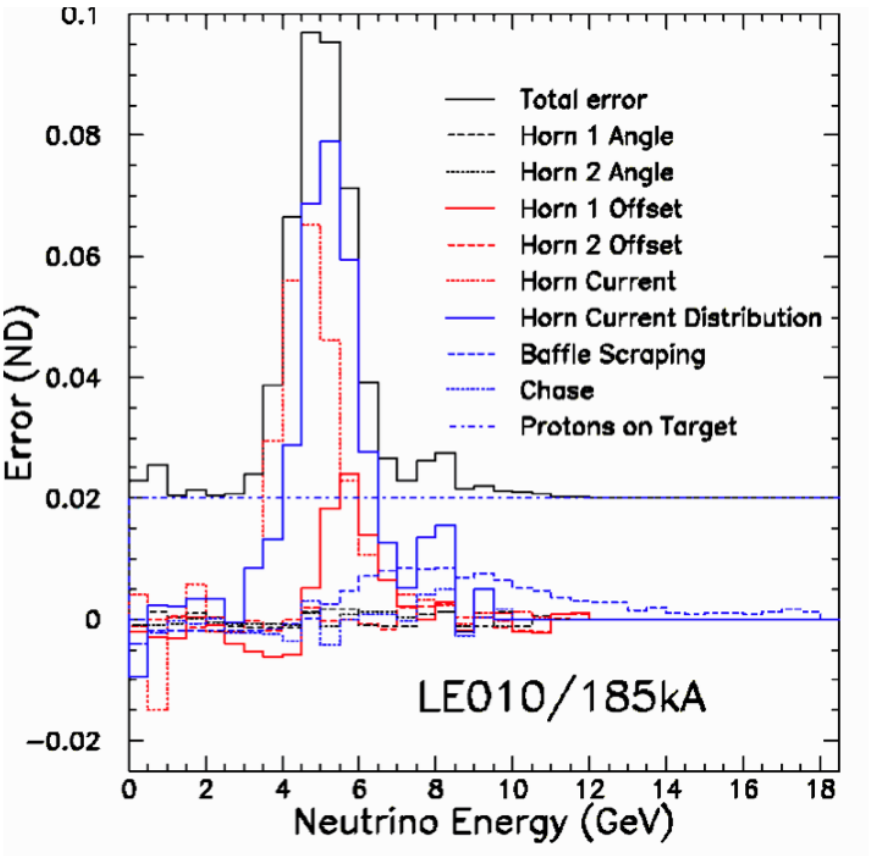

Figure 13: This plot shows the breakdown of the focusing errors of the NuMI beam at the detector. The error is the highest in the falling edge of the neutrino beam spectra, see figure 10.

Another source of uncertainty comes from the neutrinos produced in the downstream interactions of the charged secondaries: the initial pions and kaons can interact in the focusing horns or in the decay volume walls to produce a neutrino. This uncertainty is due to the uncertainty in modeling hadron production. This error is not that big because there are not as many neutrinos produced via these tertiary interactions and the majority of neutrinos interacting in MINERνA are from the original particle decays. Of course, many of these sources of error are correlated (i.e. a secondary whose

momentum is not known very well will get an unknown amount of focusing which can in turn could produce neutrinos from tertiary interactions in the target and/or hall walls).

3.3 Conclusions

The MINERνA detector was built to better understand neutrino cross sections. Any absolute measurement that could be made with the data requires an accurate knowledge of the flux. There is a dedicated effort to understand the flux being used being used in this experiment. So far, these efforts are being focused on the existing external hadron data and how to use this data to push down the flux errors. Current analysis has lowered flux errors from roughly 20% to around 12%. The new hadron production data from 120 GeV protons and/or the actual NuMI target will aid this error analysis greatly. A continuing effort will be made to further reduce this error; future endeavours will involve making hadron measurements with the NuMI target, using the NuMI target scans/MINERνA data to further constrain fits and also using data from the muon monitor chambers to get a better handle on the flux and corresponding flux errors.

Finally, it should be noted that it is an amazing engineering feat to build **and** maintain the NuMI beam. Many thanks are due and given to the engineering team at Fermilab that makes this intense, energy-tunable neutrino beam possible.

4 MINERνA Experiment

The MINERνA (Main Injector Experiment: ν-A) Experiment aims to make a precision study of neutrino interactions in the 1-20 GeV energy regions to aid oscillation studies in addition to provide insight into important stand-alone physics topics including precision measurements of M_A, the existence or absence of charged-current π production, strangeness content of the nucleon Δs, parton distributions at high x_{bj}, etc. MINERνA will make use of the intense NuMI neutrino beam to make important advances in the field of neutrino physics.

The author of this manuscript has been involved with the MINERνA Experiment since the project's inception. This means that the author has been involved with many different aspects of the experiment: design and optimization of the detector, the official experiment approval process at Fermilab, construction of the detector, monitoring of the experiment, monte carlo/software work and data analysis. The author also received experience in Department of Energy grant proposal writing[1]. The author's time on the MINERνA Experiment has been long, but it has yielded many different experiences and opportunities.

4.1 NuMI Hall and MINOS

The NuMI Hall is the current location of the MINOS near detector. The hall is roughly $4105m^3$ and $106m$ underground. It houses the semi-permanent MINOS and MINERνA detectors. Other smaller scale experiments have used the remaining space: ArgoNeut, COUPP, etc. MINERνA sits 2m directly upstream of the MINOS detector. This is crucial because MINERνA does not have a magnetic field and therefore relies on the MINOS detector to measure the momentum of exiting muons. All current MINERνA

[1]The author was the primary contact with the DoE on MINERνA at UC Irvine

analyses are limited to events in which there was a matched muon in the MINOS detector that was momentum analyzed (see section 5.4 page 71). This also means that any MINERνA data needs the corresponding MINOS data for the muon information. The combined live time of the MINERνA and MINOS detectors has been roughly steady at 95-97% throughout the entire MINERνA running. There have been a few instances of the MINOS detector having issues and losing muon data; these have only rarely lasted more than one day.

4.2 MINERνA Event Rates

MINERνA takes advantage of the intense NuMI neutrino beam at Fermilab. The existing run plan for the MINERνA detector is 4e20 POT of low energy (LE) NuMI exposure and 12e20 POT of medium energy (ME) NuMI exposure, see section 3 for an explanation of the different beam configurations. The event rates per 1e20 POT LE exposure for several charged current (CC) and the total neutral current (NC) processes are shown in table 3. These event rates correspond to a fiducial volume with Z extent of 240cm and a hexagonal apothem of 85cm.

Process	Events/1e20 POT LE Exposure
CC Quasi-elastic	50 K
CC Resonance	90 K
CC Transition	74 K 1.3¡W¡2GeV
CC DIS	137 K W¿2
CC Coherent	2.9 K
NC	128 K

Table 3: The event rates for different reaction types per 1e20 POT LE NuMI exposure. The rates listed are for event that occur in the fiducial volume of the detector. MINERνA has recorded 3.98e20 POT of LE data.

4.3 The MINERνA Detector

MINERνA is a segmented neutrino detector built with well-understood technology. The overall detector design is a hexagon roughly $3.5m$ across and $5.8m$ long consisting of an inner detector and an outer detector. The detector will add a wealth of knowledge to the neutrino field due the detector's overall good performance, see section 4.9.

As mentioned above, part of the author's initial work on MINERνA was detector optimization. There were two main areas of this work: optimization of the scinitillating elements of the detector and investigations into a magnetic field for the detector. The optimization work involved modifying the geometry and dimensions of the scintillator elements to determine what yielded the best light collection and coordinate residuals. Preliminary versions of the MINERνA detector included a magnetic field. The magnetic field was meant to increase overall MINERνA acceptance by bending more muons to have a trajectory that would intercept the MINOS detector (and therefore be momentum analyzed). It was determined that the benefit of a magnetic field did not outweigh other negative factors by it inclusion. This work was the subject of the author's Master's Thesis and will not be discussed further here.

4.3.1 MINERνA Modules

Neglecting the upstream veto wall and cryogenic target, MINERνA modules can be considered as 'slices of bread' which, when put together, make a full 'MINERνA loaf.' The entire detector, less previously mentioned sections, is segmented into modules of varying components based on location within the detector. This makes the detector installation and possible detector reconfiguration very simple. For example, the nuclear target modules could be easily switched around and/or swapped out for other modules. The bulk of the modules in the detector are the scintillator modules that make up MINERνA's target fiducial volume.

A single plane of scintillator is vacuum sealed twice with an upper and lower skin, a web layer between the adjacent 180° differing triangles, along with fiber routing trays and survey fiducials, see figure 14.

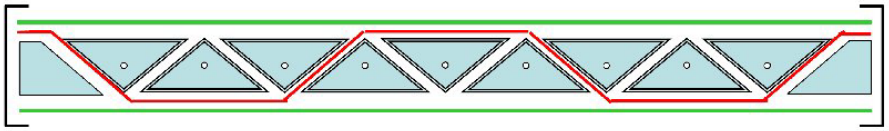

Figure 14: The cross-sectional layout of an active target scintillator plane. The green and red line represent the upper/lower skins and webbing, respectively.

A 2mm layer of an alloy consisting of Pb-Ca-Sn for structural support is then glued to this assembly and vacuum sealed a third time. This completes one plane of the detector. There are three different orientations of scintillator plane in the MINERνA detector to aid track reconstruction. The orientation of the scintillating planes are labeled X,U,V and the U and V planes are offset by $\mp 60°$ relative to the X orientation. Two of these assemblies of differing views, UX or VX, are then attached together to create a completed ID module. The electromagnetic and hadronic calorimeter modules differ slightly from what was just described and will be discussed below. The OD frame is made from trapezoid steel pieces that have slots cut out for outer detector scintillating elements. These elements have a square, instead of triangular, cross section, see figure 15. The light collected from the OD serves a calorimetric, rather than tracking, purpose and therefore can be 'coarser' in design. Six of these outer detector frames are then welded together to form a hexagon-ring OD module. The active XU or XV ID module is then bolted inside of the OD module to craft the finalized hexagonal MINERνA active target module. A single view plane, complete with OD, is shown in figure 16.

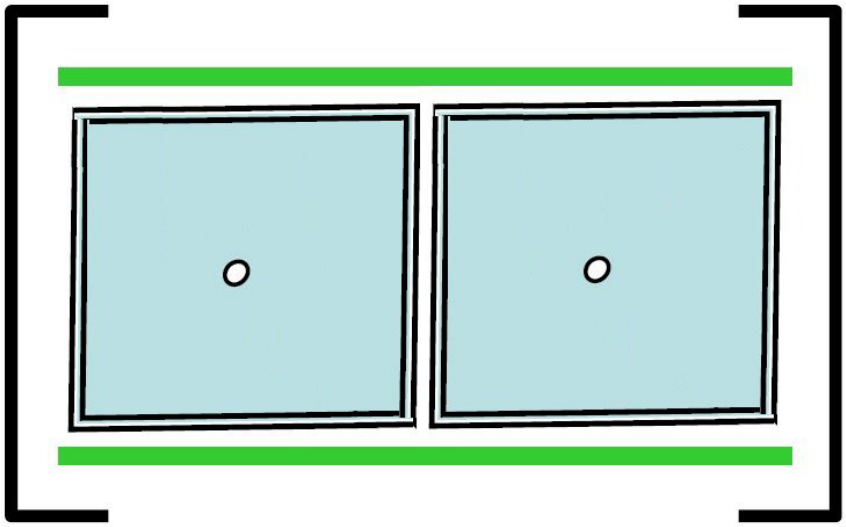

Figure 15: A simplified picture of the outer detector scintillator bars.

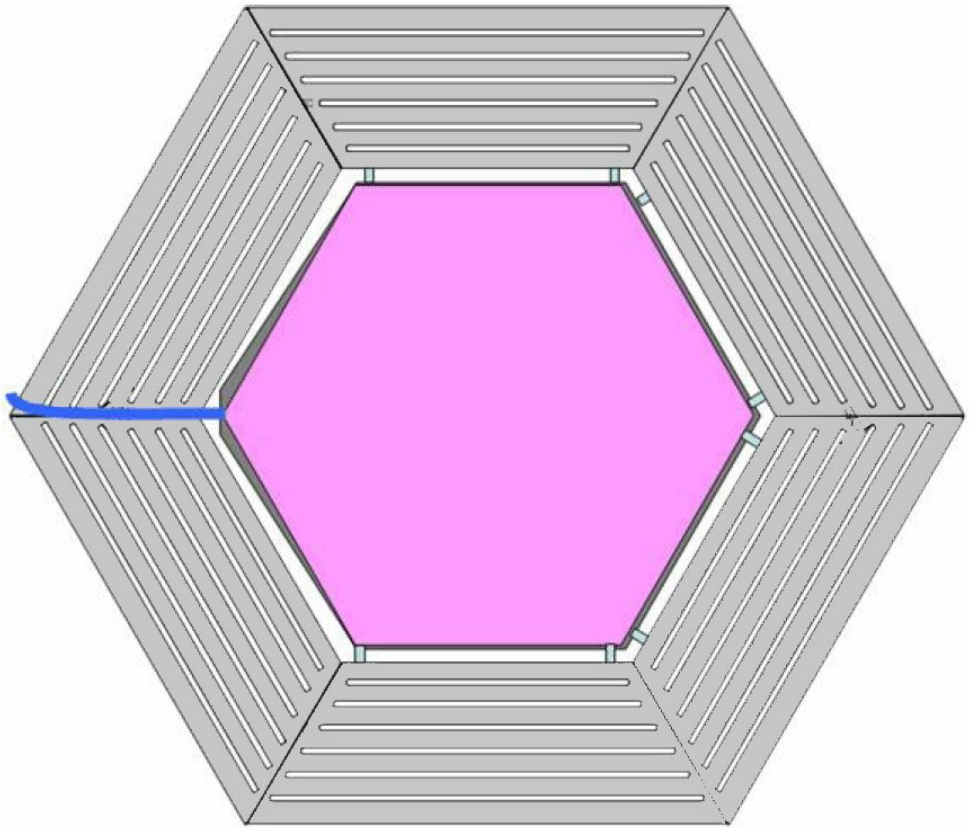

Figure 16: Detailed view of an active target module, note shown are supports for detector installation

4.3.2 Veto Region

Traveling along the path of the neutrino beam, MINERνA consists of a steel veto shield and a veto wall. The steel shield blocks any possible stray non-muon particles from the neutrino interactions that occur in the hall walls. The veto wall is a refurbished version of an older experiments veto wall. It serves to tag any muons that may pass through. The veto wall data will be very important when analyzing the data for possible neutrino interactions from the cryostat and upstream nuclear target region. Muon tracks from these interactions can be extrapolated back to the veto wall to look for coincidences to verify they are indeed muons from the neutrino interaction in the detector and not simply through-going muon tracks.

The proton beam that begins the NuMI beam is very collimated, but the neutrino beam has a radius of about a meter at the face of the MINERνA detector. Recall that the distance to the MINERνA detector is roughly 1km, see section 3 on page 25. A 1° angular deviation at the start of the beam will yield a 17m transverse displacement when reaching the MINERνA detector. This means that if a neutrino undergoes an interaction upstream of MINERνA but still close enough so that the muon does not range out, the resulting muon will, in most cases, follow closely along the neutrino direction. The result is a non-negligible flux of muons through the detector, see section 5.5.1 on page 73.

4.3.3 Nuclear Target Region

In the path of the neutrino, next comes the nuclear target region with varying thicknesses and configurations of helium, carbon (graphite), water, iron and lead targets. The exact composition of the nuclear target region, including the liquid target in the cryostat, changes depending on the MINERνA data set being analyzed, see section 6 on page 85.

The original nuclear target design is shown schematically below, with the most upstream section on the left. Each M represents one scintillator module, either a UX or VX. Note that the presence of two scintillator modules upstream of the target region will allow tracks to be extrapolated back to ensure neutrino interactions occured in the upstream target(s) and serve to veto through-going particles.

MM Pb/Fe MMMM Pb/Fe MMMM Pb/Fe/C MMMM [gap] MMMM Pb MMMM Pb/Fe

The targets will be referred to by number starting on the left, upstream target: Pb/Fe - target 1, Pb/Fe - target 2, Pb/Fe/C - target 3, Pb - target 4, Pb/Fe - target 5; see below for discussion on the gap. Recall that the inner detector portion of a module is a hexagon; the overall nuclear target shape will be this hexagon that is made of varying shape pieces of the individual material. The nuclear target modules 1 and 2 will be made of 2.54cm thick Pb and Fe. The total area breakdown of the lead and iron in these modules is 40% and 60%, respectively. This combination yields approximately 225kg of both lead and iron inside the fiducial apothem for most analyses, see 7.2.1 on page 92. These first two modules will be rotated with respect to each other during installation to account for possible differences in event acceptance and/or reconstruction. Target 3 has a more complicated structure as it consists of three materials of different thickness. The lead and iron, again, will be 2.54cm thick, but the carbon (graphite) will be 7.62cm thick. The area breakdown of target three is 20%, 30% and 50% for Pb, Fe and C, respectively, which gives the materials masses of 110kg, 110kg and 140kg (again, respectively). The presence of three materials in the same target module will allow for detailed studies of the neutrino interaction A dependence. Target four is comprised of only 0.76cm thick lead with a total mass of 170kg. This module will serve both as a target and for containment purposes. The module is about 1.5 radiation lengths so that any electromagnetic particles going either downstream or upstream will start to shower. The final nuclear target module, target 5, is 1.27cm thick lead and iron of mass totals 115kg for both (the target is 40% Pb and 60% Fe). The fully active scintillator region begins directly downstream of target five to ensure detailed studies of multiplicity and lower energy particles

from interactions in this most downstream target. Preliminary studies show that the higher energy deep inelastic scattering events are contained with only approximately 10% probability of energy leakage for hadronic energies around 10-12GeV, see figure 17. The total mass of the graphite, iron and lead targets is 140kg, 685kg and 855kg, respectively. The expected number of charged current events from these masses are about 2.0 million for Fe, 2.5 million for Pb, and 400,000 for C.

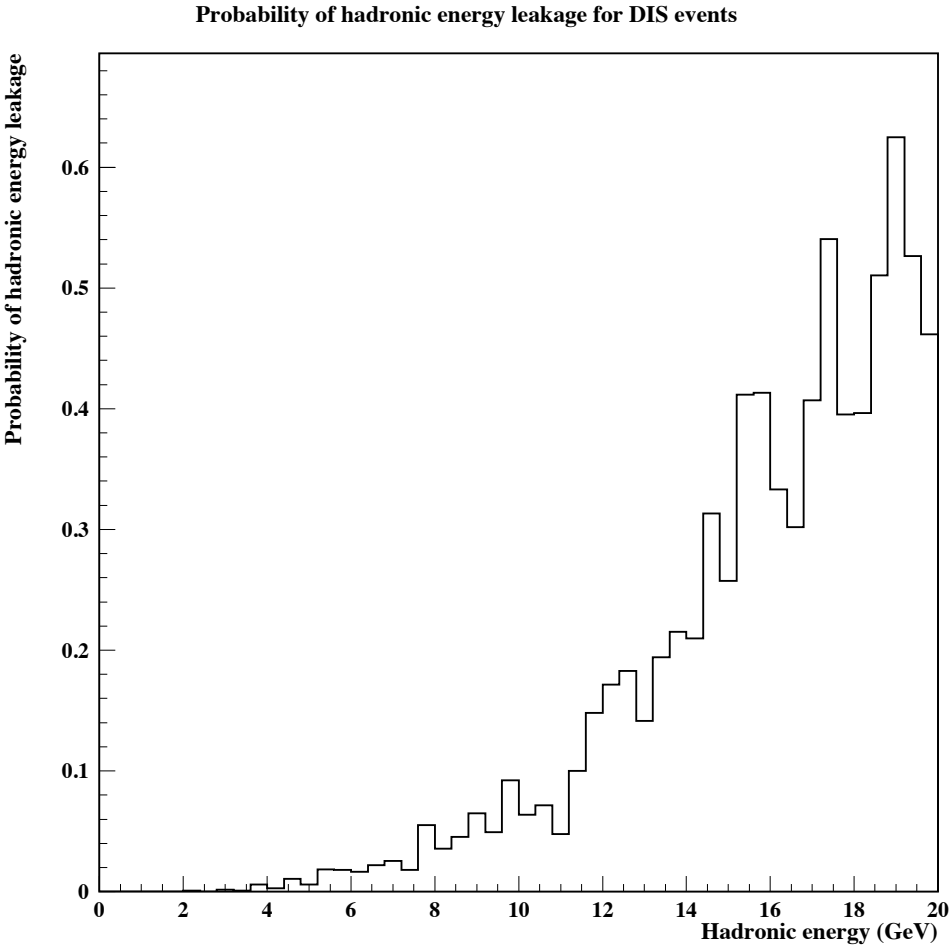

Figure 17: The plot shows the probability of energy leakage for deep inelastic scattering events (generated by the GENIE simulation) as a function of the total hadronic energy in the event. One can see that this simulation shows that there is only a 25% chance of leakage for hadron energies around 15GeV.

The gap shown in the nuclear target schematic was for a water target. There were some issues in the construction of a 'vertical water column' that could be made with a relatively low A material; initial designs suffered leaks. In the end, a design comprised of acrylic supported by

kevlar restraints was installed in November 2011. This date falls in the middle of the second neutrino data set. The original install date was September 2011 between the $\overline{\nu}$ and ν data sets, see section 6 on page 85. The total mass of water in the target is 500kg.

A special liquid helium cryostat was designed to expand MINERνA's different A measurements. The cryostat needed to be extra thin on two surfaces as to allow the smallest material for the NuMI beam to pass through. The vessel was constructed from aluminum and is the shape of a cylinder with a 152cm diameter and 150cm total length. The outer vacuum vessel was also made of aluminium and had a 183cm diameter and 249cm overall length. The liquid helium is kept at the needed temperature by a 1.5 watt cryo-cooler. The cryostat was filled in September 2011 between the $\overline{\nu}$ and ν data sets. There are also special data runs taken with the cryostat empty to study systematic errors. In an effort to make further A measurements, MINERνA is attempting to fill the cryostat with liquid deuterium. There are extra precautions, safety and otherwise, that need to be taken in order to do this, but these are being undertaken. Barring unforeseen difficulties, MINERνA will also be able to ^2H to its list of nuclear targets.

The total masses for all of MINERνA's targets and various event rates are shown in table 4.

Target	graphite	iron	lead
Total Mass	140kg	685kg	855kg
CC Events per 1e20 POT	11282	67294	73404
Target	helium	water	
Total Mass	250kg	500kg	

Table 4: The total masses of various targets used in the MINERνA experiment. Rates are listed for the targets that were in place when the detector construction was finished, March 2010.

4.3.4 Tracking Region

The main scintillating volume is directly downstream of the heavy target region. Many neutrino experiments have made use of scintillation extrusions for event detection: MINOS,

SciBar, CDF and CMS calorimeters. The scintillating elements used in the MINERνA detector are 1.7cm by 3.3cm triangular extrusions. A total of 127 extrusions are fit together, alternating up and down triangles, to form a plane of length 2.2m, see figure 14 on page 42. A wavelength shifting fiber is fitted through a central hole in the triangles for light collection, see figure 18. The central hole was chosen after running monte carlo simulations of varying the position. Simulations were also used to determine the triangular shape of the extrusions. Most particles will pass through two triangles in any given plane leading to light being deposited into both. Charge sharing in the two triangles allows for track coordinate in a plane to be constructed out of two detector coordinates leading to better spatial resolution of the track coordinates, see section 5.1.1 on page 63.

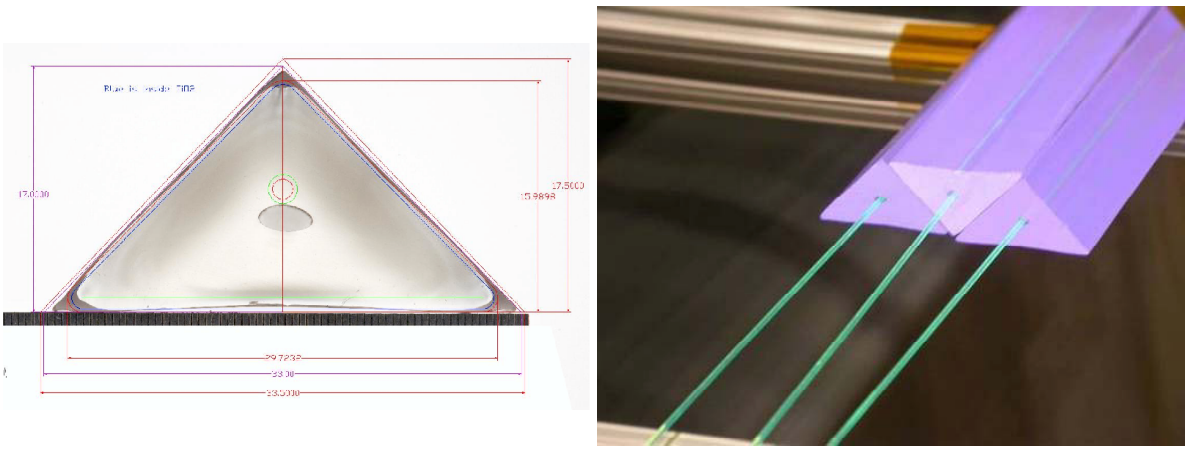

Figure 18: Left: The design and actual single scintillator bar used in the MINERνA experiment. Right: A few scintillator bars used in the setup of a vertical slice test of the MINERνA detector.

The total scintillator plastic fiducial volume, see section 7.2.1 on page 92, has a mass of 5470kg. The density of the scintillator is low and the fine sampling will enable MINERνA to make quality measurements: detector of low Q^2 recoil protons in quasi-elastic interactions, good particle identification via dE/dX, photon tracking and multiplicity counting in higher energy events. At the same time, the low density makes the inner active target module incapable of containing most events. A side calorimeter was introduced in these planes and is described below. There are a total of 62 plastic scintillator modules or 124 individual measurement planes in the active region of the detector. This is a distance of approximately 2.8m. This

distance allows particles to separate before they enter the calorimeters and also provide many separate measurements to reduce detector coordinate residuals.

4.3.5 Calorimeters

The MINERνA detector has both electromagnetic and hadronic calorimeters (ECAL and HCAL, respectively) downstream of the main plastic volume. The calorimeters serve to contain the various particles created by the neutrino interactions in the detector. The modules that make up the ECAL and HCAL follow the same basic design as the scintillator modules, yet with slight changes.

The downstream ECAL modules include the addition of two 2mm lead sheets. The 2mm lead sheet is attached to the single MINERνA plane (recall that two of such planes make up an ECAL module); an ECAL module is the typical UX/VX structure of the scintillator modules. There are a total of ten ECAL modules in the MINERνA detector. This is a total of 4cm of lead and corresponds to about seven radiation lengths. Photons of energy around 1 GeV will lose 99% of their energy in this distance. Of course, electromagnetic particles from interactions will travel varying distances through the ECAL depending on their creation point and trajectory.

A collar made of trapezoidal sheets of 2mm thickness lead and iron alloy surrounds an area from the outside edge of the inner detector frame to approximately 20cm radially inward to serve as a side electromagnetic calorimeter. This will help to contain forward going events that occur nearer to the edges of the fiducial volume.

Downstream HCAL modules are more of a modification from the original tracker modules than the ECAL ones. The HCAL modules have only one sheet of scintillator and a 2.54cm layer of iron; hence, each HCAL module has either an X, U or V view detector plane. There are a total of 20 HCAL modules in the MINERνA detector. Note that the total number of sampling points in both the ECAL and HCAL is the same. The combined thickness of the

4cm of Pb in the downstream ECAL and the ≈50cm of Fe in the HCAL will stop muons up to about 600 MeV and protons with kinetic energy up to about 800 MeV.

Although not designed for calorimetry, the upstream targets can also serve as a calorimeter. The variation of the structure the different targets means that the 'upstream calorimeter' ability to contain will depend on the spatial location in the detector. The bulk of backwards going particles created in neutrino interactions are low energy and no leakage of backward going energy is expected.

4.3.6 Outer Detector

The outer detector (OD) will serve to contain hadronic showers and force lower energy particles produced in the upstream active target region to range out. As mentioned above, the outer detector is made from six trapezoidal sheets of iron, with four slots cut for scintillator elements, joined together to form a hexagon. The coarser design makes the tracking and calorimetric capabilities of the outer detecror not as good as the tracker or other calorimeters. But, the OD will certainly add information of the transverse containment of any neutrino interactions.

4.4 MINERνA Test Beam Detector

In order to calibrate the MINERνA detector, a smaller Test Beam version of the detector was built. This consisted of forty modules of a smaller 1m by 1m square detector modules; other than the shape, modules were made exactly the same as the main detector. The test beam detector had two different configurations: 20 tracker modules/20 ECAL modules and 20 ECAL modules/20 HCAL modules. The test beam detector was run at Fermilab's new Test Beam facility. The data analysis of the test beam set is currently underway. Once this analysis is complete, this data set will provide: potential data/MC differences in energy loss, verification of MINERνA's particle identification, and potentially other interesting measurements (the temperature dependence of the light output of the scintillator was measured after

it was found to be abnormally hot in the test beam experimental hall).

One last step to creating a cross section for the two-track analysis channel would be to measure data/MC differences from protons using the test beam detector. These piece of information was not extracted in sufficient time and could not be provided until early 2013.

4.5 Readout and Electronics

The detector is readout by wavelength shifting fibers that are fit into the central hole of the triangular scintillating element. The fibers are mirrored at one end to read out the detector on one side. The green wavelength shifting fibers are attached to clear cables of varying length. The clear fibers are then routed into the photomultiplier tube. The experiment uses the R7600-00-M64 multi-anode photomultiplier tubes from Hamamatsu Photonics. These are 2cm x 2cm, 8 x 8 pixel PMTs, i.e. 64 pixels with effective dimensions 2 x 2mm^2. The electronics used for the experiment are a modified version of an previously existing front-end board. The electronics board is attached to the photomultiplier tube boxes. The electronics boards are responsible for digitizing the signals from the detector, providing timing information and high voltage to the PMTs. These 473 electronics boards are connected to 40 LVDS (CAT-5e) chains which are connected to 12 chain readout-out controllers. These readout controllers serve a variety of purposes: synchronize timing throughout the whole system, initialize readout of the detector systems and store the resulting data. The whole system is read out by one computer. This is a very limited description of the readout system; for more information see the recent publication describing this system [17].

4.6 Neutrino Event Generation

The MINERνA experiment uses GENIE [18] for neutrino event generation. GENIE is currently being used by the experiments: T2K, NOνA, μBooNE, ArgoNEUT, LBNE, INO, IceCUBE, among others. There are currently three members of MINERνA that are also in

the GENIE collaboration; this ensures that we always have the most up-to-date versions of the generator. The full details of the generator can be found at: *www.genie-mc.org*. A few of the relevant details of some of the models will be mentioned here.

4.6.1 Nuclear Physics Model

The GENIE MC uses the relativistic Fermi gas model (RFG) in its calculations and a particle version that uses short range nucleon-nucleon correlations [19]. For $A \leq 20$, the modified Gaussian density parameterization is used. For all others, a two parameter Woods-Saxon density function is used:

$$\rho(r) = N_0 \frac{1}{1 + e^{(r-c)/z}}$$

Where c and z represent the size and width of the surface of the nucleus. For ^{56}Fe, c=4.1fm and z=0.55fm. The fit parameters of the nuclei being simulated are calculated from interpolations from the data of measured nuclei. The RFG and impulse approximation seem to work at the lower GENIE energy ranges (the simulation's range is 100MeV-500GeV). Modifications need to be made at the higher energy ranges due to a variety of nuclear effects: Pauli blocking, shadowing, anti-shadowing and the EMC effect. It is well known that nucleons in a nuclear environment are different than those of free nucleons. MINERνA will be able to assist this situation by having (at least) five different nuclear targets that will be measured by the same beam. Recall that most other data comes from multiple experiments and detector/beam effects have to be taken into account when comparing the extracted data. This, more often than not, leads to biases in the extracted data.

4.6.2 Cross Section Model

A few of the relevant formulas will be shown here, but this section has some overlap with section 2.

For charged current quasi elastic scattering, GENIE uses the Llewellyn-Smith model [20]. This model assumes the hadronic current is written as:

$$\Gamma_\lambda = \gamma\lambda F_V^1(q^2) + \frac{\iota\sigma_{\lambda\nu}(\mu_p - \mu n)F_V^2(q^2)}{2M} + \frac{q_\lambda F_V^3(q^2)}{M} + \gamma_\lambda\gamma_5 F_A(q^2) + \frac{q_\lambda\gamma_5 F_P(q^2)}{M} + \frac{\gamma_5(p_1+p_2)_\lambda F_A^3(q^2)}{M}$$

Here,

- $(\mu_p - \mu n) = 4.71$
- $F_V^{1,2}$ can be related to electromagnetic factors via the conserved vector current theory (the BBBA05 versions of the electromagnetic factors are used [2])
- the assumption of no second class currents sets $F_{V,A}^3 = 0$
- F_P, F_V^3 are proportional to the lepton mass and therefore small
- F_P can be related to F_A via the partially conserved axial current theory

Electromagnetic form factors are known very well through extensive experiments. This leaves the only unknown F_A which is modeled as[2]:

$$F_A(Q^2) = \frac{F_A(0)}{(1 + Q^2/M_A^2)^2}$$

[2]See the Physics section for more details about the recent experimental controversy of the axial form factor.

GENIE uses the dipole form for the axial form factor. This has one free parameter, M_A, that is set to a value of 0.99 GeV/c^2. The world average of this parameter is around 1.03 GeV/c^2, but measurements 30% higher have been reported recently, see section 2 on page 3. MINERνA will add more data and information regarding the axial parameter from CCQE analysis of ν_μ 1,2-track samples and also analysis of $\overline{\nu}_\mu$ CCQE.

For charged current quasi-elastic scattering from nuclear targets, a suppression factor, k_f, is used in the GENIE model. The model has the simple requirement that the ejected nucleon exceed the value of k_f for the nuclei in question. The k_f values GENIE uses are:, 0.221 GeV/c for nucleons in ^{12}C, 0.251 for protons in ^{56}Fe and 0.256 for neutrons in ^{56}Fe.

GENIE uses resonance models from Rein-Sehgal [21]: there are a total of 16 resonances included and the value of the resonance axial mass is 1.12 GeV/c^2 (recall that the lepton mass term is not included in the calculations). The deep inelastic physics used in GENIE are Bodek-Yang models[22]. Coherent neutrino-nucleus scattering is modeled after Rein-Sehgal models. There are currently no meson exchange current or n particle/n hole models employed in GENIE, but this is coming in future releases according to the GENIE authors. Using the current selection (see 7.2 on page 92), the main background is from the resonance channel; hence, these resonance models are of interest.

For neutral current elastic scattering, GENIE uses the model discussed in Ahrens [14].

$$G_A(Q^2) = \frac{0.5 G_A(0)}{(1 + Q^2/M_A^2)^2}(1 + \eta)$$

where $\eta = 0.12$. This is mentioned because the author spent some time investigating the neutral current channel before switching to the 'easier' charged current version.

4.6.3 Intranuclear Hadron Transport

There is much data to suggest that the hadrons produced in interactions can be modified while exiting the nucleus. The original hadrons can lose energy and/or change direction, new hadrons can be created, others can be absorbed: pions can be absorbed in the current versions of the GENIE code, but protons and neutrons can not be absorbed. Roughly 20% of the time in GENIE, resonant pion production events have the original pion absorbed. The event topology then mimics a charged current quasi-elastic interaction. Also, there is a chance that an original CCQE event undergoes a final state interaction that produces multiple hadrons. This signal event then will be not identified as a (in this analysis, a two track) CCQE event; this situation occurs approximately 35% of the time. More data needs to be taken with neutrino targets, preferably multiple targets in the same beam to add to this information to neutrino generators (i.e. MINERνA capabilities).

The INTRANUKE model employed in GENIE is a data-driven model. It uses pion/nucleon total cross sections that are calculated up to 1.2 GeV. The agreement between the model and existing data is not perfect and therefore GENIE normalizes the cross sections to the data at lower energies. GENIE also uses a formation time of 0.342 fm/c in which nucleons can react after being produced. There is a lot of final state interaction data for 50-300 MeV. This is not the case for higher energies and the calculations do not show the best agreement with the data. The calculations in GENIE were made on iron for application to the MINOS experiment. For targets other than iron, a $A^{2/3}$ scaling is applied. In cases with multiple particles ejected from the nucleus, the angular and energy distribution are sampled from template distributions from the relevant data. This model is fully reweightable and allows extraction of final state interaction systematic errors. For more details on this transport code see the original GENIE documentation [18].

4.7 GENIE Reweighting

Many of the parameters that are used in the GENIE simulation are readily reweightable and these weights are computed automatically in any MINERνA monte carlo job run with the appropriate options enabled. These pre-defined weights in the GENIE simulation that can be used to estimate systematic errors. There are weights for each individual scattering process in addition to the above mentioned final state interaction weights.

Process	weight name	function	1σ range
CCQE	MaCCQE Normalization	adjust QE M_A	(-15%,25%)
CCQE	CCQE Normalization	adjust overall CCQE	(-20%, 15%)
CCQE	CCQE Shape	adjust M_A Shape	(-10%, 10%)
CCQE	Vector CCQE Shape	changes to dipole form	(-)
CC Resonance	CCRes normalization	adjust overall CCRes	(-20%, 20%)
CC Resonance	CCRes M_A	adjust Res M_A	(-20%, 20%)
CC Resonance	CCRes M_V	adjust Res M_V	(-10%, 10%)

Table 5: The table lists some of the reweighting factors that are relevant for this analysis. A full list can be found in the GENIE reference [18] and the reweighting itself is described in section 7.7.

GENIE reweighting is described in more detail in section 7.7.

4.8 MINERνA Monte Carlo

The manual for the MINERνA simulation is mostly (and unfortunately) code and doxygen based. This section of the dissertation will not serve as a software manual in any sense. Aspects of the simluation that author was involved and assisted in will be briefly mentioned here.

There is one important note about the monte carlo that is also mentioned later in section 7.3.2. The decay of charmed particles is (currently) not handled correctly in the simulation. This necessitated that any event with a charm particle was not analyzable. When restricting the event topology to a two-track charged current quasi-elastic final state, the fraction of events with a charmed particle is very small.

The monte carlo simulation for MINERνA was and is a formidable task. The author helped create this simulation from a basic fortran simulation to a much larger C++ based project involving an externally managed framework and other packages. This work included: generation of a detector geometry for input into GEANT3/4, creation of the original event model for the simulation, the sole author of the original reconstruction code, a major contributor to all reconstruction code, sole developer of pattern recognition schemes for the experiment, developing original version of the muon matching software and creation of code that uses rock muon tracks to debug the detector-space to electronic-space mapping for the experiment. Some of these are described elsewhere in this document. The major tasks are listed here, but there are countless minor tasks that could be included as well.

An equally as important task as the development was the education of other collaborators. The author was the point of contact for most software related questions during the beginning stages of the MINERνA experiment. This work also involved traveling to Fermilab and giving presentations on the function, use and development of the software to the newer (and older) members of the collaboration.

4.9 MINERνA Performance

This section will show several plots illustrating the performance of the MINERνA detector: some of the plots are for the general performance of the detector, like the muon angular residuals, and some are analysis specific, like the proton energy residual for the two-track analysis.

The muons that are created in the experimental hall walls are used by a number of algorithms by the experiment. These rock muons, see section 5.5.1, provide: an energy calibration source, a timing calibration source and a readily available sample of through-going tracks to test/validate reconstruction. One of these tasks involves using the rock muons to align the various elements of the detector. The author wrote the original alignment package and routines, but these were modified and taken over by another student at UC Irvine. The alignment

code takes through going tracks and compares the computed position in detector plane to the projected track position with the plane being studied removed from the fit. By looking at the offset from nominal versus different quantities, any inter-plane position and rotational shifts can be removed. Figure 19 shows the effect of alignment scan on plane shifts and rotations; after one alignment scan the detector shows vast improvement in measured shifts and rotations.

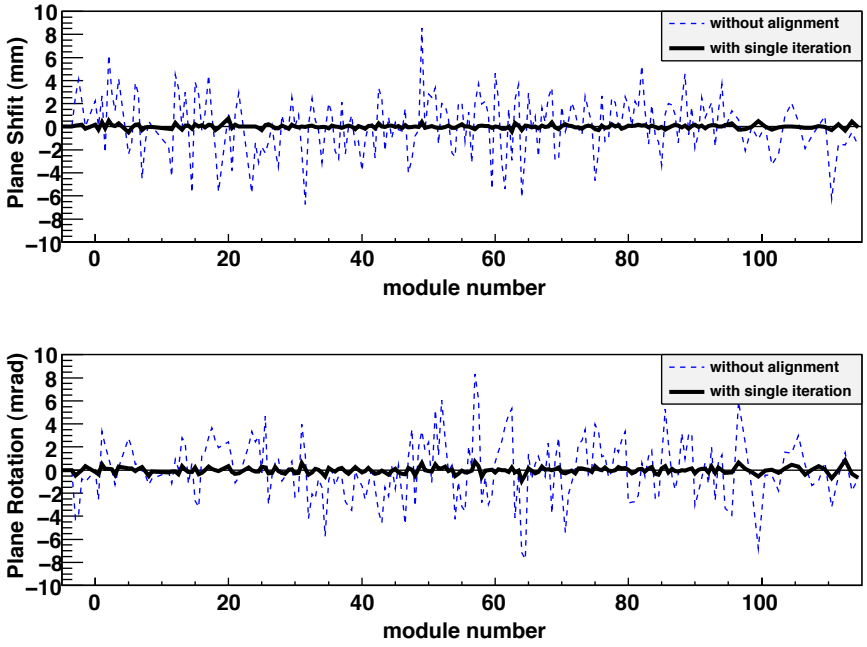

Figure 19: This shows the average plane shift and rotation before and after one iteration of the alignment code. Both the shift and rotation mean are zero which indicates successful alignment.

Angular residuals of tracks reconstructed in the detector are on the order of a degree. The residuals for both pattern recognitions can be seen in figure 20 on page 59. The performance of the long pattern recognition can be seen in the left panel; the gaussian fit σ is less than a degree. The angular performance for the second track in this analysis (i.e. the proton) can be seen in the right panel of figure 20. It should be noted that approximately 70% of the reconstructed second tracks were created with the short track pattern recognition. This plot can be thought as illustrating the performance of the short pattern recognition.

The vertex position residual is fit to a double gaussian to benchmark the performance. The

sigma and mean of the primary gaussian represent the resolution and pull of the fit, respectively. The results of the vertex fitting procedure tested on a sample of charged-current neutrino events is shown in table 6.

	No Fit	Initial Guess	Adaptive Kalman Fit
X resolution(mm)	4.61	3.62	3.54
X pull(mm)	0.02	0.06	0.09
Y resolution(mm)	5.07	4.45	4.28
Y pull(mm)	-0.21	-0.20	-0.23
Z resolution(mm)	NA	7.88	7.82
Z pull(mm)	NA	1.99	2.28

Table 6: Performance of the vertex fitting procedure. The vertex for 'No Fit' is the most upstream node of the anchor track. The Z residuals in the 'No Fit' case do not resemble a Gaussian distribution because the reconstructed Z position is restricted to the center of a plane (i.e. at 17mm intervals).

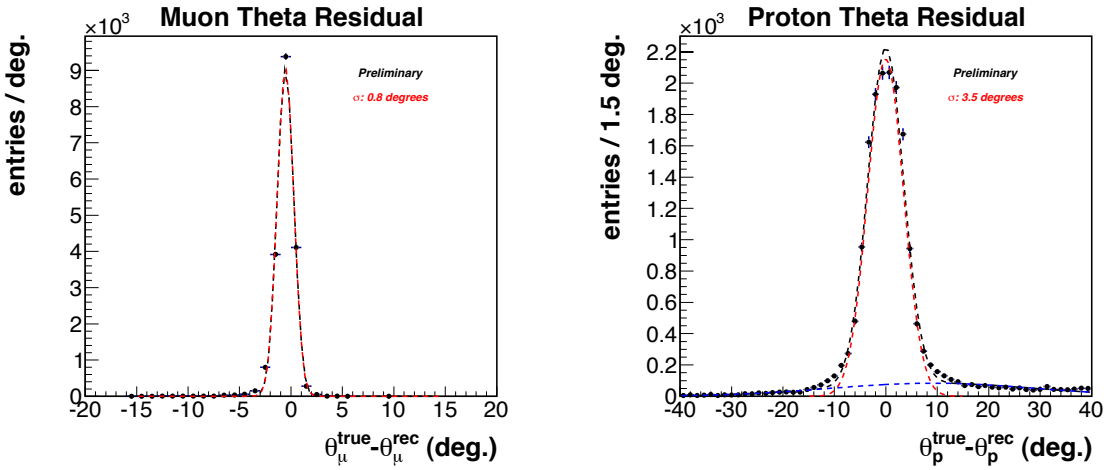

Figure 20: Left: This plots shows the angular residual of θ for the muon track. The longer, muon tracks show residuals less than a degree. Right: This plot shows the residual of the angle θ_p for the second track used in this analysis. Approximately 70% of the tracks used in the two-track analysis are found by the short pattern recognition.

The two track selection Q^2 residual is shown in figure 21. The simple gaussian fit parameters are shown on the plot. The fit sigma has a reasonable value, but there is a slight shift in the distribution. This is due to the track cleaning issue that is mentioned in the reconstruction

section 5. Energy is removed from around the muon track to improve fitting, but this has the effect of degrading energy residuals/resolutions. There have been multiple versions of the cleaning code implemented and it is still an issue that is being investigated.

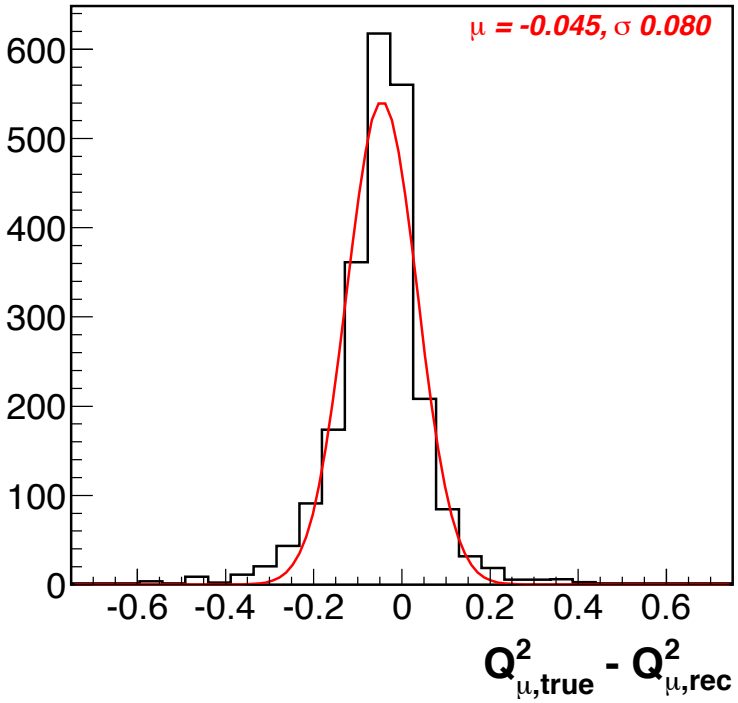

Figure 21: The Q^2 residual for the two-track selection is shown. There is a slight bias in the distribution due to the ongoing track cleaning issue.

The two track CCQE protron momentum residual is shown in figure 22. Both plots in the figure have the two track signal selection applied, see section 7.2. The left plot shows the residual broken down by the GENIE interaction channel. The simple gaussian mean of the quasi-elastic protons has a mean of zero and a sigma of 44 MeV. The right plot shows the residual broken down by the number and type of GENIE final state particles. It should be emphasized here that the actual particles that are seen in the detector can vary due to re-interactions of these GENIE final state particles.

The calorimeter energy resolution and first estimates of the systematic error as functions of the recoil energy are shown in figure 23. This information is not relevant to this analysis, but

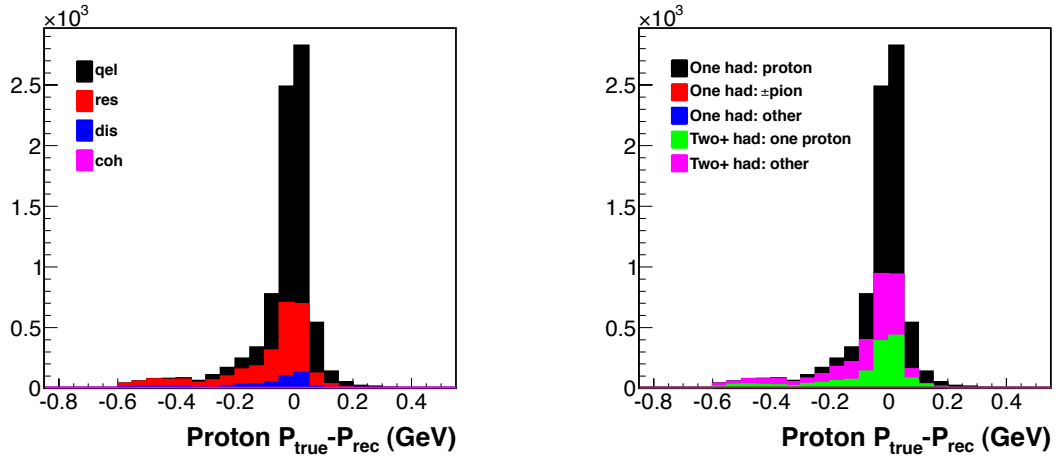

Figure 22: Left: This panel shows the proton momentum residual for the different GENIE interaction channels. Right: The proton momentum residual for the different GENIE final state particles ejected is shown. Both panels have the standard two track event selection applied.

is useful for various inclusive MINERνA analyses.

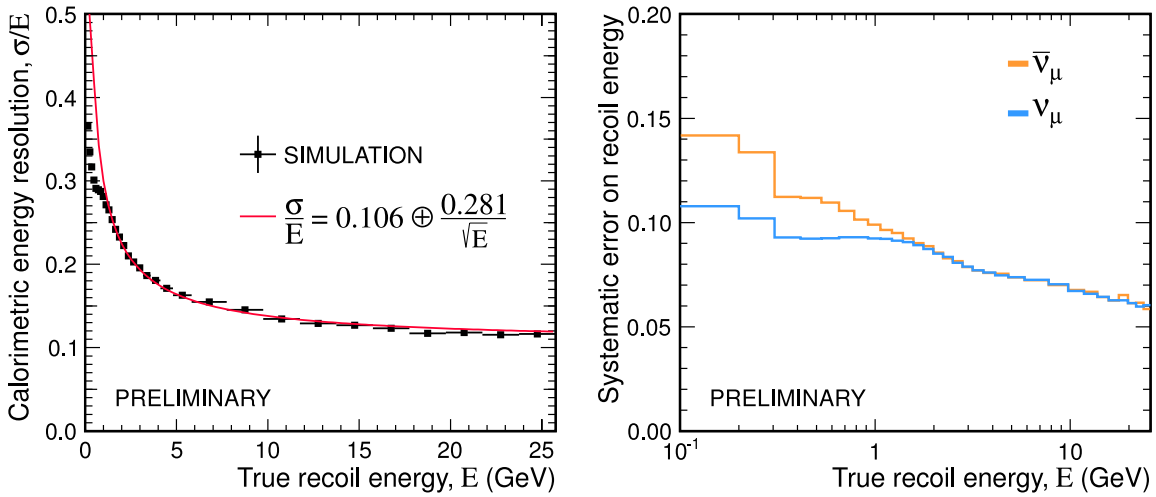

Figure 23: Left: This panel shows the energy resolution as a function of the recoil system. The fit to the simulation is also shown. Right: The first estimation of the systematic error on the recoil energy system is shown as a function of the recoil energy.

The data set used in this analysis (see section 6) was tested for abnormalities and/or oddities. The figure 24 shows the total number of charged current candidates as a function of time for the analysis playlist. One can see that the number of candidates is relatively constant over the total length of time of the playlist.

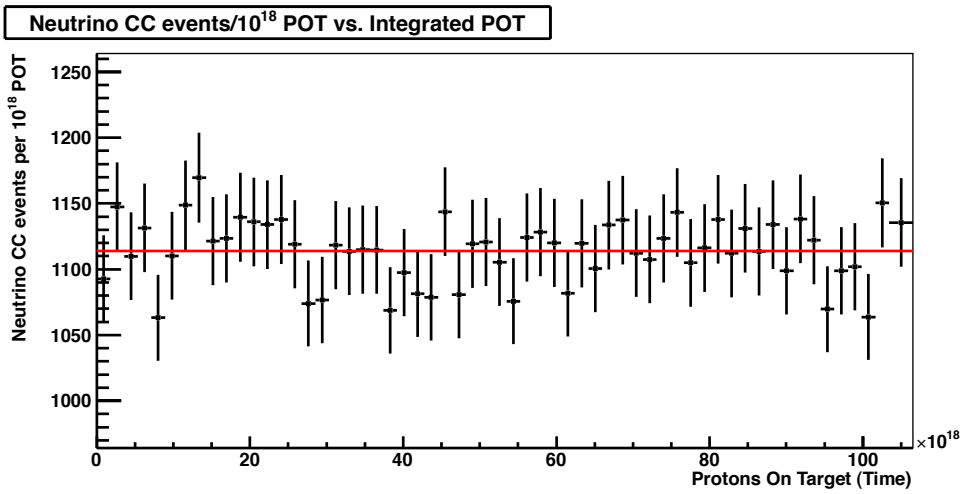

Figure 24: This shows the stability of charged current candidates as a function of time for the MINERνA01 Playlist.

eve

5 Event Reconstruction

The base reconstruction code for the MINERνA experiment was written by the author of this manuscript. The code has changed during the lifetime of the project, but the core ideas remain the same. A brief description of the procedure will be given here; emphasis will be placed on the specific code the author played the largest role in. Most of this work involved software used in the pre-event building stage of reconstruction.

5.1 Cluster Formation

The first step in track reconstruction and pattern recognition is the creation of localized energy deposits, dubbed clusters, inside individual scintillator planes in the various sub-detectors of MINERνA. Clusters will have varying size and total energy deposit depending on the location of in the detector and the object being reconstructed: smaller clusters in the tracker for muon tracks, small high energy clusters for hadron tracks, and larger clusters in the calorimeters for showers or ranging out particles. These clusters are then fed into the pattern recognition, tracking and stray energy collecting (a.k.a. blobbing) routines.

5.1.1 Clustering Algorithm

Prior to the clustering, energy deposits in the detector are grouped into smaller time windows based on the deposit's associated timing information. This separates possible multiple interactions in the detector from the wide, in time, NuMI neutrino beam, see section 3.

Clusters are formed in only one detector plane; the grouping of clusters into objects is done in the subsequent pattern recognitions. The clustering algorithm starts at one end of a scintillator plane and searches for an energy deposit in the triangular strips. The threshold for beginning a cluster is set to 0.5 MeV. Once an energy deposit in a strip is located, a cluster is begun and every strip with an energy above the threshold is added to this cluster. When the algorithm finds a strip with energy below the threshold, the cluster is finalized and the entire process is repeated until the last scintillator strip in the plane is reached.

A coordinate and an error is assigned to each of the created clusters. The current algorithm used is a charged-weighted average position based on every deposit in the cluster:

$$\sum_i^N x_i E_i / \sum_i^N E_i$$

where x_i represents the strip position and E_i represents the strip energy. The error assigned to the cluster position is a default error scale times the factor:

$$\sqrt{\sum_i^N (x_i E_i)^2} / \sum_i^N E_i.$$

The default error scale is 3mm based on monte carlo coordinal residual studies on through going muon tracks.

5.1.2 Cluster Classification

The clusters are scanned in order to classify them for further use. Detector signals are not included into this algorithm if they have too low or too high of a deposited energy signal;

the current low/high thresholds to be considered a trackable cluster are 1.0 and 12.0 MeV. Clusters that are made up of one or two fired detector strips are classified as trackable if the energy making up the cluster is between the above listed threshold. Clusters below this are considered "Low-Activity" and are not used in the pattern recognition; clusters above this threshold are classified as "HeavyIonizing" and are used in non-muon pattern recognitions (see below). Clusters that are created out of three and four detector strips are classified in a slightly different way. The bulk of the energy in the three and four hit clusters is required to be in two adjacent strips. This is to prevent a cluster being formed that will have peaks and valleys in the energy profile (these clusters are investigated and potentially recovered at a later time). Clusters that are comprised of more than five detector strips are classified as "SuperCluster" and are not used in the first pass of the pattern recognition. This is a first pass at trying to sort out trackable energy depositions and shower-like energy depositions[3].

5.2 Pattern Recognition

There are currently two main pattern recognitions (PatRec) used in the MINERνA experiment: one to find longer tracks and one to search for shorter tracks. Both of these were originally written by the author and although they have been modified over the life time of the experiment, the core functionality and methodology remains the same as when they were originally written. The pattern recognition could be improved to use more sophisticated methods (i.e. neural networks, decision trees, etc.) to recover more energetic, larger multiplicity neutrino events, but this will likely come about at a later date.

The two PatRecs present are: the long tracker which uses three hits that line along a line in each of the detector's three views to build tracks and the short tracker which uses geometrical connection between the detector views to create tracks out of as small as five detector hits. Both of the pattern recognition algorithms start processing hits at the downstream end of the detector. The idea being that tracks are more separated downstream in the detector

[3]Initial reconstruction was built to find muon tracks (i.e. long tracks and small energy deposits). The software is being modified to handle hadrons, but this is a slow task.

rather than upstream near a vertex of an interaction. This procedure could be improved by searching for localized energy depositions prior to the pattern recognition stage; but, again this will likely come about in the future.

5.2.1 Long Track Finding

The long tracker exists in two different modes: the long3D tracker and the long2D tracker (the 2D is more of a subset of the 3D rather than a separate, distinct pattern recognition).

In each of the detector view (X,U and V), clusters are sorted by their Z position in the detector. The algorithm then iterates through the detector Z locations (starting at the rear of the detector), takes clusters in three subsequent planes (i.e. N, N-1, N-2) and least-squares fits them to:

$$W_i = \alpha \times Z_i + \beta$$

where Z_i and W_i represent the cluster Z position and the transverse position measured by the X, U or V plane. If the returned fit χ^2 is below a certain threshold, this group of three clusters is promoted to a track seed. Different track seeds are allowed to share the same cluster. It is important to note that different view track seeds will have a different Z-span: X view track seeds span 142mm, while U and V view track seeds span 189mm (this difference comes into play later on in the reconstruction). There are quite a bit fewer track seeds than there are track clusters. In addition, track seeds provide local fit information instead of just positional information. Track seed formation reduces the total number of reconstruction objects and provides more information.

The next step of the PatRec joins track seeds in each view by matching the their fit parameters. Proceeding downstream to upstream, track seeds that match the fitted α and β to within a certain threshold are joined into an object called a track candidate. If the track seeds do not overlap in their Z positions and still are within a set Z range, the seeds are extrapolated to a Z

position halfway between the seeds and then combined if the extrapolated positions are close enough. After each successful merge the fit parameters are updated with all of the new W_i and Z_i points. Track seeds that are added more recently have a larger weight than those that are added previously when performing the least-squares fit. This is to allow for this intermediate track object to slightly bend to accommodate any multiple scattering along the path.

Now, there are two dimensional track objects in all three of the detector views (in addition to stray non-joined clusters). The next step involves merging these into a three dimensional track object. For combinations of X, U and V track candidates, a temporary track is created and then a 3D track χ^2 is formed from the fit coordinate and the projected coordinate at each track Z location that this track spans:

$$\chi^2 = (W_C - W_P)^2/(\sigma_C^2 + \sigma_P^2) \times L^{-1}$$

where W_i stands for the fitted coordinate (C) and the projected coordinate (P), σ_i stands for the error associated with these quantities and L is the length of the track. The fit coordinate comes out of the Kalman Filter routine (see 5.3, page 68) and the projected coordinate is the simple linear projection to the current Z location from the least-squares fit parameters of the track candidate. If this χ^2 is below a threshold, track is kept. The track is expanded by adding other candidates as long as the χ^2 threshold is not breached. After finishing the iteration over track candidates, each of the promoted tracks is fit with the Kalman Filter.

The shortest track that can be formed from this Long3D PatRec must have at least one candidate from each of the three different views. This means that the formed track must span at least eleven detector planes which corresponds to roughly 20cm. This is a fundamental limitation in the PatRec, but this procedure has roughly 97% efficiency for charged current muons. The distinction between the Long3D and the Long2D track pattern recognition is that the Long2D attempts to join only two of the three view candidates. This lowers the overall length threshold of the formed track to nine detector planes, about 16.5cm.

5.2.2 Short Track Finding

The short PatRec has a different starting point for a track. It requires four subsequent clusters with the pattern: UXVX, XVXU, VXUX, or XUXV. Two X planes are always required and no gaps are allowed in the four hit combination pattern. The short pattern recognition uses the geometric connection between different detector views:

$$X = X, \qquad U = X/2 - Y\sqrt{3}/2, \qquad V = X/2 + Y\sqrt{3}/2$$

adding and subtracting the second and third equations gives the relationship between the planar coordinates:

$$X = U + V, \qquad Y = (V - U)/\sqrt{3}$$

When the four hit combinations are found, the X slope is calculated, and the differences $X_1 - U - V$ and $X_2 - U - V$ are formed. The four hit combination is rejected if the X slope returns a non-physical track or if the coordinate differences lie outside a set range (currently set to the width of three strips). These four hit combinations are iterated through and merged if the X slope difference falls below a certain threshold and have at least one overlapping cluster. Currently, the processed/merged short tracks must have at least five total hits in the track (i.e. at least two four hit combinations have to be joined); this is to reduce the number of spurious tracks found by this PatRec. The tracks are then fed into the Kalman Filter for fitting.

This pattern recognition reduces the length threshold of the found tracks to 9cm (7.5cm) because the basic track element spans 5 (4) planes. This pattern recognition was developed before any cross-talk rejection was implemented. Once this cross talk rejection is functional, the PatRec will likely have better success in the busy vertex regions of the interactions.

5.3 Kalman Filter

To fit tracks, MINERνAuses an implementation of the well known Kalman filter method [23], which is a local least-squares estimator. In the application to track fitting, the Kalman filter will minimize the sum of standardized distance between the position of the energy deposited in a layer of scintillator and the estimate of the track's parameters as it passed through that layer of scintillator.

The clusters used to form the track are the measurements which is fit to the path of a charged particle under the hypothesis of our track model. For each cluster, a track state is created which is the estimate of the track's parameters in a plane of scintillator. The track parameters are chosen to be $\vec{q} = (x, y, \frac{dx}{dz}, \frac{dy}{dz}, \frac{q}{p})$. The z-position of the state is the same as the z-position of the scintillator plane which contains the cluster. States also carry the covariance matrix which relates the errors on track parameter estimates. The pairing of a cluster and state is called a node. For each node, a residual is calculated, which is the standardized distance between the cluster and state. The goal of track fitting is to minimize the sum of nodes' residuals. This minimization is accomplished trough the following steps:

- Seed: Make an initial guess of track parameters at one end of the track
- Predict: Use state $\vec{q}_k$ to predict state $\vec{q}_{k+1}$
- Filter: Update the predicted state $\vec{q}_{k+1}$ based on the measured position of the cluster in that plane
- Smooth: Use filtered state $\vec{q}_{k+1}$ to back-predict state $\vec{q}_k$ and update again the parameters of $\vec{q}_{k+1}$

The main components of the routine are described in more detail below.

5.3.1 Seed State

The seed state is created during 3D track merging out of the two or three 2D track candidates. The x and y positions and slopes of the track seed state are calculated with an appropriate superposition of the track candidates' starting positions and slopes. The momentum of the seed state is estimated from the track length using a fast parameterization of the Bethe-Bloch formula.

5.3.2 Predict

A state is used to predict the position of the subsequent downstream state using the simple equations of a linear track model (recall that the MINERνA detector lacks a magnetic field, so particle propagation is a straight line):

$$\begin{aligned} x_{k+1} &= x_k + (z_{k+1} - z_k) * (\tfrac{dx}{dz})_k \quad (\tfrac{dx}{dz})_{k+1} = (\tfrac{dx}{dz})_k \\ y_{k+1} &= y_k + (z_{k+1} - z_k) * (\tfrac{dy}{dz})_k \quad (\tfrac{dy}{dz})_{k+1} = (\tfrac{dy}{dz})_k \end{aligned}$$

The $\frac{q}{p}$ parameter is predicted using the expected energy loss of a charged particle through the material between the states, which is calculated with the Bethe-Bloch formula. The additional error on $\frac{q}{p}$ is added to the predicted state.

Multiple Scattering Multiple Coulomb scattering will cause a particle to deviate from a straight line path. To account for this effect, noise is added to the covariance matrix of the predicted state. The noise matrix is [24]:

$$\sigma^2(\theta_{proj})T\left(1 + (\frac{dx}{dz})^2 + (\frac{dy}{dz})^2\right) *$$

$$\begin{pmatrix} (\delta z)^2(1+(\frac{dx}{dz})^2) & (\delta z)^2(\frac{dx}{dz})(\frac{dy}{dz}) & D(\delta z)(1+(\frac{dx}{dz})^2) & D(\delta z)(\frac{dx}{dz})(\frac{dy}{dz}) \\ (\delta z)^2(\frac{dx}{dz})(\frac{dy}{dz}) & (\delta z)^2(1+(\frac{dy}{dz})^2) & D(\delta z)(\frac{dx}{dz})(\frac{dy}{dz}) & D(\delta z)(1+(\frac{dy}{dz})^2) \\ D(\delta z)(1+(\frac{dx}{dz})^2) & D(\delta z)(\frac{dx}{dz})(\frac{dy}{dz}) & (1+(\frac{dx}{dz})^2) & (\frac{dx}{dz})(\frac{dy}{dz}) \\ D(\delta z)(\frac{dx}{dz})(\frac{dy}{dz}) & D(\delta z)(1+(\frac{dy}{dz})^2) & (\frac{dx}{dz})(\frac{dy}{dz}) & (1+(\frac{dy}{dz})^2) \end{pmatrix}$$

where all track parameters come from the previous state ($\vec{q}_k$), T is a factor to account for the size of the nucleus and D is - (+) for forward (backward) going tracks. T is 1 for nuclei with $A < 56$ (Iron) and 2 for bigger nuclei. If the state passes through more materials of differing nuclear composition, an path-weighted average for T is used. $\sigma^2(\theta_{proj})$ is the variance on the angular distribution of multiple scattering and is approximated using:

$$\sigma(\theta_{proj}) = \frac{13.6}{p}\sqrt{\frac{L}{L_r}}\left(1 + 0.038\ln\left(\frac{L}{L_r}\right)\right)$$

where the particle is assumed to be of charge 1 and have $\beta = 1$, p is momentum in MeV/c, L is the path length between the states and L_r is the radiation length of the scatterer. A path-weighted average L_r is used for travel through multiple materials.

5.3.3 Filter

The filtering step updates the current state based on all of the previous measurements and accompanying errors.

5.3.4 Smooth

The smoothing step is essentially back-extrapolation including process noise; or, smoothing is an update of previous measurements based on the current measurements.

5.4 Muon Matching to the MINOS

All current analyses with MINERνA data require the existence of a muon matched track. The directly-downstream MINOS detector (see section 4.1) provides event information on a spill by spill basis [4]. A breakdown of the various muon categories can be seen in figure 25. One can see that the MINOS energy matched category is only a small subset of the total muons that could be recovered. However, muons that are not momentum analyzed via curvature by MINOS will not have the correct charge and therefore add more backgrounds.

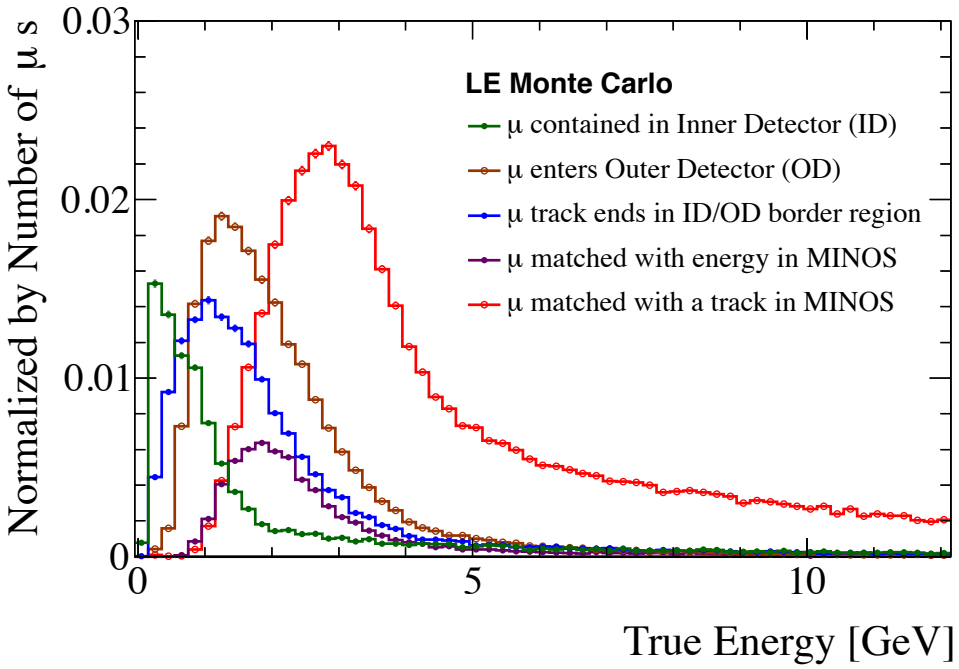

Figure 25: The energy spectrum for various categories of muons is shown. The energy matched muon category is only a small subset of all of the muons that could be used.

All long tracks that have activity in the last 6 modules of the rear hadronic calorimeter are attempted to be matched to tracks reconstructed in the MINOS detector. The search is restricted to the same spill via time matching between the two detectors; any matched track needs to be within 200ns of the other. The MINERνA tracks are projected forward to the Z position of the start of any time-matched MINOS tracks. In addition, the MINOS tracks are

[4]This is very generous of the MINOS Collaboration and the author is very grateful to them.

projected to the downstream Z position. The tracks are matched if the projected position and the actual position fall within an xy-radius of 400mm at **both** of the projected Z positions (the rear of MINERνA and the face of MINOS).

There was significant effort put into aligning the MINERνA and MINOS detectors, both in time and space. Both detectors receive time signals from NuMI beam monitoring software and set local event times to this outside source. Therefore, both detectors are matched in time automatically via the NuMI beam pulse. The alignment in space of the two detectors involved minimizing the track residuals projected between the two detectors. The performance of the track reconstruction and MINOS matching on both rock muons and neutrino event muons can be seen in figures 26 and 27.

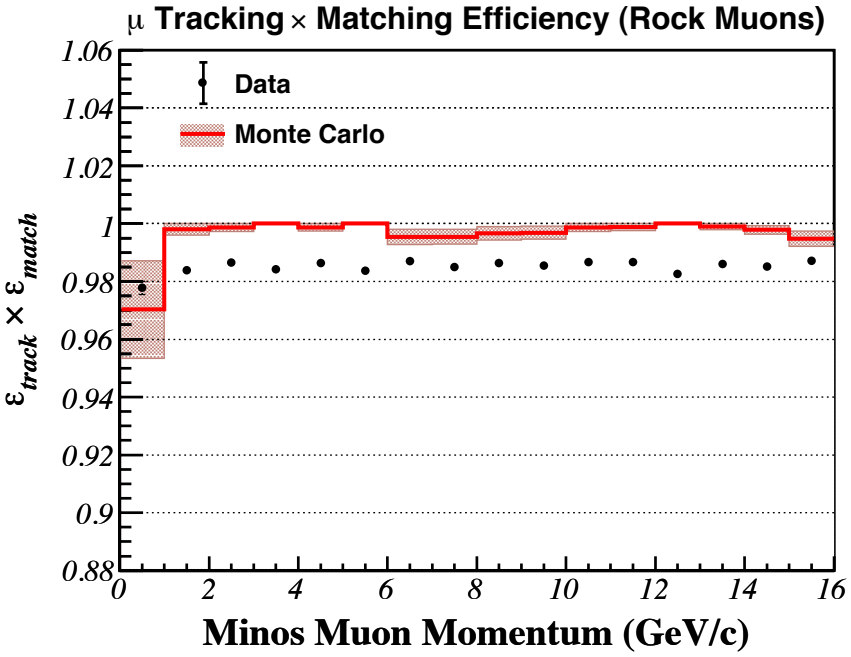

Figure 26: The tracking efficiency times the MINOS matching efficiency is shown as a function of the matched rock muon momentum.

5.5 Building Events

A brief overview of the event building process will be given. This includes selecting an anchor track, doing track cleaning, doing vertex fits and possible short tracking. The current

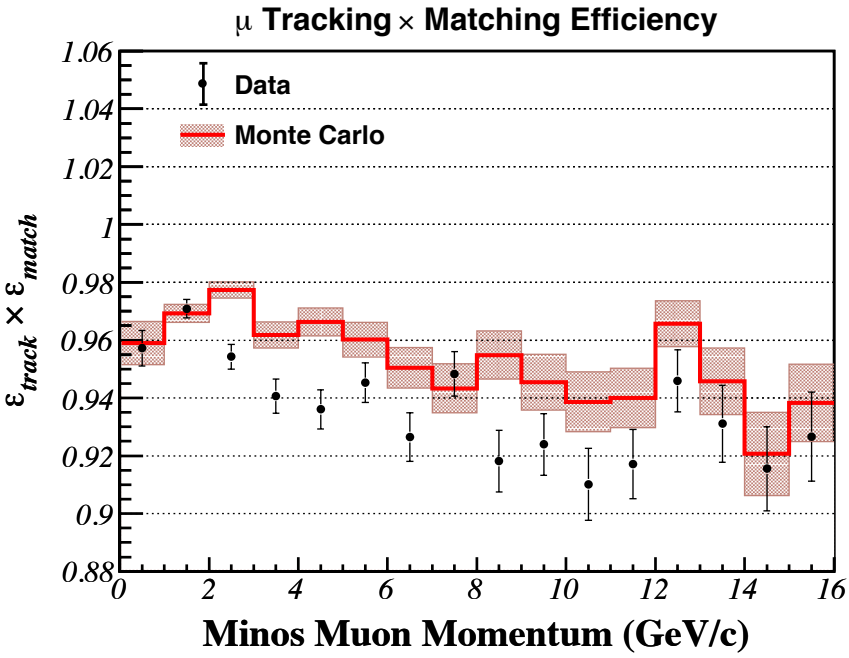

Figure 27: The tracking efficiency times the MINOS matching efficiency is shown as a function of the matched muon momentum of the identified neutrino event.

philosophy in the event building is completely built on charged current events with a MINOS matched tracked, as mentioned above. Future versions of code will most likely involve more sophisticated topological scans, neutral current event building and some kind of network/decision tree/multivariate approach.

The starting point in event building and anchor selection is the track reconstruction steps listed above. After track reconstruction we are left with anywhere from zero to a few tracks, possibly matched to a track in MINOS.

5.5.1 Rock Muons

As mentioned in section 3, there is a constant source of muons in every beam spill. These are not the muons produced along with the original neutrino, but muons that are produced by neutrino interactions by the beam before reaching the detector. The bulk of these muons follow closely along the neutrino path (i.e. along the detector Z-axis), but there is some angular spread depending where the neutrino interacted. Therefore, most of these muons enter

near the front of the detector and exit near the back of the detector.

These rock muons are relatively easy to find and reconstruct due to their long length; rock muons that overlap closely in time with other neutrino (or otherwise) events are more challenging. The subject of handling overlapping interactions in the detector is an active area of study in MINERνA and will not be considered here. Identifying through-going rock muons is fairly easy. Event filters look for muons that have hits that start in the first planes of MINERνA are tagged as potential rock muons and can be extrapolated back to registered hits in the veto wall. Filters also look for long tracks that start near the outside radial edge near the front of the detector. These tracks are tagged as rock muons if they extend all the way to the back of the HCAL in MINERνA or exit the outside radial edge near the rear of the detector. Over 98% of rock muons are positively identified by this simple criteria.

These rock muons serve as a valuable calibration source for the MINERνA detector. These tracks are used to calibrate the energy response of the detector, used to align the MINERνA detector (and inter-align the MINERνA and MINOS detectors), used to study cross-talk produced by the electronics of MINERνA, etc.

5.5.2 Selecting and Cleaning the Anchor Track

Currently, the anchor track is always selected to be the MINOS matched track. The anchor track must originate from a neutrino interaction inside the detector; through going rock muon tracks are not eligible to be the anchor track. There are various filters and data from the veto wall to catch these through going rock muons from masquerading as neutrino interaction muons. The returned fit χ^2 from the Kalman Filter (see section 5.3) must fall below a certain threshold to be considered to be an anchor track, as well.

The anchor track is then cleaned. The track cleaning process began as a method of extrapolating a longer track (in most cases the muon) back through a large cluster or clusters (i.e. shower or vertex activity) to the most upstream point. In these cases, the average energy

from the track is removed from a large energy deposit along the direction of the track and the track is then refitted. If there is a large energy deposit near the vertex of a track, the cleaning will extrapolate the muon back to the farthest upstream point (assuming that the event is charged current and the absence of backward parallel going tracks). The track cleaning procedure also will attempt to break larger clusters on the track to improve position residuals. There are often delta rays or other electromagnetic activity very near the muon tracks that is removed to improve track fitting parameters; this energy is then re-associated to the overall track so as not to degrade energy resolution.

Energy may not be re-associated to the muon track in certain versions of the software. This is evident in figure 21. Track cleaning has been a source of ongoing work due to bugs, error and issues associated with the various versions of the code.

5.5.3 Creating a Primary Vertex

The primary vertex of an event is limited to be created only from an anchor track. This, again, will mature in the future versions of reconstruction code. The primary vertex is chosen to be the most upstream Z position of the anchor track. The vertex position is assigned the values of this upstream track state. The error assigned to the X and Y positions of the vertex is set to the error on the corresponding quantities of the track state. The Z position error is automatically set to 8.5mm, which is exactly half the width of a MINERνA plane.

5.5.4 Anchored Tracks

The next step is to attempt to attach more tracks to the found primary vertex. It is important to note that only the long pattern recognition has been run at this point. All of the other non-MINOS matched tracks found by the long PR are tested to see if the are consistent with the primary vertex. The vertex fitting procedure is described below in section 5.6. Anchored track finding (with the long PR) is performed using the primary vertex to attempt to find other stray tracks that were missed in the first pattern recognition pass.

Secondary anchored tracking is performed using the endpoint of all tracks attached to the primary vertex that also stop inside the inner detector. This tracking pass catches particles that underwent an interaction and have a hard kink in the track. A secondary vertex is created if any tracks are found emerging from any of the endpoints. This secondary vertex is then fit. This procedure is then repeated until all track end points are tried as a possible vertex.

Track cleaning is also performed on these secondary tracks. The track cleaning of secondary (assumed hadrons) tracks is undergoing a reworking at the time of writing this document. These changes will most likely have a large influence on the results of this analysis; but, the software version was frozen for the analysis to be able to proceed[5]. The software does the same cleaning on these secondary track as the primary tracks. But, this procedure splits the wider, heavy-ionizing clusters at the vertices, of which the bulk are from non-muon tracks. This most likely biases the energy reconstruction of these tracks, albeit at a small level. Although, in the track cleaning procedure, clusters are never split at the end of tracks where this could cause possible severe problems for particle identification software.

5.5.5 Short Tracking

The short pattern recognition (short PR) is run after these stages. The pattern recognition is limited to begin in a set region around of a vertex. This prevents any stray energy deposition that lies along a line from being called a track, especially in a higher multiplicity vertex region. A vertex point is required in the current version of the short tracking; the point is used as a starting point of the new track to make sure that the new track is consistent with the vertex. Another variation of so-called anchored short tracking was to first attempt to fit clusters emerging in a cone from the vertex. Both of these yielded similar results. This anchored short tracking is an effective method while event searching is restricted to only charged current events. Neutral current events will require more event building sophistication beyond

[5]There have been changes to the software in the past that have not yield large effects but have hindered the completion of this analysis. And, hence, the decision was made.

this beginning approach and, most likely, the reconstruction software will be modified by the time neutral current analyses begin. There is nothing currently *wrong* with the short PR, but more care has to be taken when trying to fit higher multiplicity events. The author of this manuscript believes that some kind of Hough Transform combined with the existing pattern recognition will be needed for these high multiplicity events and/or broken, displaced tracks.

The MINERνA experiment never fully adopted the short PR into the standard data/monte carlo processing. This was due to the fact that single track analyses were labeled 'high priority' and emphasis was placed on recovering long, MINOS penetrating muon tracks. The author of this analysis first studied neutral current elastic scattering ($\nu p \rightarrow \nu p$) where the signal is a lone proton track in the detector. Because of this (and due to the fact the author wrote the short PR), the author has much experience with the short PR and has vetted this software more than the general collaboration. Analyses that have released results have not used the short PR: single track anti-neutrino charged current quasi-elastic, single track neutrino charged current quasi-elastic and charged current inclusive; analyses that use the short PR: two-track charged current quasi-elastic (plastic and nuclear targets), single pion charged current inclusive, single pion charged current and charged current coherent pion production. Clearly, the code is functional and returns decent results or so many analyses would not be using it; and this analysis would not be able to produce the results that it does.

This step of the processing sometimes causes data loss because the short track fitter and dE/dX code combine to produce unrecoverable failures. There is currently a loss of a few$\times 10^{19}$ POT worth of data in this step, see 6 on page 85. Work is being done by the author on the relevant algorithms to recover these lost protons on target[6].

[6]These failures are tied to the track cleaning and particle identification software work that is being undertaken now.

5.5.6 Outer Detector Event Building

Event building is currently limited to the inner detector. There are no tracking algorithms written for the MINERνA outer detector and energy blobbing (section 5.8) is not done. Inner detector tracks can be extrapolated into the outer detector to look for energy deposits and this is being investigated by a current analysis. But, the outer detector has not been calibrated or aligned so cannot be reliably used in event building before this occurs.

5.6 Vertex Fitting

After two or more tracks are joined, they are fit to a common vertex by the following procedure.

5.6.1 Initial Guess

The vertex fitting procedure begins by making an estimate for the vertex position based on points of closest approach (POCA) using a procedure described in reference [25]. A POCA is calculated for all permutations of pairs of tracks that are attached to the vertex. For each pair of tracks i and j a weight is assigned of:

$$W_{ij} = (d_{min} + DOCA)^n$$

where DOCA is the distance of closest approach between tracks i and j in mm , $d_{min} = 0.01mm$, and $n = -0.5$. The final position of the vertex is taken to be the weighted average of all of the POCAs in the vertex.

5.6.2 Adaptive Vertex Kalman Filter

The adaptive Kalman filter applied to fitting a vertex is described in [25] and [26]. Each track is considered an independent measurement that is used to update the overall vertex position.

The position of the vertex and the track's slopes are used to predict the track's nearest state and compare it to the actual nearest track state. The residual of these two states is used to update the vertex position. A linear track model is used to predict a track state given the current prediction of the vertex position and track momentum. Here, h represents the predicted track parameters of a track coming out of a vertex at position x with momentum q. The equations that predict the track parameters are:

$$\vec{h}(\vec{x},\vec{q}) = \vec{c_0} + A*\vec{x} + B*\vec{q}, \quad A = \frac{d\vec{h}}{d\vec{x}}\,|_{\vec{x}_0,\vec{q}_0}, \quad B = \frac{d\vec{h}}{d\vec{q}}\,|_{\vec{x}_0,\vec{q}_0}, \quad \vec{c_0} = \vec{h}(\vec{x}_0,\vec{q}_0) - A*\vec{x}_0 - B*\vec{q}_0$$

where $\vec{x_0}$ and $\vec{q_0}$ are the position and slope of the state of the track closest to the vertex. The matrix A translates the vertex position into track parameter space, and B translates the track momentum into track parameter space. For a linear track model these equations become:

$$A = \begin{pmatrix} 1 & 0 & -\frac{dx}{dz}\,|_{\vec{x}_0,\vec{q}_0} \\ 0 & 1 & -\frac{dy}{dz}\,|_{\vec{x}_0,\vec{q}_0} \\ 0 & 0 & 0 \\ 0 & 0 & 0 \\ 0 & 0 & 0 \end{pmatrix}, \quad B = \begin{pmatrix} 0 & 0 & 0 \\ 0 & 0 & 0 \\ 1 & 0 & 0 \\ 0 & 1 & 0 \\ 0 & 0 & 1 \end{pmatrix}, \quad \vec{c}_0 = \begin{pmatrix} \frac{dx}{dz}\,|_{\vec{x}_0,\vec{q}_0} * z_0 \\ \frac{dy}{dz}\,|_{\vec{x}_0,\vec{q}_0} * z_0 \\ 0 \\ 0 \\ 0 \end{pmatrix}$$

The Kalman gain of the track is given by the product of the weight and inverse of the covariances of the estimated and measured track state:

$$G = weight * (V_{est.}^{-1} + V_{meas.}^{-1})$$

This represents a measurement of how much confidence can be put into the nearest state on the track. The Kalman gain is used to update the covariance matrix, position of the vertex and momentum of tracks at the vertex, respectively:

$$C = (C_{prev}^{-1} + A^T * G_b * A)^{-1}, \quad \vec{x} = C(C_{prev}^{-1} * \vec{x}_{prev} + A^T * G_b * (\vec{m} - \vec{c}_0)), \quad \vec{q} = W * B^T * G * (\vec{m} - \vec{c}_0 - A * \vec{x})$$

where $\vec{m}$ is the fit parameters of the measured track state, and

$$W = (B^T * G * B)^{-1} \quad G_b = G - G * B * W * B^T * G.$$

The residual and χ^2 of the track state are computed according the following equations:

$$\vec{r} = (\vec{m} - \vec{c}_0 - A * \vec{x} - B * \vec{q}), \quad \chi^2_{kf} = \vec{r}^T * G * \vec{r} + (\vec{x} - \vec{x}_{prev})^T * C_{prev}^{-1} * (\vec{x} - \vec{x}_{prev})$$

and the weight assigned to the track is updated according to:

$$weight_i = \frac{1}{1 + e^{\frac{\chi_i^2 - \chi_{crit}^2}{2.0 * T}}}$$

where χ^2_{crit} is 10.0, T is the annealing temperature, and

$$\chi_i^2 = Similarity(\vec{r}, G) + Similarity(\vec{x} - \vec{x}_{prev}, C_{prev}^{-1}).$$

One iteration of the vertex fitter is completed after all of the tracks are used to update the overall vertex position and the corresponding covariance matrix. The iteration process is stopped if the vertex position moves less than .1 mm or the χ^2/dof improves by less than .05; the vertex is considered *converged* is these conditions are fulfilled. The fit fails if convergence is not reached after 10 such iterations.

5.6.3 Annealing

Annealing is a process used in the vertex fitting that modifies the weighting of a track in successive iterations. This strengthens the compatibility of tracks that come from a similar vertex and down-weights tracks that are not originating from a common point. The annealing temperature is set to an initial value of 25, and is updated after each iteration of the Kalman filter according the formula [27]

$$T = 1.0 + 0.35 * (T_{prev} - 1.0)$$

The overall performance of the vertex fitting procedure in MINERνA is shown in section 4.9, table 6 on page 57.

5.7 Particle Identification

MINERνA has base particle identification algorithms for certain classes of muons and a few types of contained hadrons. A brief description of these algorithms will be given.

5.7.1 Muon Identification

There are several classes of muons that are of interest: muons that stop inside the MINERνA inner detector, muons that exit MINERνA and enter into MINOS, muons that stop in the MINERνA outer detector and muons that exit MINERνA with a trajectory that does not intersect MINOS.

As mentioned above, all analyses being done with MINERνA data use MINOS matched muons. This is the primary method of muon identification. The charge over momentum (q/p) of MINOS matched tracks in the NuMI neutrino mode are required to be less than zero; the q/p of MINOS matched tracks in the NuMI anti-neutrino mode are required to be greater than zero. MINERνA does not currently use MINOS tracks that are momentum

analyzed by range (and are not charge identified). The MINOS tracks that are analyzed by curvature penetrate quite far into the MINOS detector; there is only a very small probability that a charged hadron would be created with enough energy ($\geq$ 10 GeV) in the MINERνA detector with LE NuMI beam and travel this far of a distance into MINOS. As such, all MINOS matched tracks are assumed to be muons.

Muons that exit MINERνA (and do not have a trajectory into the MINOS detector) are lost and are for the most part unrecoverable. There are efforts to identify muons that stop in the inner detector via the michel electrons. Algorithms like this are not at the level of being used in any MINERνA data analyses as of yet. There are efforts to use muons that stop in the outer detector. Inner detector track-outer detector hit matching is possible, but the outer detector does not have any track reconstruction or energy calibration. This makes the energy resolution of theses types of tracks poor. Active work is being done to recover these muons as they greatly increase the number of events that can be reconstructed in MINERνA.

5.7.2 Contained Track Identification

Tracks that are contained inside the MINERνA detector are analyzed and (attempted to be) identified by the energy deposited as they range out. The energy deposited along the track is gathered, the path corrected and the total material budget is computed. The track is then scanned and the deposited energy is compared to a calculated deposited energy given a particular particle hypothesis. A particle identification dE/dX χ^2 is then formed. The χ^2 is a normalized difference between the measured energy loss and the calculated energy loss (assuming a certain particle hypothesis). The dE/dX χ^2 is normalized by the photo-statistical error, the error on the measured energy loss, the error on the calculated energy loss and the path length error. A particle ID χ^2 is formed for every particle hypothesis; currently MINERνA only fits for a proton and pion hypothesis. A particle hypothesis for kaons, electrons and muons could be added but have not been studied sufficiently to be included in standard data/monte carlo processing. There are two different methods for forming the χ^2: one that uses the full information on the track for identification and one that uses only

the end of the track (the so-called Bragg peak). The full information of the track is used in this analysis, but recently the second method has been shown to have better performance on identifying pions in the data. A momentum and energy are created for every one of the particle hypotheses and associated to the reconstructed track.

A particle identification variable is then formed from the dE/dX fit χ^2 for each hypothesis. The particle ID variable, in its current form, starts to lose discriminating power when more than two particle hypotheses are introduced. This is one of the reasons that only a proton and pion particle hypothesis are used. The variable is defined as[7]:

$$pID_i = 1 - \frac{\chi_i^2}{\sum_j \chi_j^2}$$

The particle identification is an active area of development. This development is very much tied into the hadron track cleaning development that was mentioned above. Previous versions of the code had hadron track energy removed in the cleaning stage to potentially aid track reconstruction; this energy was never re-associated for use in energy reconstruction and particle identification. Energy reconstruction for different versions of code and different hypotheses has shown varying performance. This is discussed further in later sections.

5.8 Stray Energy Collection - Blobbing

The next step of the reconstruction process is to collect stray energy that is not used in track reconstruction and do some preliminary identification and collection of this stray energy. The blobbing process does not use any low activity clusters (clusters below 1MeV of energy) or cross-talk candidates (low energy hits from PMT pixels that are adjacent to higher energy

[7]One can see that this is just a more complicated relation between the individual χ_i^2's. This is touched on later in the analysis section

pixels). There are two methods used in blobbing: the filament method and the radial method. The filament style is to collect energy that lies along a line that track reconstruction did not find. The radial method simply collects stray energy inside certain sequentially larger radii. Properties such as allowed blob Z-gap, maximum plane coordinate gap, maximum search radius, etc. need to be provided to these blob algorithms and default parameters exist for these.

There are two main categories of blobs that are created by the current software: isolated and dispersed. Isolated blobs are formed out of more than one view cluster. Dispersed blobs can be made of only one view cluster. Blobs that are created out of more than one view cluster can have a three dimensional detector coordinate associated with them; single view blobs have only a two dimensional spatial location. Depending on the size of the blob (in the transverse and longitudinal direction), more than one detector coordinate could be formed and associated to the blob. The first energy blobbing is done around the primary vertex; the vertex blobbing is always limited to a sphere of 10cm. Blobs are created around secondary vertices as well. The remaining clusters, regardless of location in the detector, are used to create the remaining blobs: isolated blobs if there are close proximity adjacent view clusters, dispersed blobs if energy is limited to a single plane.

6 MINERνA Data Sets

The MINERνA detector came online around 11/2009 and has been taking data in various detector configurations and with varying beam settings up to the end of April 2012. All of the data, less the special run data, was taken when the NuMI beam was in the LE configuration. The beam is currently shut down for maintenance and changing the system over to the medium energy beam configuration. The beam is scheduled to be turned on in low power mode around February 2013 and back to normal operation for data taking in July 2013, at the earliest . See section 3.1.1 on page 30 for an explanation of these beam modes.

6.1 Tracking Prototype

The very first data set that was taken with a version of the MINERνA detector was taken with the MINERνA Tracking Prototype. The Tracking Prototype was nineteen planes of tracker and twenty planes of ECAL. This detector served as an all encompassing test of the systems of the MINERνA detector: electronics, software, reconstruction, etc. This detector saw about three full months of neutrino data as well as cosmic ray data when the detector was first assembled above ground. There were no physics analyses with this detector data, partially because of the small size and lack of event containment. But, the tracking prototype was instrumental in the understanding of the MINERνA detector.

6.2 Partial $\overline{\nu}_\mu$ Detector Data

The detector began taking in November 2009 when only approximately 55% of the detector modules were installed. There are two months of anti-neutrino data recorded in this detector configuration. This data set is referred to as the 'frozen detector' data.

After this, the rest of the detector was installed *while* the anti-neutrino beam was running; this is called the downstream data set. This set runs from January 2010 until the full detector construction was completed in March 2010.

Neither of these data sets will be considered here. The corresponding two track analysis would involve final state tracking of a neutron, which MINERνA is incapable of doing. There is a quasi-elastic one-track analysis done on the 8.96×10^{19} POT of anti-neutrino data. The cross section result as a function of Q^2 can be seen in figure 28 and the systematic error breakdown can be seen in figure 29.

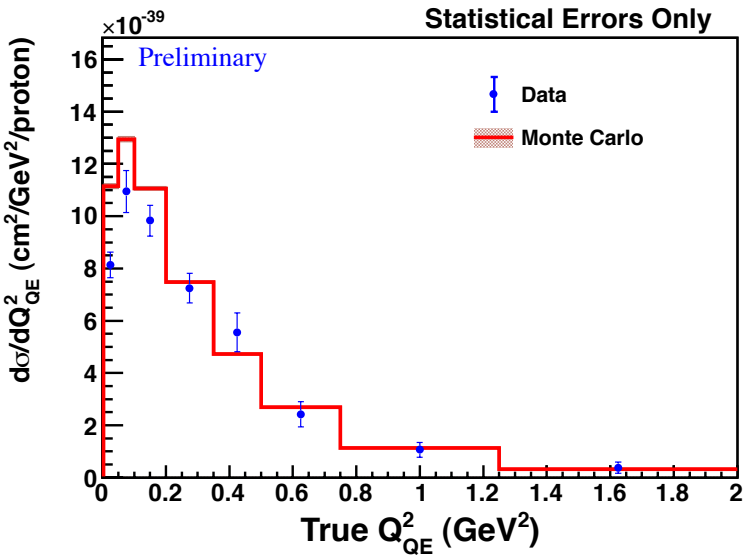

Figure 28: This plot shows the preliminary results from the one-track $\overline{\nu}$ CCQE analysis.

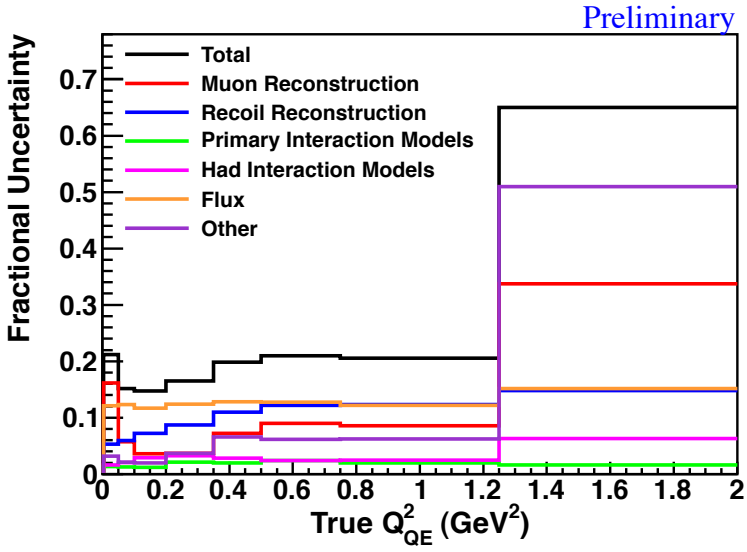

Figure 29: This plot shows the preliminary errors from the one-track $\overline{\nu}$ CCQE analysis.

6.3 Full Detector Data

As mentioned previously, the full MINERνA detector was completed March 2010. At this point, the current in the NuMI focusing horns was switched and the detector began taking data with the beam in low energy (LE) neutrino mode. The detector has a near constant live time with few interruptions while the NuMI beam has been active; there are a few sporadic instances of hour-or-so detector downtimes and regular beam down times during scheduled Fermilab shutdowns when the detector does not take data. While the neutrino beam is live, MINERνA has data taking efficiencies of approximately 97%.

There are six different periods of full detector data consisting of varying length and intensity of neutrino data, anti-neutrino data and 'special run' data. A brief description will be given about the duration and recorded POT of these periods.

6.3.1 Neutrino Data

The full detector took LE neutrino data from March 2010 until the beam shutdown in July 2010. During this running, a total of 1.2×10^{20} POT worth of data was recorded. This data set is from when the detector does **not** have the cryogenic target or the the water target installed, see section 4.3.3 on page 44.

There was another period of neutrino running that took place from between September 2011 until the beam shutdown in April 2012. The cryostat was installed prior to the beginning of this data set. The water target was supposed to be installed at this time as well, but problems prevented this from happening. The water target was installed in November 2011. The total integrated POT for this data set was 3.7×10^{20}. This data set includes 1.9×10^{20} POT with the helium target installed, 5.5×10^{19} POT with the empty cryostat for systematic error studies and 1.96×10^{20} POT with the water target installed. Analysis of this data will take place later after the effects of the full/empty cryostat and water target are understood.

6.3.2 Anti-Neutrino Data

The full detector took LE anti-neutrino data from November 2010 until February 2011 and then again from July 2011 until September 2011. The total data taken in this mode was 1.7×10^{20} POT. The detector does **not** have the cryogenic target or the the water target installed for this data set.

6.3.3 Special Run Data

MINERνA took periods of data where the NuMI neutrino beam was in varying target positions and with various currents in the focusing horn, see section 3.2.1 on page 34. These so-called target scans focus hadrons interactions from the target with different x_f and p_T, which in turn varies the energy distributions of the beam neutrinos. By examining the different spectra of x_f and p_T, the neutrino flux can be better understood and reduce errors associated with the flux. This special run data was taken most often in between horn current polarity switches and represent only a fraction of the total MINERνA data collected.

There were periods of both neutrino and anti-neutrino special run data. For the neutrino special run data, there were three different configurations of the NuMI beam: 7.38×10^{18} POT of data with zero current in the horns, 1.47×10^{19} POT of data in the ν ME configuration and 8.15×10^{18} POT of data in the ν HE configuration. The anti-neutrino special run data consists of 1.92×10^{19} POT of data in the $\overline{\nu}$ ME configuration.

For completeness the detector, configuration and POT totals from November 2009 until April 2012 are listed together in table 7.

6.4 Analysis Data Set

The analysis of this manuscript is based on the first portion of the full detector neutrino LE mode data. This is the period that does not have either the cryostat nor the water target.

detector	configuration	POT
frozen/downstream	$\overline{\nu}$, LE	8.96×10^{19}
full	ν, LE	3.98×10^{20}
full	$\overline{\nu}$, LE	1.7×10^{20}
full, He vessel filled	ν, LE	1.9×10^{20}
full, He vessel empty	ν, LE	5.5×10^{19}
full, water target	ν, LE	1.96×10^{20}
full, special	ν	3.02×10^{19}
full, special	$\overline{\nu}$	1.92×10^{19}

Table 7: This table lists the detector, configuration and POT totals for the various MINERνA data sets between November 2009 and April 2012. All data taken, less the special runs, was in the NuMI beam LE mode.

This data set starts at run 2000 and ends with run 2397 with a total of 3846 subruns. As listed above this corresponds to 1.2×10^{20} POT, but there were issues with certain runs in this data set that forced the removal of about 2.5×10^{19} POT. The official processing for this data periods yields 9.54×10^{19} POT. The analysis requires the running of the shortPR over the data to reconstruct protons that the longPR misses, see section 5.5.5 on page 76. This step reduces the POT a little further to 8.947×10^{19} POT due to failures in the reconstruction. Work is being done to recover this small $\sim 0.6 \times 10^{19}$ POT.

Ideally, the analysis would include the full 3.98×10^{20} POT worth of LE data that MINERνA has collected. This is not possible at the time of this document because the last 2.78×10^{20} POT of data does not currently have calibrations generated and/or applied. Applying this analysis to the data would also have to wait until the data is processed after calibrations have been applied. The completion of this task is set around the end of the calendar year 2012; the data would also have to be studied for variations compared to the first neutrino data set, as well. Both of these factors preclude the opportunity to use the full data set given the timetable for graduation. The two track analysis will be included in any charged current quasi-elastic neutrino results on the full LE data set when released at a later date.

There was a one track neutrino charged current quasi-elastic analysis performed on this data set as well. This analysis would look for a matched muon track and then remove all other

tracks. The stray, non-muon energy was gathered and a cut upon. A final cross section has not yet been calculated, but the event spectra after event selection can be seen in figure 30 and figure 31.

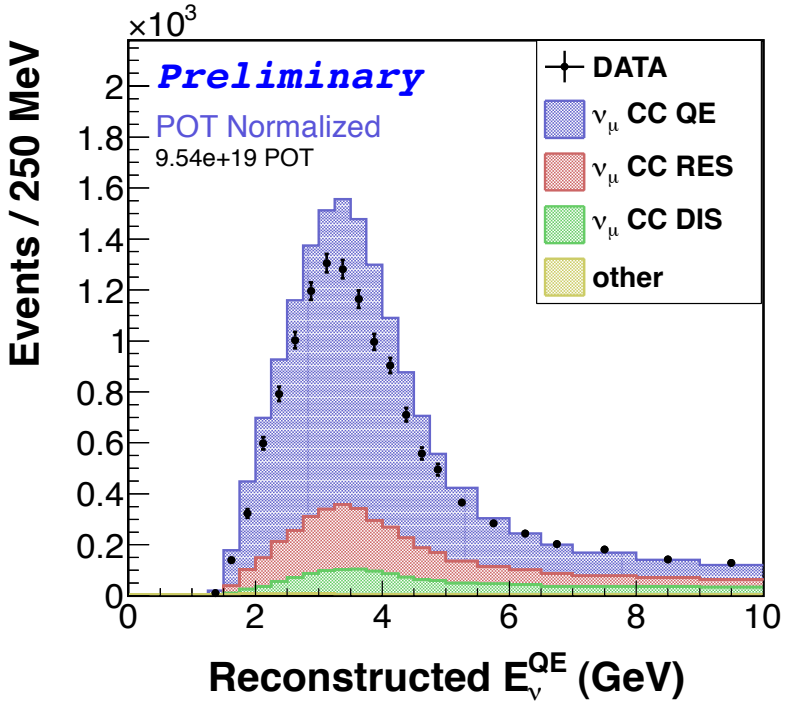

Figure 30: This plot shows the preliminary Q^2 spectrum from the one-track ν CCQE analysis.

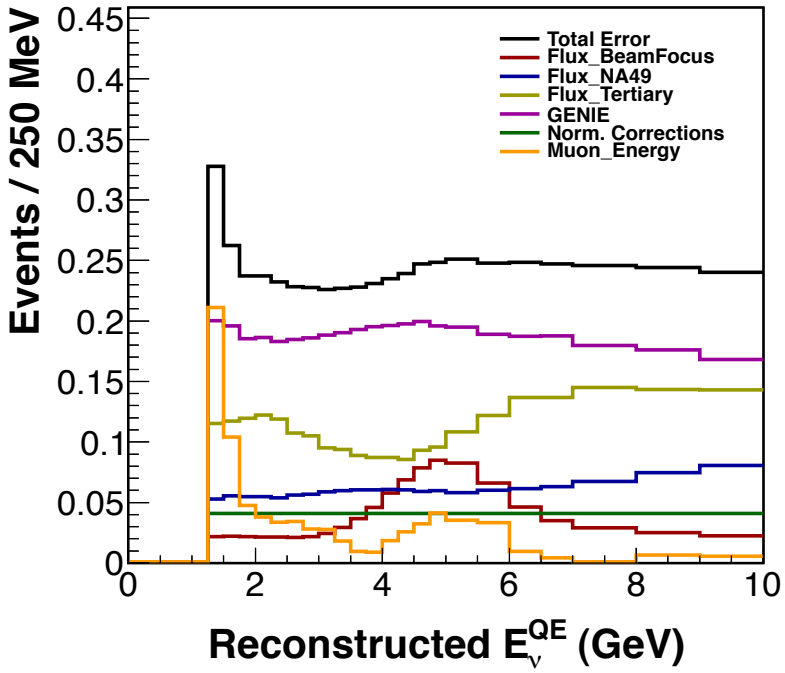

Figure 31: This plot shows the preliminary error on Q^2 from the one-track ν CCQE analysis.

7 CCQE Two Track Analysis

This section will present the main physics analysis that was done during the author's graduate school career.

7.1 Signal Definition

The desired signal is an interaction with negatively charged muon track momentum analyzed by the MINOS detector and a highly-ionizing contained proton track; the CCQE signal can have pions and/or multiple hadrons in the final state, but this first CCQE analysis will focus on the subset of the CCQE signal with a single proton track. Events in which the proton is below tracking threshold of five detector planes are not considered (see 5.2, page 64), nor are events where the proton re-interacts in the detector. The main background to this signal are resonant production or deep inelastic events where only a single proton is detected and all other particles are not detected (i.e. neutrals, absorbed hadrons, particles below detection threshold). In all cases the long, MINOS penetrating track is assumed to be the muon and

the contained track is assumed to be the proton.

The exact definition of 'signal' in the monte carlo is defined as the following:

- the interaction is labeled as charged current quasi-elastic by GENIE
- the interaction does not contain a charmed particle, this is ∼1.3% of the all interactions (and none of the events selected as signal)
- the incoming neutrino energy is less than 22GeV
- the interaction is in a volume defined by a Z extent of {5940mm,8450mm} and an apothem of 900mm; this is slightly larger fiducial volume than listed in section 7.2.1

7.2 Signal Event Selection

The various signal cuts in the analysis will be explained and justified in the following sections. nonvertex non-vertex

7.2.1 Fiducial Volume

The first signal requirement is a vertex originating from a set fiducial volume in the MINERνA detector. The fiducial volume used in this analysis is a Z-detector position located between the first plane of module twenty seven (5990mm) and the last plane of module eighty (8400mm) inside a hexagonal apothem of 850mm. The fiducial volume is four detector planes ($\tilde{1}$00mm) downstream and upstream of the heavy targets and ECAL, respectively. The apothem cut leaves roughly 150mm from the side electromagnetic calorimeter located on the outside edge of the inner detector planes. This selection corresponds to a plastic scintillator volume of $6.03m^3$ or 6.6 tons. This cut will be referred to as: FV.

7.2.2 Muon Identification

The long track in this analysis channel needs to extend into the MINOS detector far enough to be fully reconstructed - shorter tracks that either range out in the upstream region of

MINOS or in the MINOS magnetic coil are not included in this analysis. This requirement puts a lower threshold on the momentum of the muons in the signal selection corresponding to the total energy loss in MINERνA and the front of MINOS. This lower energy limit is around 1.5-2 GeV/c. The track also has to have a charge over momentum (q/p) value of less than zero corresponding to successful momentum identification in the MINOS magnetic field; the cut is to remove the (positive) muons from the wrong neutrino sign background of the NuMI beam. The contamination of anti-neutrinos in the neutrino beam is approximately 5%; the contamination of neutrinos in the anti-neutrino beam is around 20%, see section 3. Using this muon selection limits the reach with the MINERνA detector, but this makes sure that the correct helicity is selected. The momentum resolution of tracks reconstructed in MINOS via range is approximately 4% (momentum resolution is 11% if tracks are reconstructed via range). This cut will be referred to as: CC.

Again, non-MINOS matched muons were not considered in this analysis, see 5.4 on page 71 and will be considered in future versions of this analysis. Also, this analysis is strictly focused on the lower energy region of the neutrino beam; muons that are reconstructed with an energy higher than 20 GeV are rejected.

7.2.3 Two Track Vertex

Two tracks in the given detector time slice need to be reconstructed to the same vertex to be selected for this analysis. This is handled different for the different pattern recognitions used in reconstruction. Two tracks that are created with the long pattern recognition need to have a point of closest approach of less than 250mm (more often that not, this distance is much smaller). A track reconstructed via the 'short' reconstruction needs to have a upstream position be within a three-dimensional distance of 100mm from the upstream position of a long track to be considered vertexed to the longer track. A short track, short track combination is not allowed as per the CC cut. The current version of this cut allows for extra tracks in a time slice that are not attached to the primary vertex; these tracks could be part of the signal or part of the background. This cut will be referred to as: twoVtx.

The total number of tracks for data ands monte carlo for the candidate events are shown in figure 32. Only 2.2% of the events have greater than two tracks in the time slice. A few of the events with more than two tracks were scanned and it was found most of these were from rock muon contamination and from, seemingly, displaced unattached tracks.

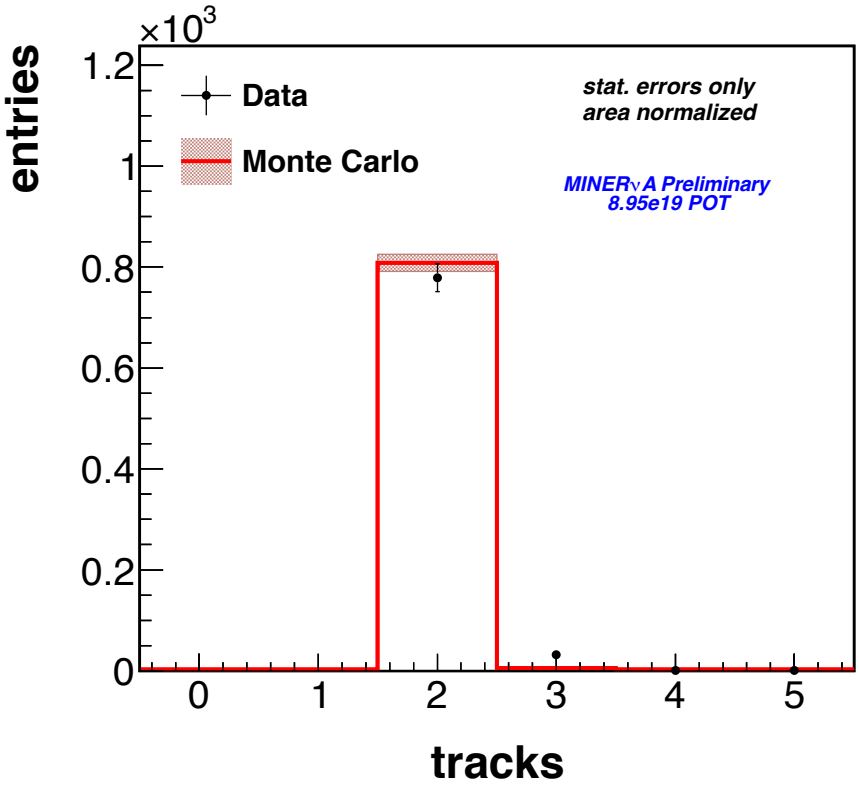

Figure 32: The data / monte carlo comparison of the number of tracks found in candidate two-track charged current quasi-elastic events. Only 2.2% of total selected events have more than two tracks.

7.2.4 Contained Track

The next requirement made in the event selection is that the non-MINOS matched, vertexed track is contained within the bulk of the detector. The containment bounds are slightly larger than the fiducial volume used in this analysis: the second track is allowed to extend out to an apothem of of $950mm$ and downstream to $Z = 8600mm$. The extended Z range allows the track to enter into the downstream, higher mass ECAL; event yields are increased by

approximately 18% by allowing the contained track to transverse into the ECAL. There is no cut on any type of identity associated with the track at this point. The track needs to be contained inside the detector volume in order to identify the track via the energy deposition per plane, especially at the end of the track. There is some systematic error associated with this cut due to the reconstruction software not finding the true end of the track. This will be discussed later. This cut will be referred to as: conTrk.

7.2.5 Extra Energy Cut

There is a cut placed on the extra energy in the time slice not associated with higher level reconstructed objects, i.e. the muon and proton tracks. This cut serves to veto events with a large shower and/or when there is substantial non-tracked activity in the event slice. The collaboration has adopted a procedure that labels all energy with 10cm of the primary vertex as *vertex energy* and does not cut on this quantity, see section 5.5.3 on 75 (an exception is for the coherent π analysis where the signature is no vertex energy). The remaining energy is called *non-vertex* energy. A timing cut is placed on this non-vertex energy distribution; only energy from $\pm$ 25ns from the muon track time is accepted. Also, the energy from the hadronic calorimeter is removed from the sum. The phototubes in the HCAL have more XT than the rest of the detector. This timing cut and removal of HCAL in the extra energy distributions was studied extensively and is used by all current MINERνA analyses. This energy quantity is then cut upon. This cut will be referred to as: EE.

The total number of blobs found in an event differ between data and monte carlo. This is because of inaccuracies in the model of cross talk in the detector and difference in the blobs created in the vertex region of the event (i.e. dispersed and vertex blobs). One can see from figure 33 and figure 34 that the overall non-vertex blob energy and the number of isolated blobs in signal events in data and monte carlo. There is agreement between the data and monte carlo at the level of 20%.

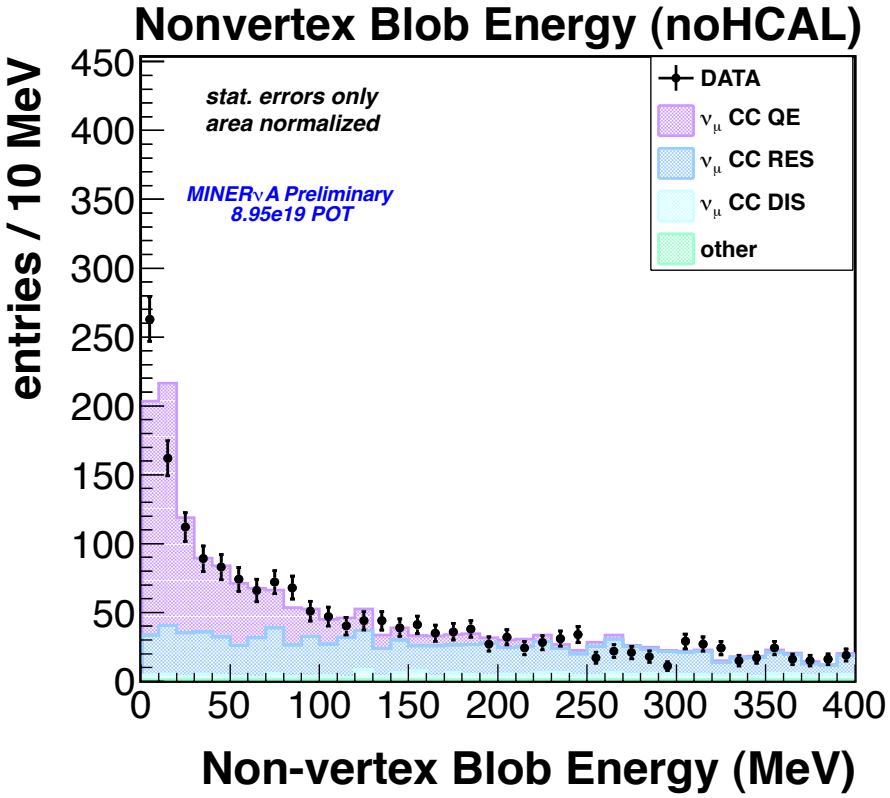

Figure 33: This shows the distribution of the non-tracked blob energy that is outside a sphere of radius 10cm around the identified two-track vertex.

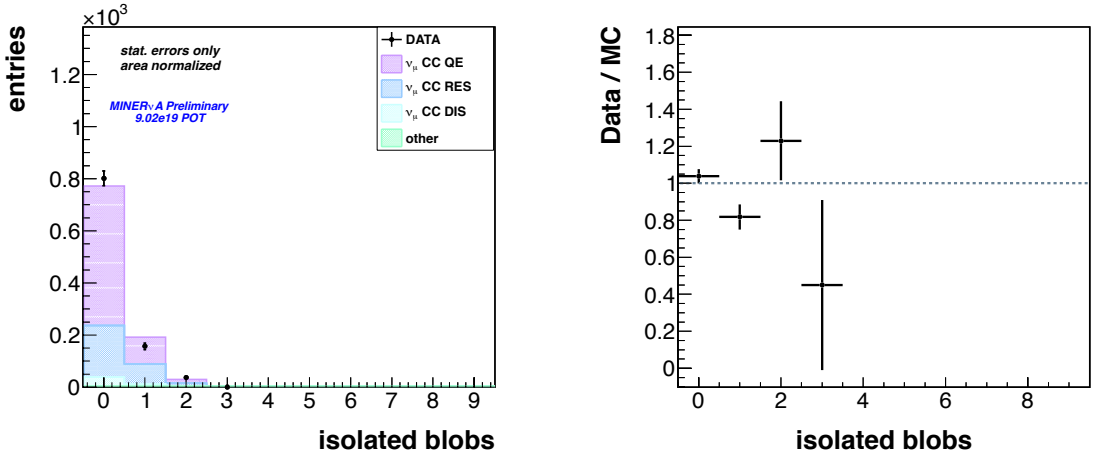

Figure 34: Left: This shows the number of isolated blobs found in both data and monte carlo for events that pass the signal selection. Right: The data/MC ratio of the number of isolated blobs. Data and monte carlo agree fairly well (∼20% level).

7.2.6 Proton Identification

There is a particle identification (PID) cut placed on the vertexed, contained track to remove the background of charged current single $\pi^{\pm}$ events. This signature could be from a resonant or DIS pion production event where the proton is below threshold or absorbed before leaving trackable activity. There were two PID cuts that could be applied: a threshold cut on the proton PID and a requirement that the proton PID was more favorable that the pion PID, see section 5.7, page 81 for further details of the PID process. This cut will be referred to as: prID.

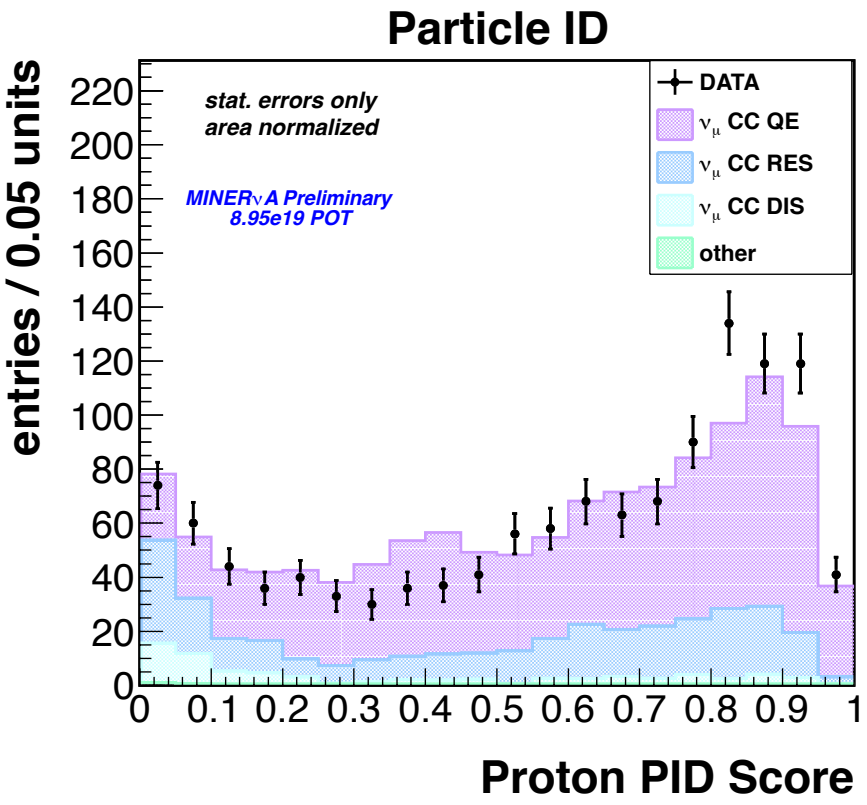

Figure 35: This plot shows the dE/dX proton particle identification parameter.

There was also a cut placed on the particle identification dE/dX χ^2, see section 5.7.2. A very large χ^2 represents a poor dE/dX fit. Figure 36 shows that the bulk of the larger χ^2 bins are populated with background. This cut will be referred to as prχ^2.

The particle identification cut is somewhat problematic because a systematic error has yet to be assigned to PID. A systematic error is not 'readily formable' for the proton particle ID

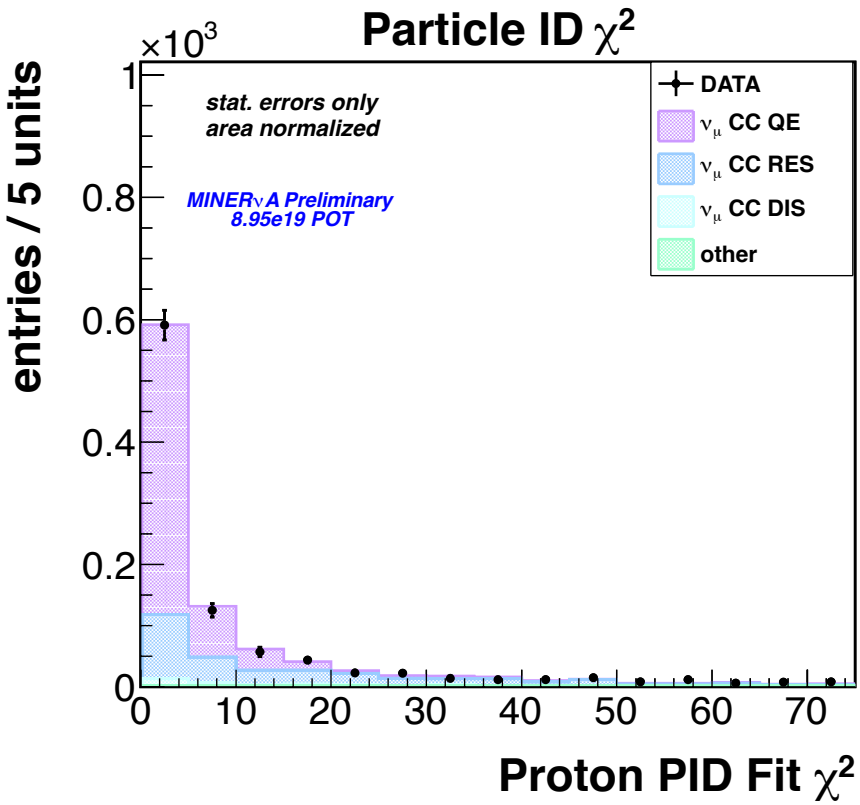

Figure 36: This shows the particle identification fit χ^2.

score. The reconstruction and particle identification code is going through a major reworking at the time of this analysis. New features are being included in the PID, such as including photo-statistical error, as well as including energy on tracks that was previously removed by older versions of the track cleaning procedure. As such, currently forming such an error for the PID process would be using incomplete information and most likely be incorrect at the current time.

7.2.7 CCQE Enhancement - ΔKE cut

In order to enhance the quasi elastic fraction of the selected data, an energy matching cut is placed on the candidate events. As mentioned in previously, one can reconstruct the kinematics of the CCQE event either using only the muon or only the proton. The quantity ΔKE is formed to serve as a normalized energy matching term between the kinematic variables of the muon and proton. It is defined as:

$$\Delta KE \equiv \frac{(E_{\nu}^{CCQE} - E_{\mu} - E_b) - KE_p}{KE_p}$$

Here, E_b is a binding energy set to 30 MeV and,

$$E_{\nu}^{CCQE} = \frac{m_n^2 - (m_p - E_b)^2 - m_{\mu}^2 + 2(m_p - E_b)E_{\mu}}{2(m_p - E_b - E_{\mu} + p_{\mu}\cos\theta_{\mu})}$$

The ΔKE is a pseudo-model independent way to separate signal and background. It matches the visible detector energy of the proton to the expected visible energy proton formed from the observed muon and energy of the neutrino (inferred from the muon). There is a model assumed in the formulation of the quantity E_{μ}^{CCQE} (with the presence of the binding energy); but, ΔKE uses only the kinetic energy of the proton which is less likely to be influenced, in data, via nuclear effects or be biased, in the MC, by the specific nuclear model that is used. Previous experiments have used the angle of the proton in trying to enhance the CCQE

fraction in their data, but this biases the selection because it folds in the nuclear model by using the angle predicted by the specific generator and/or final state interaction model used. This cut will be referred to as: ΔKE, and the distribution can be seen in figure 37.

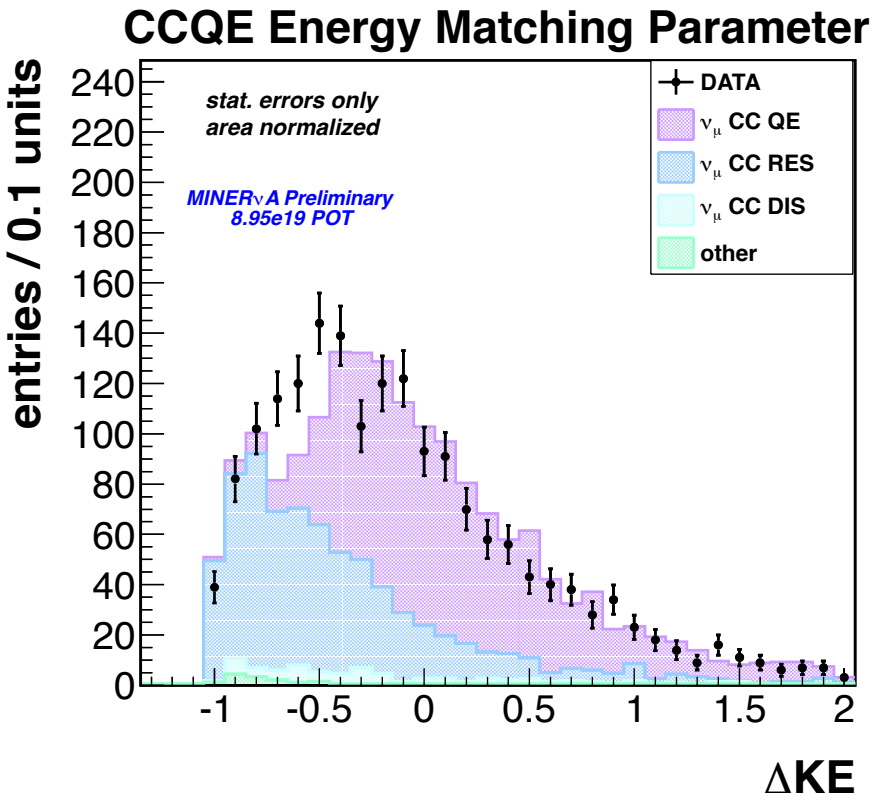

Figure 37: The figure shows the distribution of the cut parameter ΔKE that matches the visible energy of the proton to what is expected from muon information. There is clear signal/background separation at small negative and positive values of ΔKE.

For clarity, a non-stacked version of the ΔKE parameter showing only monte carlo signal and background can be seen in figure 38.

The ΔKE cut clearly enhances signal over background. But much study went into understanding the effects of the cut on the spectra of the signal variables (i.e. p_μ, θ_μ, ..., p_p, θ_p, ...). The ΔKE cut placement had the potential to cause a bias in the event selection. This is discussed further in the Cut Placement section below.

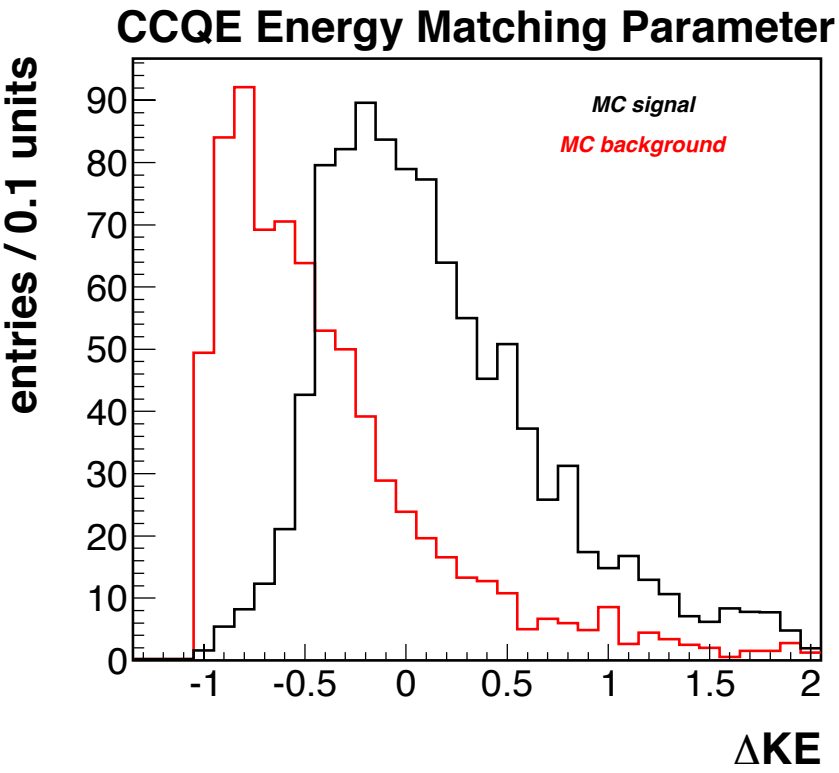

Figure 38: This shows the MC signal and MC background in a non-stacked manner. The ΔKE^{sig} is centered around zero with non-gaussian shape that is related to the nuclear models used in the simulation. The entries populating the -1 bin are usually events with errors in the hadron energy reconstruction.

For reference, the abbreviations for the cuts used in the acceptance and efficiency studies are listed in table 8.

Cut	fiducial volume	charged current	two-track vertex	contained track
Abbreviation	FV	CC	twoVtx	conTrk
Cut	extra energy in slice	reco proton	energy matching	
Abbreviation	EE	prID/prχ^2	ΔKE	

Table 8: The abbreviations used for the signal selection cuts for the CCQE two-track analysis; these are also defined in the main text.

7.3 Signal Acceptance, Efficiency and Purity

There is ambiguity when discussing signal acceptance and efficiency. Both are important when attempting to extract a cross-section measurement from data. Here acceptance effects will be defined as: fiducial volume, muon (MINOS) reconstruction, and MINERνA reconstruction; signal efficiency will involve all other cuts described above.

7.3.1 Acceptance

There were five criteria for passing the acceptance for this analysis:

- The event must be a *true* ν_μ charged current quasi-elastic interaction as defined by GENIE.

- The fiducial volume requirement shapes the acceptance of signals. As mentioned before the fiducial volume for this analysis is module 27 through module 80, inclusive, contained within a 850mm hexagonal apothem. The acceptance fiducial volume extends 50mm further in all directions: a upstream Z cut of 5940mm, a downstream Z cut of 8450mm and an apothem cut of 900mm.

- The current MINERνA software requires that any reconstructed muons are matched to track reconstructed in MINOS. This shapes the distribution of variables used in the analysis, particularly the p_μ and Q^2 distributions, because the higher angle muons will not be momentum analyzed by the MINOS detector. The muon must also be reconstructed via curvature and have the same $q/p < 0$ cut applied to the analysis signal.

- The acceptance signal must also pass a requirement on the reconstructed muon energy. The analysis is currently focused only on events that are inside the focusing peak of the NuMI spectrum and not on very high energy muons. The reconstructed muon energy must be below 22 GeV. This is 2 GeV higher than the cut that defines the analysis sample.

- There was one extra cut that defined the acceptance. This was the absence of a charm particle in the final state. There was a problem with the decay of charmed particles in the current version of the monte carlo that prevented these types of events from being reconstructed correctly[8]. At some point in the future, all of the monte carlo generated for MINERνA will be re-run and this restriction will be removed.

7.3.2 Efficiency and Purity

The above cuts define the denominator for the efficiency. The numerator is defined from events passing all of the above listed cuts: FV, CC, twoVtx, conTrk, EE, prID/prχ^2 and ΔKE (see table 8); note that this FV and CC cuts have the slightly smaller fiducial volume and slightly lower muon energy threshold than the acceptance cuts listed in section 7.3.1. The extra restriction of no charm quark in the final state is also put on the events that appear in the numerator of the efficiency.

[8]The particles did not decay properly and 1GeV of energy would be deposited at the charm creation point.

The purity calculation uses the efficiency numerator as its denominator. The numerator of purity consists of all events that pass the event selection cuts and are *true* ν_μ charged current quasi-elastic interactions, as defined by GENIE.

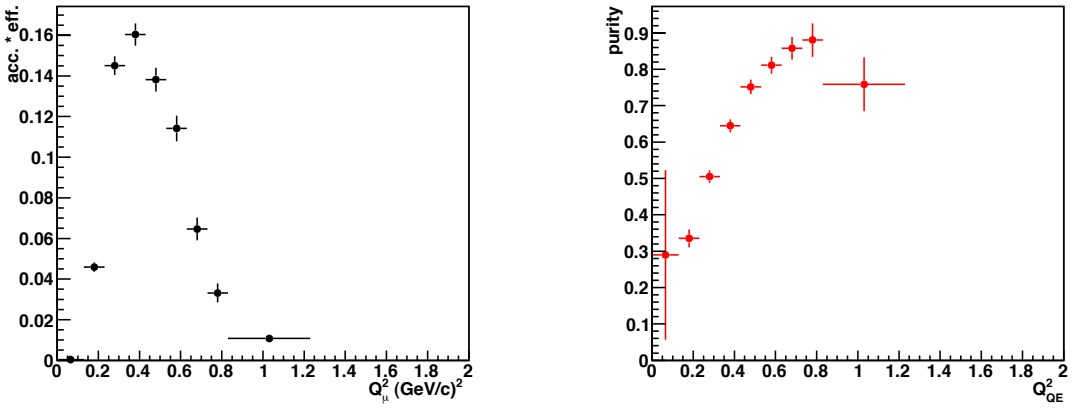

Figure 39: Left: This shows the signal selection efficiency as a function of Q^2. The first two bins have a very low efficiency, but they correspond to a proton that is below the tracking threshold of the MINERνA detector. Right: This panel shows the purity of the event selection. The purity rises quite quickly as Q^2 increases. The efficiency is low, but the sample that is selected is very pure.

7.3.3 Cut Placement

The cut values were studied in a 'N-1' pattern: all of the signal cuts are applied, one of the signal cuts is removed and its spectrum plotted (figures 33, 36, 35 and 37 were all created in this manner). The final cut values were set to maximize or the signal efficiency times the signal purity. Here, signal efficiency is defined by the number of events selected by the cut divided by the total number of signal events present in the distribution; the purity is defined as the number of signal events selected by the cut divided by the number of signal plus background events selected by the cut.

Non-vertex Energy:

The signal to background ratio as a function of the non-vertex blob energy cut value is shown in figure 40 on the left and the cut efficiency, purity and the product of the two is shown on the right. The cut efficiency $\times$ the cut purity shows a maximum around a cut value of

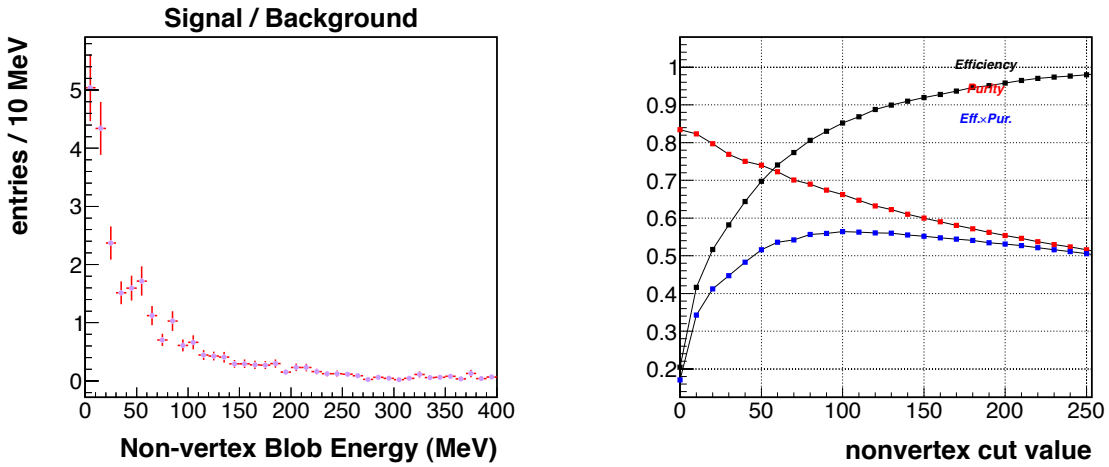

Figure 40: Left: This shows the signal to background ratio as a function of the non-vertex energy variable. Right: This plot shows the efficiency, purity and their product as a function of the non-vertex energy variable.

70-100MeV. The non-vertex energy cut was set at 65MeV. At the higher values of the cut, the signal to background ratio is less than one so a higher cut is allowing more background to pass the selection. A variable, Q^2 dependent cut was investigated but ultimately not implemented, see figure 41. This type of cut did not drastically improve the results of the analysis. This cut will most likely be modified in future two-track CCQE analyses as the reconstruction capabilities of the MINERνA experiment become more sophisticated.

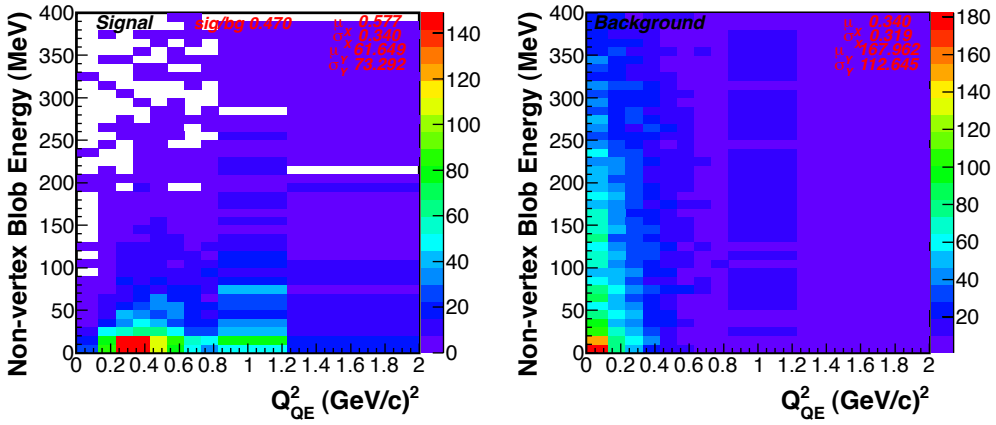

Figure 41: This plot shows the non-vertex energy versus Q^2 for events that pass cuts: FV, CC, twoVtx, contTrk and prID/prχ^2. The GENIE defined signal is shown on the left and the background is shown on the right. The bulk of the background reconstructs to a non-physical Q^2 (i.e. below the proton tracking threshold).

Energy Fit χ^2:

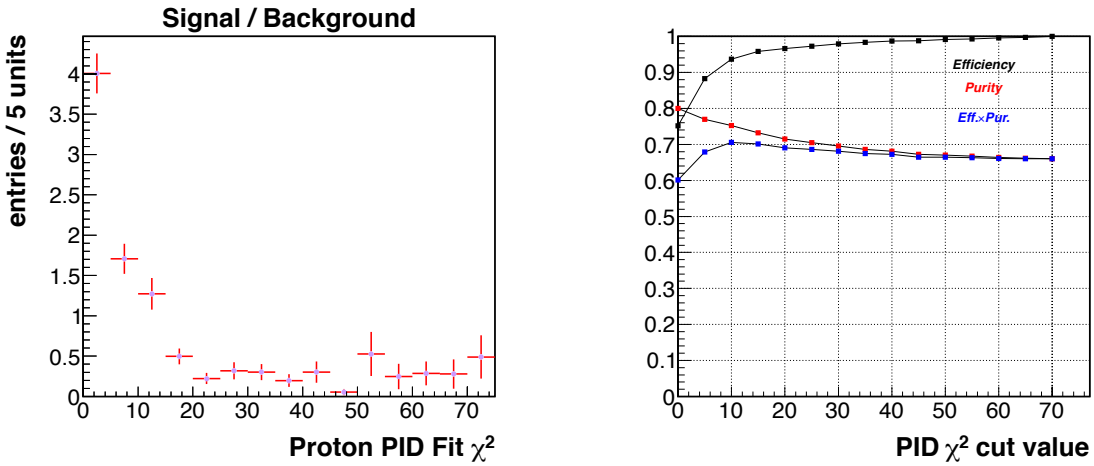

Figure 42: Left: This shows the signal to background ratio as a function of the particle ID χ^2 variable. Right: This plot shows the efficiency, purity and their product as a function of the particle ID χ^2 variable.

The particle identification dE/dX Fit χ^2 distributions are shown in figure 42: the left panel shows the data to background ratio as a function of the dE/dX fit χ^2 and the right panel shows the efficiency and purity as a function of this variable. One can see from the plot, that the efficiency $\times$ purity of the cut only slightly varies from 70% at a cut value of $\chi^2_{dE/dX}$=10 to only around 65% at a cut value of $\chi^2_{dE/dX}$=70. Also, the signal to background ratio reaches a constant value after a $\chi^2_{dE/dX}$ of $\sim$20. The final cut was place at $\chi^2_{dE/dX}$=20. Over twice as much background as signal is included in the analysis for each bin added past the $\chi^2_{dE/dX}$=20 cut value. In addition, the higher values of the $\chi^2_{dE/dX}$ indicate a poorer fit, so all further events added a higher χ^2 value are of increasingly worse quality.

Particle ID:

The particle identification variable is just a more complicated expression involving the individual dE/dX fit χ^2 particle hypotheses; recall from section 5.7.2:

$$pID_i = 1 - \frac{\chi_i^2}{\sum_j \chi_j^2}$$

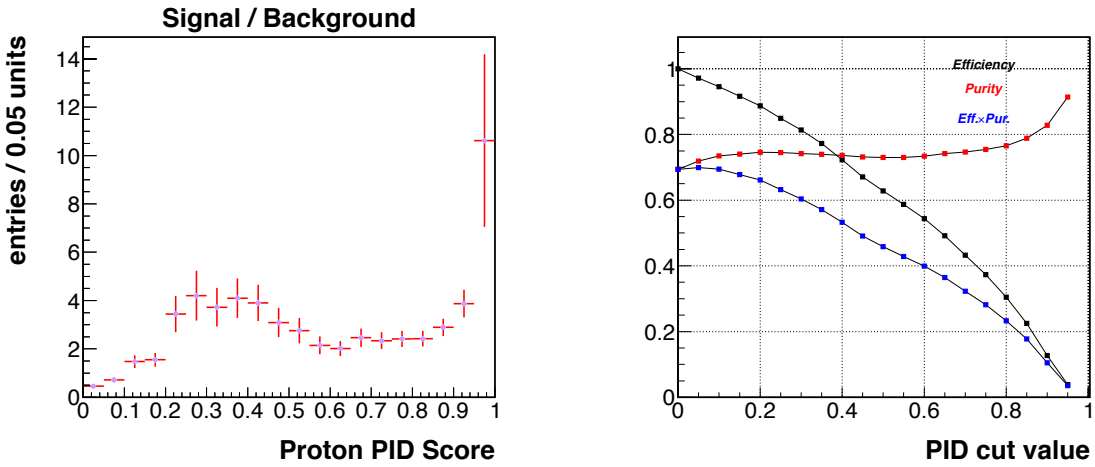

Figure 43: Left: This shows the signal to background ratio as a function of the proton particle ID variable. Right: This plot shows the efficiency, purity and their product as a function of the proton particle ID variable.

where in this case, $i = \{proton, pion\}$. It is relatively easy to see that with only two particle hypotheses that any comparison between the two particle scores is a direct comparison between the $\chi^2_{dE/dX}$:

$$\begin{aligned} 1 - \frac{\chi^2_{pr}}{\chi^2_{pr}+\chi^2_{pi}} &\geq 1 - \frac{\chi^2_{pi}}{\chi^2_{pr}+\chi^2_{pi}} \\ \frac{\chi^2_{pi}}{\chi^2_{pr}+\chi^2_{pi}} &\geq \frac{\chi^2_{pr}}{\chi^2_{pr}+\chi^2_{pi}} \\ \chi^2_{pi} &\geq \chi^2_{pr} \end{aligned}$$

Hence, a straight forward cut to make on the particle ID value is to require that the $prID \geq piID$, which translates into a lower fit $\chi^2_{dE/dX}$ for a proton particle than a pion particle. The other cut that could be placed on the particle ID would be a threshold cut. It is more difficult to justify this cut because the data and monte carlo do not show a high level of agreement, see figure 35 on page 97; the overall trend of the shapes of the data and MC curve do show similarities. The efficiency $\times$ purity for this cut shows a steadily declining value across the entire range of PID cut values. The data to background ratio shows values above unity at cut values as low as protonID= 0.1. The PID cut was placed in the vicinity of a local minimum of the 'N-1' plot (figure 35) of 0.27 units.

The MINERνA test beam program will help in the future analysis involving particle identification. The analysis of the test beam data was not at a mature enough level at the time of this document to be able to further aid in the PID related cuts. Preliminary analysis shows that the proton ID distribution of actual protons is sharply peaked at one and falls off quickly as prID goes to zero. The above cut is further justified if one pictures the **data** prID distribution as the sum of two falling distributions, one at prID=1 (signal) and the other at prID=0 (background).

ΔKE:

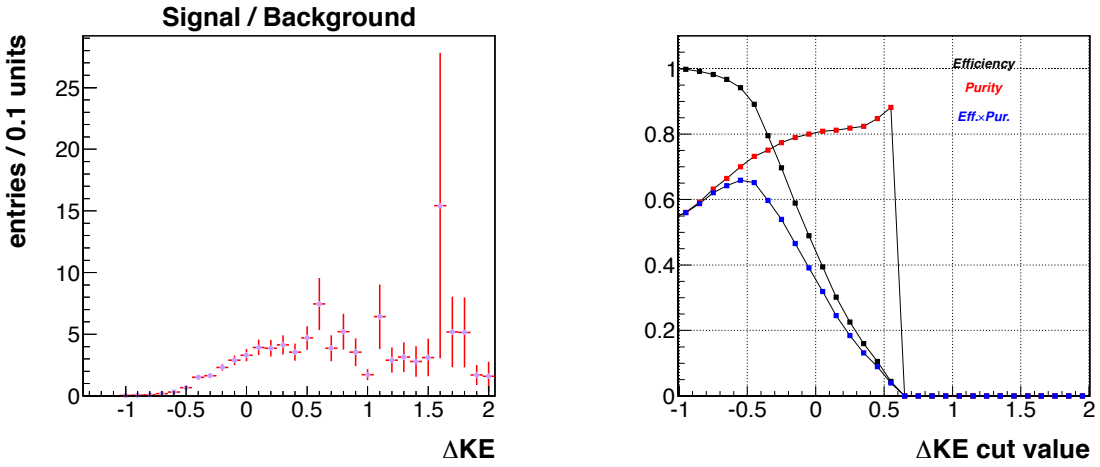

Figure 44: Left: This shows the signal to background ratio as a function of the ΔKE variable. Right: This plot shows the efficiency, purity and their product as a function of the ΔKE variable.

The ΔKE variable is sensitive to both nuclear effects and final state interactions. The ΔKE will **not** be biased by these effects/interactions that change the direction of the emitted proton, but only those that change the overall energy of the proton. Errors in the proton reconstruction also effect this variable. Due to this, the ΔKE variable was given extra scrutiny.

The plots shown in figure 44 indicate that signal efficiency $\times$ purity has a maximum at around -0.5 units. This is also approximately the value where the signal to background ratio rises above unity. In the figure 44 for both the efficiency and the purity, the ΔKE variable is summed up to the value of 0.4 in each entry.

Figures 45 and 46 show the non-vertex energy distributions vs. Q^2 for two different ΔKE

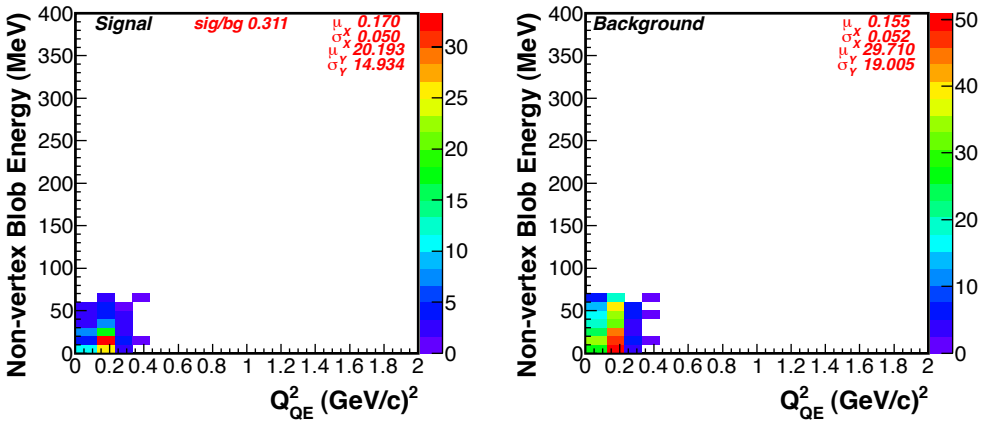

Figure 45: This panel shows the non-vertex energy vs. Q^2 for $\Delta KE \in \{-0.75, -0.5\}$. The bulk of both the signal (left) and background (right) appear in the non-physical Q^2 bin. The signal to background ratio for this ΔKE bin around 0.3 indicating that this bin is background dominant.

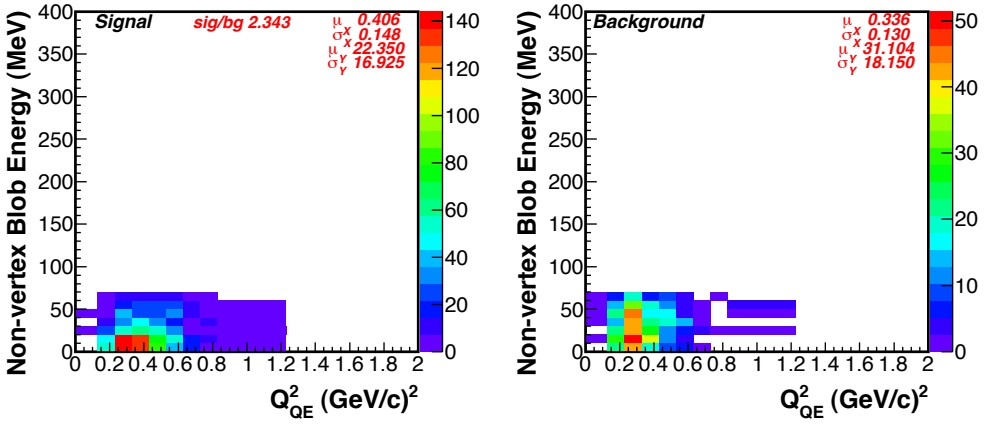

Figure 46: This panel shows the non-vertex energy vs. Q^2 for $\Delta KE \in \{-0.5, 0.4\}$. This is the analyzed ΔKE region. The bulk of the background reconstructs to low Q^2. The signal to background ratio for this ΔKE bin around 2.3 indicating that this is a signal dominant bin.

regions: $\{-0.75, -0.5\}$ and $\{-0.5, 0.4\}$. In the lower region, the bulk of the entries in both the signal and the background reconstruct in Q^2 to the un-physical bin (i.e. below proton tracking threshold). The higher of the two bins has the bulk of the entries reconstructing with a $Q^2 \geq 0.23$ - this Q^2 value has special significance. The tracking threshold, as mentioned before, is currently 5 detector planes or approximately 11cm. A proton with kinetic energy 125 MeV will travel about 11cm in MINERνA when traveling at normal incidence to the detector. A proton kinetic energy of 125 MeV corresponds to a Q^2 of 0.23 $(GeV/c)^2$ using the relation $Q^2 = 2M_pT_p$. Most of the signal protons are produced at higher angles which means that they will have a higher Q^2 value. This fact will be used later to justify the zeroing of the first two bins in the Q^2 distribution in the final result.

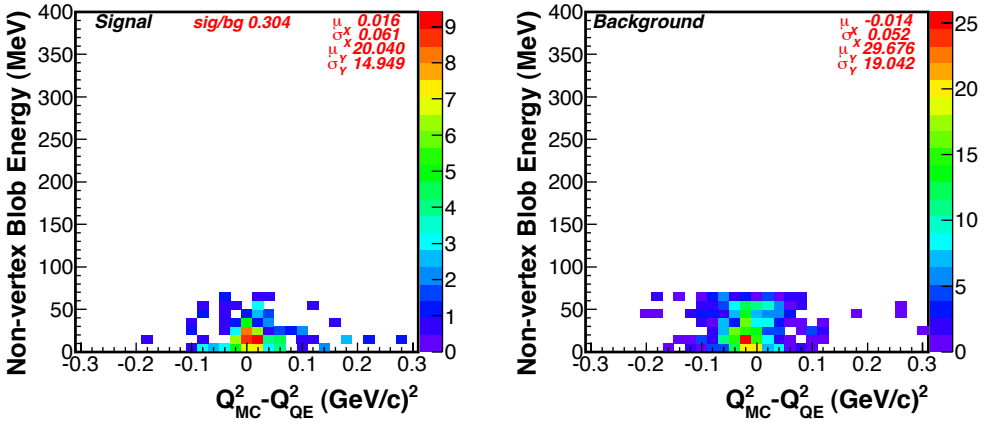

Figure 47: This panel shows the non-vertex energy vs. Q^2 residual for $\Delta KE \in \{-0.75, -0.5\}$. Both the signal and background have a low Q^2 residual, but this bin is background dominant and therefore rejected.

Figures 47, 48 and 49 show the non-vertex energy vs. Q^2 residual for ΔKE bins of $\{-0.75, -0.5\}$, $\{0.4, 0.8\}$ and (the signal region) $\{-0.5, 0.4\}$. The Q^2 residual shows good values in the lowest bin, but the bin is dominated by background. The highest ΔKE bin has very little background, but the Q^2 residual is very poor. The last ΔKE bin, figure 49, shows a good Q^2 residual.

The signal region in ΔKE space was chosen to be $\{-0.5, 0.4\}$. This region is near the maximum of efficiency$\times$purity, reconstructs to above-threshold Q^2 and shows reasonable values for the Q^2 residual.

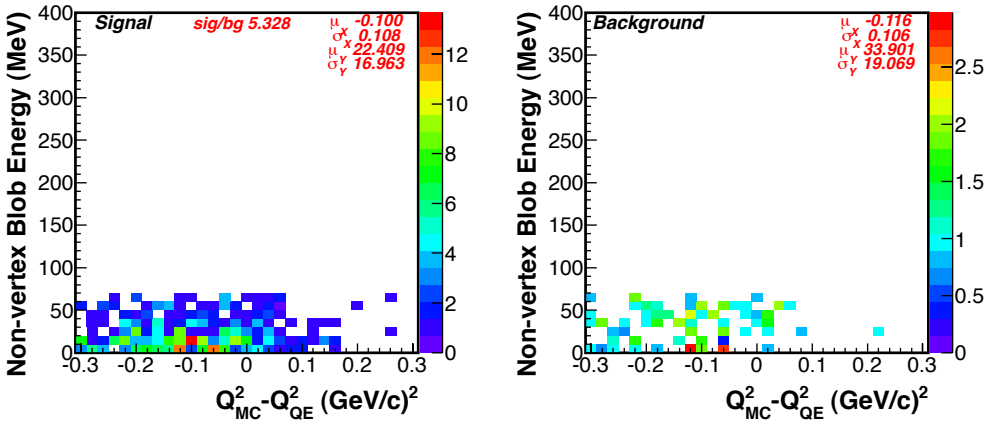

Figure 48: This panel shows the non-vertex energy vs. Q^2 residual for $\Delta KE \in \{0.4, 0.8\}$. This region is signal dominant, but the reconstruction of the event Q^2 is very poor.

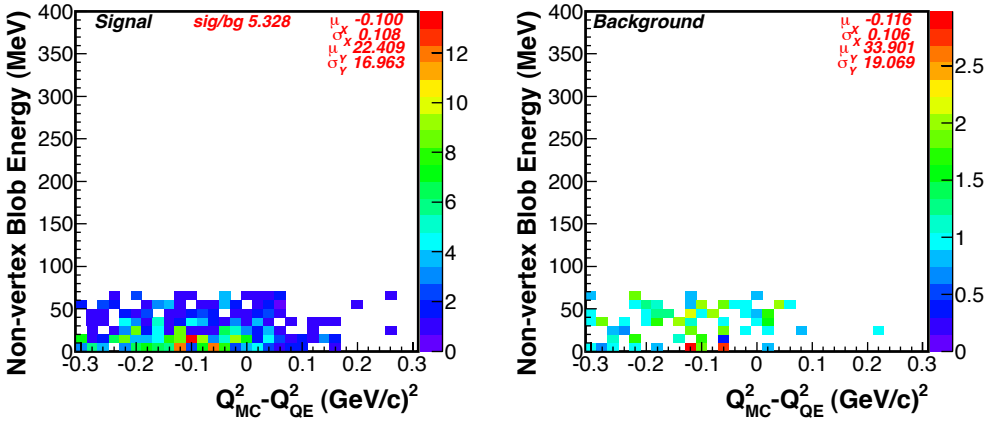

Figure 49: This panel shows the non-vertex energy vs. Q^2 residual for $\Delta KE \in \{-0.5, 0.4\}$. This is the main signal region.

7.4 Unfolding

Unfolding, or unsmearing, is done to remove certain dependencies or biases in distributions. Typically, distributions are unfolded to remove detector dependencies. Matrices are constructed to map reconstructed quantities into true quantities. This enables comparison to various theories in an easier manner. Unfolding was not done for this analysis. All reported quantities will be as a function of reconstructed detector variables. Unfolding will be incorporated in future versions of this analysis.

7.5 Normalization

In the final calculation of a cross section there are various normalization factors that need to be applied. These will be described here.

7.5.1 Data/Monte Carlo Corrections

There are factors in either the data and monte carlo that are not modeled in the other. A correction factor is then applied to either set that takes the mis-modeling into account. The factors are described and then listed in table 9.

Data Corrections:

If there is an interaction in the detector that occurs a few hundred nanoseconds before the selected two-track event, some channels in the detector could have dead time and possibly produce errors in reconstruction. This is not modeled current in the monte carlo. With the current dead time cut, see 7.2, 0.55% of the selected data events are vetoed. This is negligible, but a correction factor was applied to the data regardless.

Monte Carlo Corrections:

The tracking efficiency was measured to be slightly different in monte carlo due to noise present in the data that was not simulated in monte carlo. The muon tracking efficiency was 4.5% lower in monte carlo; the proton tracking efficiency was found to be 5.6% lower in monte

carlo than data. The total tracking efficiency correction factor applied was 0.902.

There were slight differences in the acceptance of muon tracks exiting the back of the MINERνA detector and entering the front of the MINOS detector. The differences were due to fit failures of tracks passing near the MINOS magnetic coil and it was found that the monte carlo had greater failures than the data. A correction of 0.975 was therefore applied to the monte carlo.

The monte carlo does not currently have any overlapping events. This led to the conclusion that there would be an excess of MINOS fit failures from these overlapping events. A detailed study confirmed this and a correction factor of 0.9727 was applied to the monte carlo to take this into account.

There are some events where a muon is present but it is not reconstructed in the MINERνA detector. These events were *not* accounted for in the muon tracking efficiency study due to the details of track selection. These events were dubbed as 'catastrophic dead time' (distinct from the dead time listed above) events and a 0.983 correction factor was applied.

Process (data)	Correction Factor
dead time	0.9955
Total	1.0
Process (monte carlo)	**Correction Factor**
MINERνA Tracking Efficiency	0.902
MINOS acceptance	0.975
MINOS overlap	0.9727
catastrophic dead time	0.983
Total	0.841

Table 9: Table listing the various correction factors that were applied to account for mis-modeling in either the data or monte carlo.

The total correction factor applied to the monte carlo was 0.841.

7.5.2 POT Accounting

The total number of protons (POT) on target is provided via the NuMI beam monitoring and is recorded to the data files on a spill by spill basis. The analysis algorithm counts the POT written to disk and sums the total when data plots are created. This ensures that if a data file is corrupted and/or fails in the processing step that the protons on target in this particular file are not included in the final sum. The total POT for the analysis data set was 8.947×10^{19}. This is slightly smaller than the total 9.54×10^{19} that was recorded for the Minerva01 playlist used in this analysis. This analysis makes use of the AnchoredShortTracker algorithm and this algorithm is known to cause failures for some data files; this is the origin of the smaller POT logged.

The monte carlo has a different method for the protons on target accounting. The total POT exposure is controlled by the GENIE event generator. The flux of neutrinos along with a detailed geometry of the detector is provided to the generator and the final exposure is handled via GENIE. The total POT is just a multiplicative factor of the total number of files processed. Each monte carlo file that is analyzed has an exposure of 9.809×10^{16} POT. There were a total of **3921** files used yielding a total of 3.846×10^{20} protons on target.

The total ratio of data to monte carlo protons on target was 0.2326 ($= \frac{8.947 \times 10^{19}}{3.846 \times 10^{20}}$).

7.5.3 Flux Accounting

The flux was obtained by the beam simulation mentioned in section 3. The flux is crucial for the extraction of a cross section and is an area of constant investigation in the MINERνA experiment. The flux used in this analysis will not be the final version that will be used in any publications of this analysis. The version of the flux used in this analysis is shown in figure 50.

The flux was obtained by integrating the full beam flux up to the 20 GeV energy cut off that was used in this analysis. This gives a value of $3.410 \times 10^{-4}/m^2/POT$. Multiplying by the

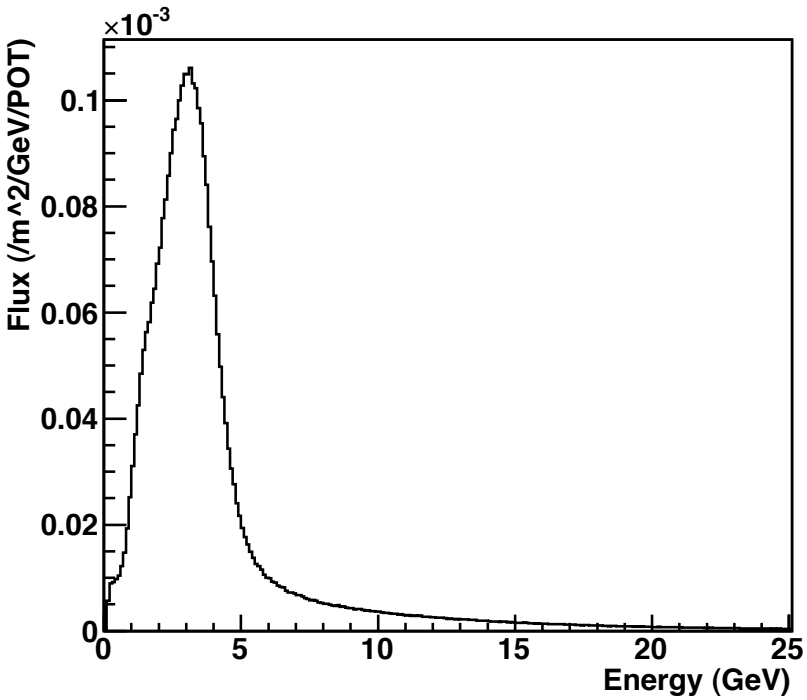

Figure 50: The NuMI ν_μ flux obtained from the g4numi simulation. The flux is being updated and will most likely change for the next version of this analysis.

POT and converting to cm units gives a flux of $3.051 \times 10^{12}/cm^{-2}$.

7.5.4 Target Number

The total number of target neutrons was calculated via simulation. The composition of an inner detector plane was determined as listed in table 10. The isotopic abundance of the elements in a plane is listed in table 11. Using these two tables, the total number of neutrons per cm^2 per plane is calculated to be $5.640 \times 10^{23}/\text{cm}^2/\text{plane}$. The area of an 86cm apothem hexagon is:

$$\begin{aligned} Area &= \tfrac{1}{2}Pa \\ &= \tfrac{1}{2}(12tan(30°)a)a \\ &= 6tan(30°)a^2 \end{aligned}$$

where P is the perimeter and a is the apothem of the hexagon; the final area per plane is 25,620cm^2. The slightly larger volume of 56 modules yields a total of 112 planes. Multiplying all of these factors gives a total of 1.618×10^{30} neutrons.

Element	Atoms/cm^2/plane
H	9.03×10^{22}
C	8.89×10^{22}
O	2.4×10^{21}
Cl	1.89×10^{20}
Ti	1.76×10^{20}
Si	1.29×10^{20}
Al	1.11×10^{20}

Table 10: Table listing the number of atoms per cm^2 per plane in the inner detector of MINERνA.

Element	Abundance (%)	Element	Abundance (%)	Element	Abundance (%)
^{1}H	99.9	^{2}H	0.015		
^{12}C	98.9	^{13}C	1.10		
^{35}Cl	75.77	^{37}Cl	24.23		
^{46}Ti	8.25	^{47}Ti	7.44	^{48}Ti	73.72
^{49}Ti	5.41	^{50}Ti	5.18		
^{28}Si	92.23	^{29}Si	4.67	^{30}Si	3.10
^{27}Al	100				

Table 11: Table listing the isotopic abundance of elements in a plane in the inner detector of MINERνA.

7.6 Event Re-weighting

The reweighting technique used is the 'many universes' technique. It assumes that there is a model with variable and parameter inputs:

$$f(x, y, \alpha, \beta, \gamma)$$

where x and y are variable inputs and $(\alpha_0, \beta_0, \gamma_0)$ are the nominal parameters of the model.

The parameters have uncertainties of $\sigma = \{\sigma_\alpha, \sigma_\beta, \sigma_\gamma\}$. Many different versions of the nominal parameters are generated by taking (in this case) three gaussian random numbers with mean zero and variance one, $\overline{r}$ and computing:

$$(\alpha, \beta, \gamma) = (\alpha_0, \beta_0, \gamma_0) + \Sigma \cdot \overline{r}$$

where Σ is the covariance matrix of the model parameters. The weight of the event in question is the calculated as:

$$weight = \frac{f(x, y, \alpha, \beta, \gamma)}{f(x, y, \alpha_0, \beta_0, \gamma_0)}$$

and then the systematic uncertainty in the jth bin of a given quantity using this method is then:

$$\sigma_j = \sqrt{\frac{1}{N}\sum_i (\nu_i - n_{ij})^2}$$

where N is the number of universes used (usually 1000 in this case), ν_i is the nominal variable and n_{ij} is the shifted variable. The covariance and correlation matrices are:

$$cov(j,k) = \frac{1}{N}\sum_i (\nu_j - n_{ij})(\nu_k - n_{ik}) \quad cor(j,k) = cov(j,k)/\sigma_j\sigma_k$$

This method has the added benefit of being able to compute the weight factors prior to the actual use of the weighting factors in any analysis job.

7.6.1 Flux reweighting

The flux calculation heavily uses reweighting. A detailed description of the flux fitting and reweighting that has been done for the NuMI beam can be found in [28] and [16]. The monte carlo of the beam simulation, as mentioned in section 3, uses particle production data from non-NuMI targets and non-NuMI energies. The data is corrected by reweighting factors. The NuMI monte carlo uses parameterizations of particle yields that are functions of p_T and x_F ($\sim p_z/120\text{GeV}$):

$$\frac{d^2N}{dx_F dp_T} = [A(x_F) + B(x_F)p_T] \times exp(-C(x_F)p_T^{3/2})$$

Here the A,B and C are also themselves functions of x_F given by:

$$A(x_F) = a_1 \times (1 - x_F)a_2 \times (1 + a_3 x_F) \times x_F^{-a_4}$$

$$B(x_F) = b_1 \times (1 - x_F)b_2 \times (1 + b_3 x_F) \times x_F^{b_4}$$

$$C(x_F) = \begin{cases} c1/x_F^{c_2} + c3 & x_F < 0.22 \\ c1/e^{x_F c_3} c_2 + c_4 x_F + c_5 & x_F \geq 0.22 \end{cases}$$

The parameters a_i, b_i and c_i are found by fitting particle yields for π^+, π^-, K^+ and K^-

separately for varying values of x_F [28]. Reweighting factors also exist for the beam focusing and the tertiary particle production. The effect of the reweighting factors on the flux are shown in figure 51 and figure 52. One can see that the reweighting factors have a larger effect on the falling edge of the peak and in the tail. Also, the reweighting factors have a bigger impact on the anti-ν beam than the ν beam.

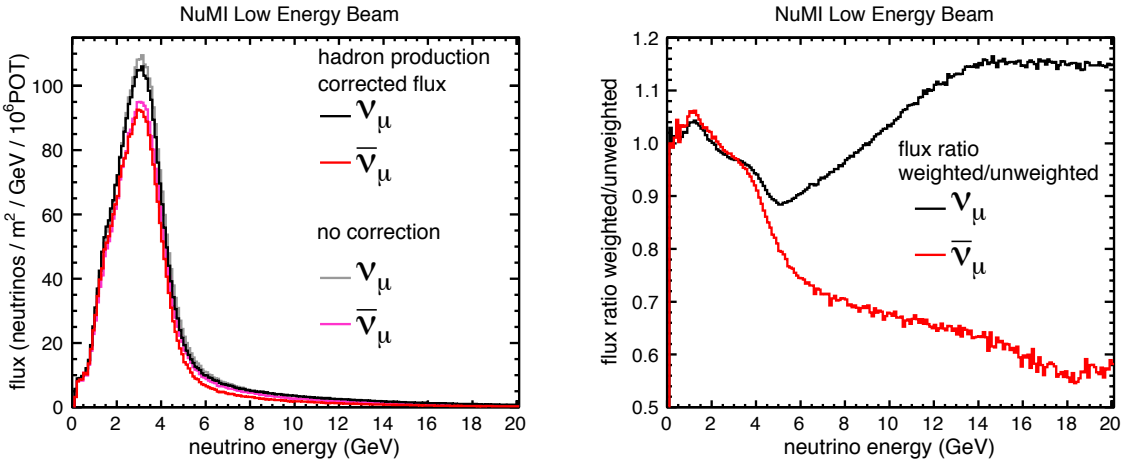

Figure 51: Left: This plot shows the LE neutrino flux before and after reweighting factors have been applied. Right: This plot shows the ratio of the weighted to non-weighted ν_μ flux as a function of the generated neutrino energy.

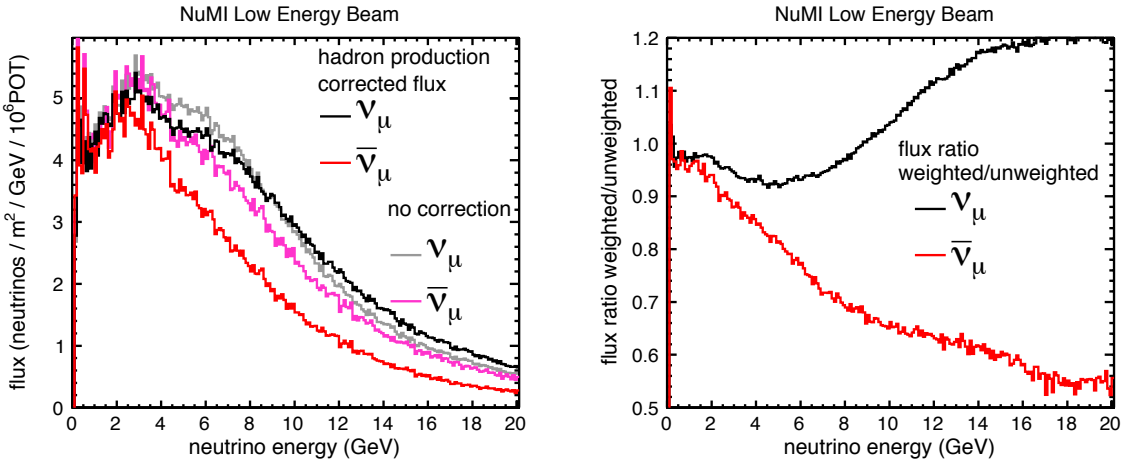

Figure 52: Left: This plot shows the flux of the LE anti-neutrino beam before and after reweighting factors have been applied. Right: This plot shows the ratio of the weighted to non-weighted $\overline{\nu}_\mu$ flux as a function of the generated neutrino energy.

7.7 GENIE Re-weighting

GENIE has built in reweighting features that are used in this analysis. There are several categories of weights in GENIE: weights for the overall uncertainty of the cross section, weights that control interaction models and weights that control nuclear/hadronic models. The latter parameters/models in GENIE that are changed are briefly described in the next two subsections. The results of the reweighting on the systematic error are listed in section 7.8.3.

7.7.1 Interaction Models

The GENIE weights that control details of the primary neutrino interaction are listed in table 12. The table lists the GENIE weight name, a brief description of the parameter and the effect of varying the parameter by $\pm 1\sigma$.

GENIE Weight	Description	1σ Effect
MaNCEL	elastic scattering M_A	$\pm 25\%$
EtaNCEL	elastic scattering η (see section 2.5	$\pm 30\%$
NormCCRES	resonance normalization	$\pm 20\%$
MaRes	resonance M_A	$\pm 20\%$
MvRes	resonance M_V	$\pm 20\%$
Rvp1pi	1π νp/$\overline{\nu}$n non-resonance production	$\pm 50\%$
Rvp1pi	1π νn/$\overline{\nu}$p non-resonance production	$\pm 50\%$
Rvp2pi	2π νp/$\overline{\nu}$n non-resonance production	$\pm 50\%$
Rvp2pi	2π νn/$\overline{\nu}$p non-resonance production	$\pm 50\%$

Table 12: This table lists the GENIE interaction reweighting parameters. These parameters deal with what happens during the primary neutrino interaction.

7.7.2 Nuclear Models

The GENIE weights that control details of the hadron interactions after the primary neutrino event are listed in table 13. The table lists the GENIE weight name, a brief description of the parameter and the effect of varying the parameter by $\pm 1\sigma$.

GENIE Weight	Description	1σ Effect
MFPpi	pion mean free path	$\pm 20\%$
MFPN	nucleon mean free path	$\pm 20\%$
FrAbspi	pion absorption	$\pm 30\%$
FrCExpi	pion charge exchange	$\pm 50\%$
FrElaspi	pion elastic scatter	$\pm 10\%$
FrInelpi	pion inelastic scatter	$\pm 40\%$
FrPiProdpi	pion π production	$\pm 20\%$
FrAbsN	nucleon absorption	$\pm 20\%$
FrCExN	nucleon charge exchange	$\pm 50\%$
FrElasN	nucleon elastic scatter	$\pm 30\%$
FrInelN	nucleon inelastic scatter	$\pm 40\%$
FrPiProdN	nucleon π production	$\pm 20\%$
AGKYxF1pi	AGKY hadronization model - x_F dist.	$\pm 20\%$

Table 13: This table lists the GENIE hadronic/nuclear reweighting parameters. These parameters deal with what happens after the primary neutrino interaction: nucleon absorption, re-interactions, charge exchange, etc.

7.8 Systematic Errors

There were different types of systematic errors investigated. These errors were all determined by various studies and documented in numerous internal MINERνA technical notes. This is not the final list or calculation of systematic errors for the two track analysis. The complete error a nalysis is part of an ongoing effort, which will use the full Minerva data set. Consequently some errors have not been included in this analysis. A number of flat data/monte carlo efficiency corrections were evaluated. Neutrino flux and GENIE systematic errors were evaluated also. The different components of the non-vertex energy cut were scaled and a systematic error assigned. The muon energy scale, proton energy scale and the proton identification systematic errors were investigated, but a final systematic error for these quantities was not determined.

7.8.1 Flat Errors

There is a class of errors that have a 'flat' systematic error associated with them. The same flat error is applied to all of the Q^2 bins in the final calculated spectrum.

Tracking Efficiency:

The tracking efficiency for muons (in neutrino mode) was investigated in both data and monte carlo. The efficiency for muons was measured to be 4.5% lower in monte carlo than in data. The uncertainty was estimated at 2.5%. The monte carlo is scaled for this correction before comparing to data. The tracking efficiency for protons was found to be 5.6% lower in monte carlo than in data; the uncertainty was estimated at 3.5%

MINOS Related Errors:

There is a correction associated with the acceptance of muons in the MINOS monte carlo and data. These errors come from muon tracks that pass near/through the MINOS magnetic coil and have unreliable momentum measurements: this is the case for muons reconstructed via range and curvature (although recall all analyses use muon reconstructed via curvature). The monte carlo has a deficiency of 2.5% $\pm$ 2.5% compared to the data sample and is corrected for this lack of events.

The current simulation does not have overlapping events that are present in the data. The discrepancy occurs when two muons enter the MINOS detector and because the tracks overlap, only one of the tracks gets reconstructed and has a momentum associated to it. The other track appears as a short track without any momentum. A study was performed to determine this discrepancy between the data and monte carlo. The monte carlo needs to scaled by 97.2%. The error associated with this measurement in 0.6%.

Discriminator Dead Time Errors:

After a readout window, the discriminators in the detector are dead for a period of time. This prevents hits from being read out and can cause failures in the reconstruction. The first correction comes from dead time that causes tracks not to be reconstructed to the back of the MINERνA detector. This causes an error in the total number of muons that are detected by MINERνA/MINOS. A study of this effect found that the monte carlo needs to be scaled down by 1.7% $\pm$ 1.7%.

There is another error associated with dead time. This error is due to dead discriminators that are upstream of the reconstructed muon tracks. This causes the muon vertex to be reconstructed downstream of the true vertex. The reconstructed muon track (in data) is propagated upstream and the number of dead discriminators in this path is counted. Events that have two or more dead discriminators in this propagated upstream path are removed from the sample. In the two track sample this corresponds to 0.6% of the total events that are tagged. This is a very small corrected factor, by the monte carlo is scaled down by the 0.6% $\pm$ 0.6%.

Target Mass:

The last flat error correction is from the target mass. The monte carlo detector geometry was generated from the survey of the actual MINERνA detector. There is no correction factor applied to the either the data or monte carlo. The error on the target mass was determined to be 1.4%.

7.8.2 Flux Systematic Error

The flux is an ongoing source of investigation. There are continuous efforts the reduce the systematic errors on the flux. The flux used in this analysis is just the first version to be used and will most likely have reduced errors in the future. The flux had three separate errors associated with it: one error from differences in the hadron production model used in the monte carlo, one due to the beam focusing from the magnetic horns and the final error was from tertiary particle production from the muons in the decay and absorber volumes.

7.8.3 GENIE Systematic Error

GENIE has an overall cross section systematic error and then two other categories of systematic errors. The first category contains error associated with interaction models and the errors are listed in table 12. The second category contains error associated with hadronic models and the errors are listed in table 13.

When calculating the value of the cross section, a few of the GENIE errors were not varied as to not bias the value of the measurement. The errors not included are: **VecFFCCQEshape**, **MaCCQEshape**, **CCQEPauliSupViaFK** and **NormCCQE**.

7.8.4 Non-vertex/Extra Energy Error

The non-vertex extra energy was matched to the monte carlo particle that created it: proton, neutron, charged pion, EM particle (γ, $e^{\pm}$ or ^{0}) or other. If no match was found, the energy was labeled as cross talk. Each one of the particle categories was scaled to find the systematic error on the non-vertex energy. The energy created by neutron particles was scale up and down by 20% and the energy from protons, charged pions, EM particles and the *others* category was scaled by $\pm$10%.

7.8.5 Tracking Error

The systematic error on the vertex position from the reconstruction was evaluated by the following method: MINOS matched muons with a vertex inside of the fiducial volume were selected in both data and monte carlo. The track in the scintillator region is split in half with equal (or as near as can be) nodes; both tracks share one node (the downstream end of the upstream track is the upstream end of the downstream track). The upstream track is given the momentum of the original track, p_0 and the downstream track has the momentum $p_0 - nE_{avg}$, where n is the number of nodes on the upstream track and E_{avg} is the average planar energy deposited by a muon. Both of the tracks are refit (with multiple scattering enabled). The positional and angular residual of the overlapping state is formed and fit to a double gaussian function. Figure 53 shows the double gaussian fit results for the data and monte carlo. Figure 54 shows the data/MC agreement of the vertex positional residuals and figure 55 shows the data/MC agreement of the vertex angular residuals.

These studies led to the assumption of a 1.4mm systematic error the vertex positions and a

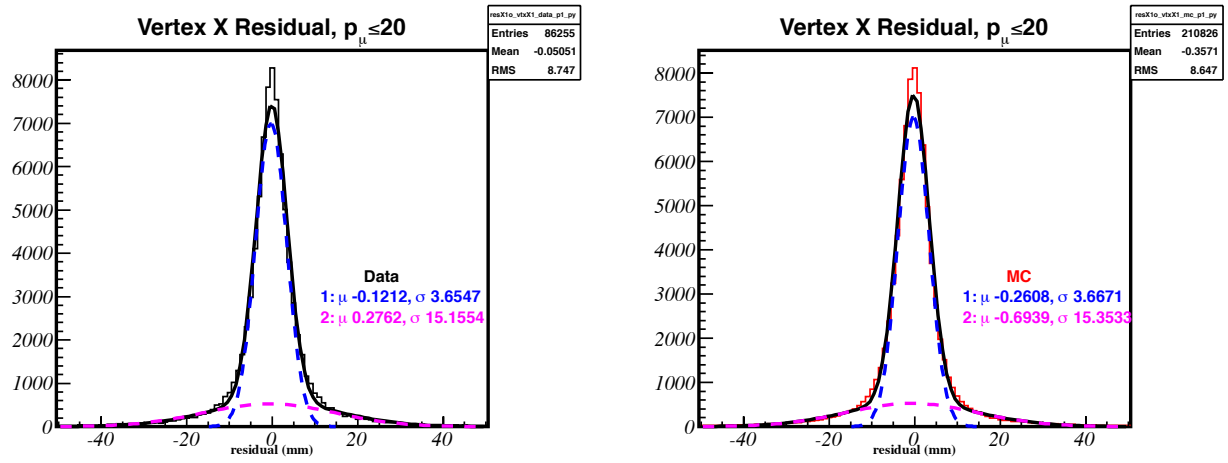

Figure 53: The X position residual for the overlap state fit to a double gaussian, shown on the left for data and the right for MC.

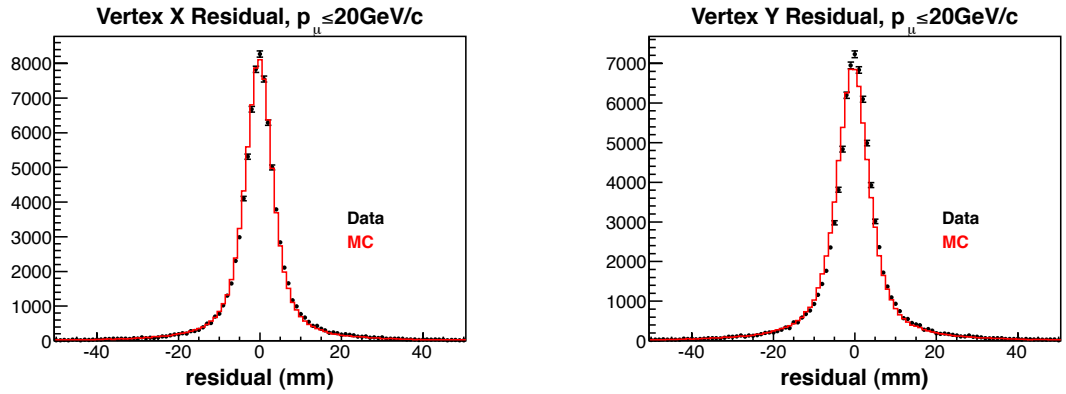

Figure 54: The left panel shows the Right: Y

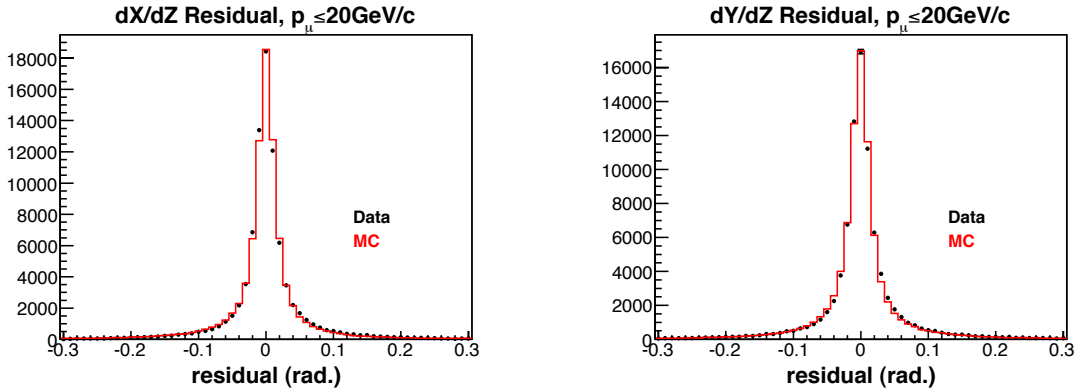

Figure 55: Left: aX Right: aY

1.8mrad systematic error for the angles of the muon track. This error was investigated, but found to be negligible and not included into the total error budget.

7.8.6 Future Systematic Error Work

Muon Energy Scale:

A dedicated study was done to determine the muon energy scale. The muon energy had three components of error associated with it. There is one error due to the material budget that the track passes through; this was determined to be 11 MeV. The next muon energy error is from the dE/dX energy calculation; this was set at 30 MeV. The final error is from the muon energy determination from the MINOS detector; this was set at 5% if the muon energy was below 1.5 GeV and 2% if the muon energy was above or equal to 1.5 GeV.

This error was *not* included in the final systematic errors reported. The $\overline{\nu}_\mu$ analysis reported fractional systematic errors due to the muon energy scale of between approximately 4% in the most populated Q^2 bins. Obviously, these errors do not translate into the two track analysis, but the level of the error gives an idea of scale of this systematic.

Particle Identification Error:

The particle identification and dE/dX χ^2 have been a topic of discussion for a long period of time; recall that the PID with only the proton and pion particle hypotheses used in the calculation is a direct comparison relation between the dE/dX χ^2, see subsection Cut Placement in section 7.2. This systematic error would ideally come from test beam program analysis. As mentioned in the previous subsection, the test beam analysis is not at the stage of being able to provide this error. The software algorithms that calculate the dE/dX χ^2 and PID variable have been in continual update for about two months. Subsequent updates to this code have shown significant changes between versions. In addition, the changes to the track cleaning procedure has added to the discrepancies between versions.

As a result, there is no systematic error associated with the particle identification. This error

is being studied both with full MINERνA detector data and monte carlo in addition to be studied in the test beam data and monte carlo. Subsequent versions of the analysis will have a systematic error associated with these variables.

Proton Energy Error:

The proton momentum error was determined via the test beam program of the MINERνA experiment and was set to be 10%. This 10% error was from an initial study that was performed in the past and has been reduced in further analysis. A more sophisticated study is being done at the time of this document that will give a better estimate of the proton momentum error, There will be a more in-depth study of the proton energy in the future including errors due to the material budget and the dE/dX energy calculation. But these were not performed as of yet due to the collaboration's focus on the $\nu/\overline{\nu}_{\mu}$ one-track analyses. The proton energy is used in the ΔKE cut variable used in the event selection and therefore important in the final reported result. An initial calculation of this systematic error were performed but it found to be incorrect with the newer versions of the code, as with the PID error, and therefore not included in the final systematic error budget.

7.9 Final Systematic Errors

The final systematic errors for the Q^2 bins used in the analysis is listed in table 14. The first Q^2 bin is not shown in the error table because it has no entries and is below the proton tracking threshold. The largest errors come from the flux and the overall GENIE cross section.

7.10 Final Result

The various distributions that are used to form the final result will be shown. The left plots of figure 56 shows the raw data and monte carlo distributions that are obtained from applying the event selection to the neutrino sample. The right plot of the figure shows the background corrected distributions. The absolute background level was obtained from the protons on target scaled monte carlo. This background is then subtracted from both data and monte carlo

Fractional Systematic Error Table

Q^2 Bins	(0.13,0.23)	(0.23,0.33)	(0.33,0.43)	(0.43,0.53)	(0.53,0.63)	(0.63,0.73)	(0.73,0.83)	(0.83,1.23)
Flat Errors								
target mass	0.0140	0.0140	0.0140	0.0140	0.0140	0.0140	0.0140	0.0140
catastrophic dead time	0.0100	0.0100	0.0100	0.0100	0.0100	0.0100	0.0100	0.0100
minos overlap	0.0060	0.0060	0.0060	0.0060	0.0060	0.0060	0.0060	0.0060
dead time cut	0.0055	0.0055	0.0055	0.0055	0.0055	0.0055	0.0055	0.0055
muon tracking efficiency	0.0250	0.0250	0.0250	0.0250	0.0250	0.0250	0.0250	0.0250
proton tracking efficiency	0.0350	0.0350	0.0350	0.0350	0.0350	0.0350	0.0350	0.0350
Non-vertex Errors								
neutron response down	0.0362	0.0104	0.0094	0.0022	0.0075	0.0000	0.0331	0.0000
proton response up	0.0050	0.0075	0.0032	0.0075	0.0161	0.0000	0.0292	0.0000
proton response down	0.0000	0.0083	0.0013	0.0057	0.0150	0.0172	0.0332	0.0203
pion response up	0.0088	0.0173	0.0061	0.0036	0.0091	0.0000	0.0000	0.0000
pion response down	0.0141	0.0200	0.0093	0.0041	0.0044	0.0000	0.0000	0.0000
EM response up	0.0044	0.0015	0.0000	0.0020	0.0000	0.0000	0.0271	0.0000
EM response down	0.0000	0.0035	0.0015	0.0000	0.0000	0.0000	0.0000	0.0000
other response up	0.0042	0.0000	0.0000	0.0000	0.0000	0.0000	0.0000	0.0000
other response down	0.0000	0.0015	0.0031	0.0000	0.0000	0.0000	0.0000	0.0000
Interaction Errors								
EtaNCEL	0.0000	0.0000	0.0000	0.0000	0.0000	0.0000	0.0000	0.0000
MaNCEL	0.0000	0.0000	0.0000	0.0000	0.0000	0.0000	0.0000	0.0000
MaRES	0.0550	0.0491	0.0438	0.0397	0.0416	0.0348	0.0324	0.0270
MvRES	0.0200	0.0214	0.0208	0.0202	0.0216	0.0185	0.0173	0.0152
NormCCRES	0.0792	0.0572	0.0432	0.0356	0.0331	0.0272	0.0238	0.0190
NormDISCC	0.0000	0.0000	0.0000	0.0000	0.0000	0.0000	0.0000	0.0000
Rvn1pi	0.0168	0.0130	0.0076	0.0071	0.0083	0.0040	0.0000	0.0137
Rvn2pi	0.0000	0.0013	0.0004	0.0000	0.0000	0.0000	0.0000	0.0000
Rvp1pi	0.0080	0.0087	0.0085	0.0055	0.0074	0.0000	0.0000	0.0000
Rvp2pi	0.0015	0.0013	0.0017	0.0010	0.0019	0.0000	0.0000	0.0000
Hadron Model Errors								
AGKYxF1pi	0.0017	0.0049	0.0049	0.0020	0.0018	0.0011	0.0000	0.0004
FrAbs N	0.0448	0.0458	0.0551	0.0567	0.0548	0.0522	0.0756	0.0705
FrAbs pi	0.0083	0.0004	0.0032	0.0006	0.0017	0.0001	0.0041	0.0046
FrCEx N	0.0027	0.0011	0.0005	0.0005	0.0015	0.0013	0.0014	0.0012
FrCEx pi	0.0090	0.0040	0.0043	0.0028	0.0024	0.0033	0.0012	0.0008
FrElas N	0.0817	0.0811	0.0956	0.0939	0.0954	0.0968	0.1139	0.1109
FrElas pi	0.0084	0.0046	0.0052	0.0036	0.0018	0.0043	0.0033	0.0005
FrInel N	0.0007	0.0006	0.0007	0.0024	0.0015	0.0008	0.0070	0.0035
FrInel pi	0.0198	0.0165	0.0123	0.0105	0.0042	0.0109	0.0082	0.0054
FrPiProd N	0.0000	0.0000	0.0002	0.0003	0.0004	0.0006	0.0010	0.0012
FrPiProd pi	0.0002	0.0001	0.0001	0.0000	0.0002	0.0002	0.0000	0.0005
MFP N	0.0227	0.0257	0.0366	0.0361	0.0234	0.0167	0.0037	0.0000
MFP pi	0.0021	0.0015	0.0066	0.0072	0.0073	0.0018	0.0190	0.0000
RDecBR1gamma	0.0002	0.0001	0.0001	0.0000	0.0000	0.0000	0.0001	0.0000
Theta Delta2Npi	0.0132	0.0012	0.0042	0.0004	0.0058	0.0056	0.0033	0.0006
GENIE XS Error								
GENIE	0.1622	0.1862	0.2142	0.2409	0.2601	0.2915	0.3170	0.3314
Flux Systematics								
Flux Tertiary	0.0914	0.0987	0.0960	0.1078	0.0887	0.1070	0.1061	0.1108
Flux NA49	0.0579	0.0596	0.0594	0.0567	0.0600	0.0604	0.0629	0.0663
Flux BeamFocus	0.0316	0.0324	0.0356	0.0386	0.0396	0.0421	0.0465	0.0358
Total	0.2496	0.2601	0.2826	0.3048	0.3149	0.3443	0.3799	0.3855
Statistical	0.1140	0.0679	0.0665	0.0796	0.1162	0.1796	0.3015	0.2673

Table 14: This table lists the fraction systematic errors for the two-track analysis.

distributions. Future iterations of this analysis will use data/MC distributions to constrain and fit for the background fraction.

For completeness, the area normalized data and monte carlo distributions are shown in figure 57. This plot has not been background or acceptance corrected.

The distributions are then corrected for acceptance. The acceptance is shown in figure 39 in section 7.2. The first two bins are zeroed out in this step. Recall that the first two bins in this distribution correspond to a proton that is below the tracking threshold of the shortPR,

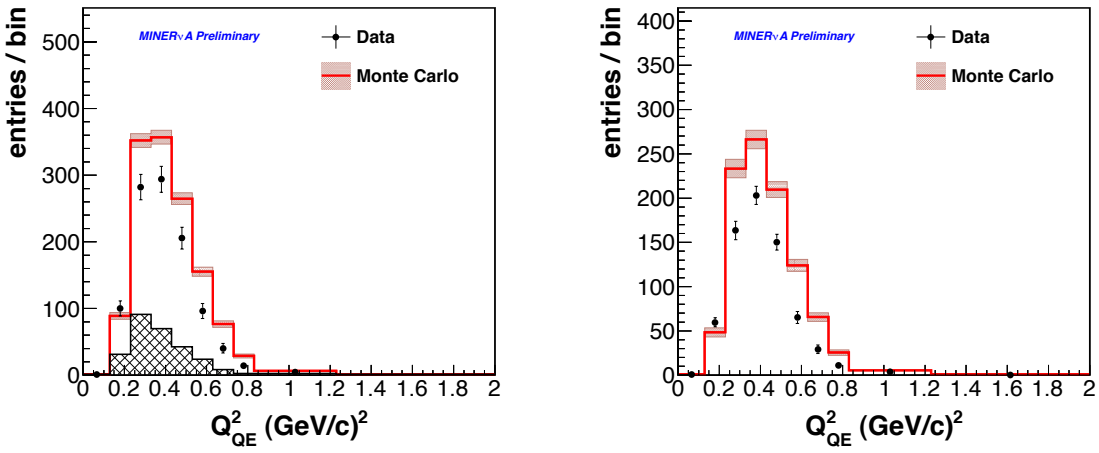

Figure 56: The left panel shows the raw data and MC distributions. The right panel shows the background corrected distributions. The background was obtained from the POT scaled monte carlo distribution.

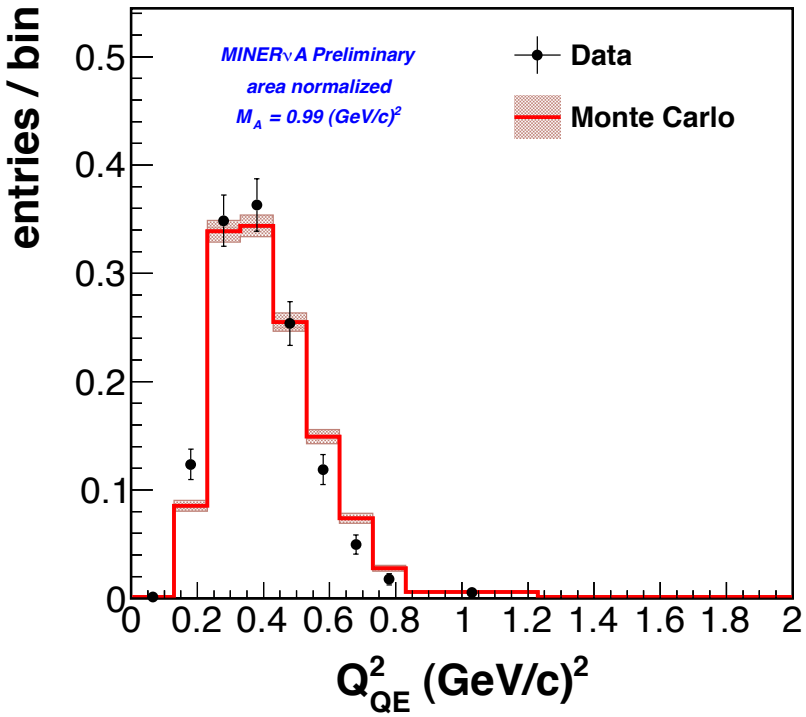

Figure 57: The area normalized data and monte carlo two-track distributions. This distribution has *not* been background or acceptance corrected.

see section 7.3.3.

After the acceptance correction, the distributions are normalized by the product of the number of neutron targets times the data protons on target times the neutrino flux: 1.618×10^{30} neutrons, 8.947×10^{19} POT and $3.410 \times 10^{-8}/\text{cm}^{-2}/\text{POT}$. These multiply together to give a normalization factor of 4.939×10^{42}. The final result is the two-track charged current quasi-elastic cross section and is shown in figure 58.

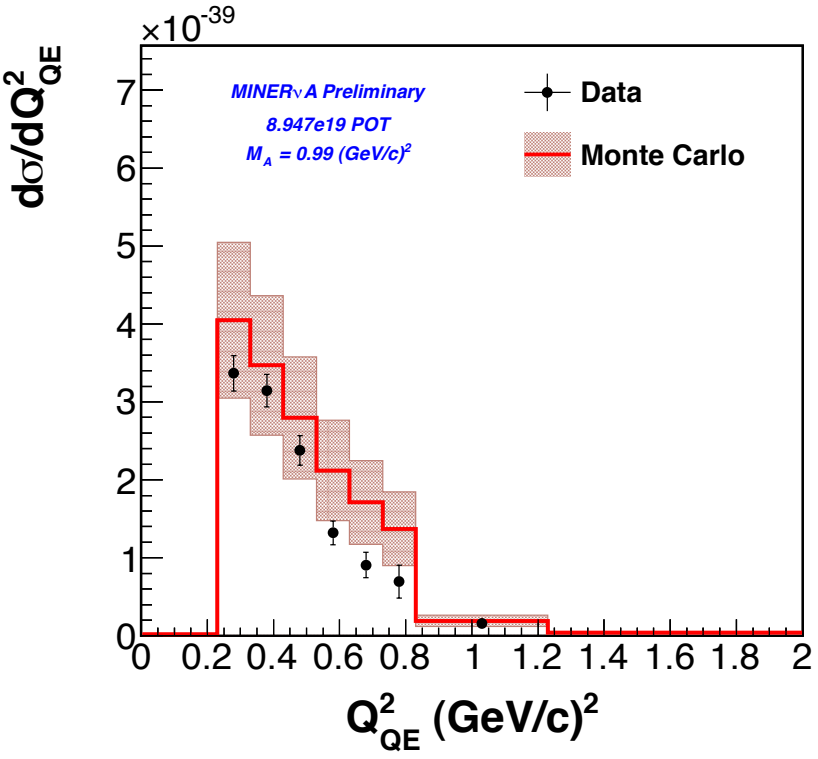

Figure 58: This plot shows the final result of the analysis: the two-track charged current quasi-elastic cross section.

8 Conclusions

The MINERνA detector has collected roughly 4×10^{20} protons on target of neutrino data and a total of 2.5×10^{20} protons on target in anti-neutrino mode in two different detector configurations. This data was collected while the NuMI beam was in the low energy configuration. The detector is scheduled to collect approximately three times this amount of data in the medium energy mode of the NuMI beam. This data will be used to extract high precision cross sections to be used in future neutrino experiments. Nuclear effects, meson exchange currents and the strangeness component of the nucleon spin are a few of the other topics that MINERνA data can also address.

A subset of the initial neutrino data was investigated and a two-track charged current quasi-elastic cross section was formulated. A total of 8.947×10^{19} POT was used to form this cross section. A two-track vertex consisting of one track extending into the MINOS detector and the other track contained in the detector identified as a proton by the energy deposited per length was used in the analysis. A cut on the extra energy in the event and one on a CCQE-enhancing variable was used to separate signal from background. An initial list of systematic errors is presented and evaluated for the analysis. Future versions of this analysis will include the use of the full neutrino data, most likely be combined with the corresponding one-track neutrino CCQE analysis.

References

[1] NuTeV Collaboration. A precise determination of electroweak parameteres in neutrino-nucleon scattering. *[hep-ex/0110059]*, 2003.

[2] H.Budd A.Bodek and J.Arrington. Vector and axial form factors applied to neutrino quasielastic scattering. *[hep-ex/0410055]*, 2004.

[3] K2K Collaboration. Measurement of the quasi-elastic axial vector mass in neutrino-oxygen interactions. *[hep-ex/0603034]*, 2006.

[4] V.Lyubushkin. A study of quasi-elastic muon neutrino and anti-neutrino scattering in the nomad experiment. *Eur.Phys.J.C*, 63, 2009.

[5] K2K Collaboration. Search for coherent charged current pion production in neutrino-carbon interactions. *Phys.Rev.Lett*, 95 252301, 2005.

[6] MINERVA Collaboration. *Proposal to Perform a High-Statistics Neutrino Scattering Experiment Using a Fine-grained Detector (and subsequent revisions).* [hep-ex/0405002].

[7] E.A.Pachos M.Sakuda I.Schienbein and J.Y.Yu. Comparison of a new δ resonance model with electron and neutrino data. *[hep-ph/0408185]*, 2004.

[8] P.A.Schreiner and F.Von Hippel. Neutrino production of the $\delta(1236)$. *Nucl.Phys.*, B58, 1973.

[9] M.Arneodo. Nuclear effects in structure functions. *Phys.Rept.* **240***, 301*, 1994.

[10] G.Piller and W.Weise. Nuclear deep-inelastic lepton scattering and coherence phenomena. *Phys.Rept.* **330***, 1*, 2000.

[11] R.Petti S.A.Kulagin. Global study of nuclear structure functions. *[hep-ph/0412425]*, 2005.

[12] W.Weise S.A.Kulagin, G.Piller. Shadowing, binding, and off-shell effects in nuclear deep-inelastic scattering. *Phys.Rev.C*, 50, 1994.

[13] C.Maieron W.M.Alberico, S.M.Bilenky. Looking for strangenesswith neutrino-nucleon scattering. *[hep/ph/0311053]*, 2003.

[14] L.A.Ahrens et.al. Measurement of neutrino proton and anti-neutrino proton elastic scattering. *Phys.Rev.*, D35, 1987.

[15] Christophe Praet. Modeling quasi-free neutrino nucleus reactions for accelerator-based experiments. *Thesis, Gent University*, 2008.

[16] Laura Loiacono. Measurement of the muon neutrino inclusive charged current cross section on iron using the minos detector. *Thesis, UT Austin*, 2010.

[17] G.N. Perdue, L. Bagby, B. Baldin, C. Gingu, J. Olsen, P. Rubinov, E.C. Schulte, R. Bradford, W.K. Brooks, D.A.M. Caicedo, C.M. Castromonte, J. Chvojka, H. da Motta, I. Danko, J. Devan, B. Eberly, J. Felix, L. Fields, G.A. Fiorentini, A.M. Gago, R. Gran, D.A. Harris, K. Hurtado, H. Lee, E. Maher, S. Manly, C.M. Marshall, K.S. McFarland, A. Mislivec, J. Mousseau, B. Osmanov, J. Osta, V. Paolone, R.D. Ransome, H. Ray, D.W. Schmitz, C. Simon, C.J. Solano Salinas, B.G. Tice, T. Walton, J. Wolcott, D. Zhang, and B.P. Ziemer. The data acquisition system and infrastructure. *Nuclear Instruments and Methods in Physics Research Section A: Accelerators, Spectrometers, Detectors and Associated Equipment*, 2012.

[18] C. Andreopoulos et al. The GENIE Neutrino Monte Carlo Generator. *Nucl. Instrum. Meth.*, A614:87–104, 2010.

[19] A.Bodek and J.L.Ritchie. Further studies on fermi motion effects in lepton scattering from nuclear targets. *Phys.Rev.*, D24, 1981.

[20] C.H. Llewelly Smith. Neutrino reactions at accelrator energies. *Phys.Rept.*, vol 3, 1972.

[21] D.Rein and L.M.Sehgal. Neutrino excitationof baryon resonances and signle pion production. *Annals.Phys*, 133, 1981.

[22] A.Bodek and U.K.Yang. Higher twist scaling and effective lo pdfs for lepton scattering in the few gev region. *J.Phys.*, G29, 2003.

[23] R. Frhwirth. Application of kalman filtering to track and vertex fitting. *Nuclear Instruments and Methods in Physics Research Section A: Accelerators, Spectrometers, Detectors and Associated Equipment*, 262(2-3), 1987.

[24] E.J. Wolin and L.L. Ho. Covariance matrices for track fitting with the kalman filter. *Nucl.Instrum.Meth.*, A329, 1993.

[25] R Frhwirth, Wolfgang Waltenberger, and Pascal Vanlaer. Adaptive vertex fitting. Technical Report CMS-NOTE-2007-008, CERN, Geneva, Mar 2007.

[26] Rolf Luchsinger and Christoph Grab. Vertex reconstruction by means of the method of kalman filtering. *Computer Physics Communications*, 76(3):263 – 280, 1993.

[27] Wolfgang Waltenberger. Adaptive vertex reconstruction. Technical Report CMS-NOTE-2008-033, CERN, Geneva, Jul 2008.

[28] Zarko Pavlovic. Observation of disappearanc of muon neutrinos in the numi beam. *Thesis, UT Austin*, 2008.